Analysis and Visualization of Exact Solutions to Einstein's Field Equations

by

Majd Abdelqader

A thesis submitted to the
Department of Physics, Engineering Physics & Astronomy
in conformity with the requirements for
the degree of Doctor of Philosophy

Queen's University
Kingston, Ontario, Canada
September 2013

Abstract

Einstein's field equations are extremely difficult to solve, and when solved, the solutions are even harder to understand. In this thesis, two analysis tools are developed to explore and visualize the curvature of spacetimes. The first tool is based on a thorough examination of observer independent curvature invariants constructed from different contractions of the Riemann curvature tensor. These invariants are analyzed through their gradient fields, and attention is given to the resulting flow and critical points. Furthermore, we propose a Newtonian analog to some general relativistic invariants based on the underlying physical meaning of these invariants, where they represent the cumulative tidal and frame-dragging effects of the spacetime. This provides us with a novel and intuitive tool to compare Newtonian gravitational fields to exact solutions of Einstein's field equations on equal footing. We analyze the obscure Curzon-Chazy solution using the new approach, and reveal rich structure that resembles the Newtonian gravitational field of a non-rotating ring, as it has been suspected for decades. Next, we examine the important Kerr solution, which describes the gravitational field of rotating black holes. We discover that the observable part of the geometry outside the black hole's event horizon depends significantly on its angular momentum. The fields representing the cumulative tidal and frame-dragging forces change qualitatively at seven specific values of the dimensionless spin parameter of

the black hole. The second tool we develop in this thesis is the accurate construction of the Penrose conformal diagrams. These diagrams are a valuable tool to explore the causal structure of spacetimes, where the entire spacetime is compactified to a finite size, and the coordinate choice is fixed such that light rays are straight lines on the diagram. However, for most spacetimes these diagrams can only be constructed as a qualitative guess, since their null geodesics cannot be solved. We developed an algorithm to construct very accurate Penrose diagrams based on numeric solutions to the null geodesics, and applied it to the McVittie metric. These diagrams confirmed the long held suspicion that this spacetime does indeed describe a black hole embedded in an isotropic universe.

Statement of Co-Authorship

The research presented in this thesis was done under the supervision of Kayll Lake at Queen's University. All the work presented here was done by the author (Majd Abdelqader) except where explicitly stated otherwise.

Chapter 2 contains a version of a paper published in Physical Review D as: *Majd Abdelqader and Kayll Lake "Visualizing spacetime curvature via gradient flows. II. An example of the construction of a Newtonian analogue", Physical Review D* ***86****, 124037 (2012).* I am the lead author of this paper. I wrote the manuscript, performed all the calculations and produced all the figures. Kayll Lake edited the manuscript, and added the mass appendix.

Chapter 3 contains a version of a paper published in Physical Review D as: *Majd Abdelqader and Kayll Lake "Visualizing Spacetime Curvature via Gradient Flows III: The Kerr Metric and the Transitional Values of the Spin Parameter", Physical Review D* ***88****, 064042 (2013).* I am the lead author of this paper. I wrote the manuscript, performed all the calculations and produced all the figures under the supervision of Kayll Lake.

Chapter 4 contains a version of a paper published in Physical Review D as: *Kayll Lake and Majd Abdelqader "More on McVittie's legacy: A Schwarzschild-de Sitter*

black and white hole embedded in an asymptotically ΛCDM cosmology", Physical Review D, ***84****, 044045 (2011).* Kayll Lake is the lead author of this paper. I created the algorithm to produce the conformal Penrose diagrams numerically, on which the main analysis presented in the paper is based. I performed all the numerical calculations, wrote the section describing the numerical algorithm used to construct the conformal diagrams, and produced all the figures except for figures 1 and 2.

Chapter 5 contains a version of a paper published in Physical Review D as: *Philippe Landry, Majd Abdelqader, and Kayll Lake "McVittie solution with a negative cosmological constant", Physical Review D,* ***86****, 084002 (2012).* Philippe Landry is the lead author of this paper. I performed all the numerical calculations based on the algorithm I created in Chapter 4, wrote the section describing the construction of the conformal diagrams for this spacetime, and produced all the figures except for figures 1 and 2.

Acknowledgments

I would like to thank my supervisor Kayll Lake for all the advise, guidance and support over the course of my PhD studies.

I wish to thank my parents, Nada and Abdelqader, for their support and encouragement at every stage of my studies.

Special thanks to Stéphane Courteau for being a very involved and supportive coordinator of graduate studies in the physics department. I also wish to thank the faculty members of the Queen's University Astronomy Research Group for creating a great academic environment.

I also wish to thank the administrative staff of the physics department at Queen's University, especially Loanne Meldrum.

Last but not least, I would like to thank my dear friends Joel Roediger, Mitch Anderson, Jeremy Durelle and Abdullah Abunafeesa.

Table of Contents

List of Figures

Chapter 1

General Introduction

The non-linearity of Einstein's field equations makes them extremely challenging to solve, even forcing Einstein to initially think that the equations cannot be solved analytically. After Karl Schwarzschild succeeded in finding his famous analytic solution in 1915 describing the gravitational field outside spherically symmetric objects, Einstein wrote to him saying [1] "*I have read your paper with the utmost interest. I had not expected that one could formulate the exact solution of the problem in such a simple way.*" What is more troubling is that even when an exact solution is found, understanding the meaning of the solution is yet a more cumbersome task. There are many technical reasons for this, and most will be discussed below, but the gauge invariance aspect of general relativity contributes greatly to the confusion about the meaning of any solution. There is not a priori geometry on which the theory of general relativity is built, and the source of the spacetime actually determines the geometry. Furthermore, any solution can be transformed and written in infinitely many different coordinate systems, and no set of coordinates is preferred. Of course,

calculations of any sort of predictions or observables have to be performed in a coordinate independent way. However, a smart, or lucky, choice of coordinates can make all the difference in simplifying the calculations, or even lead to a solution in the first place. In spite of all these difficulties, there exists hundreds of exact solutions to Einstein's field equations.

From an experimental and observational point of view, general relativity has been greatly successful. Within the solar system, the theory accurately explained the advance of Mercury's perihelion, predicted the bending of light around a massive object like the Sun, and the gravitational time delay of light bouncing off Venus and Mercury. Furthermore, at a terrestrial scale, the Pound–Rebka experiment provided a very precise test of the gravitational redshift predicted by general relativity. Interesting enough, all the success that general relativity enjoys is based on weak field approximations, or only a handful of exact solutions [2, 3]. So one might ask why do we need to understand more exact solutions, or even develop more tools to do so?

The observations and experiments are getting to the point where we might very soon directly detect gravitational phenomena in the strong field limit. For example, the Event Horizon Telescope project plans to observe the region containing the supermassive black hole of the Milky Way with a resolution high enough to detect the shadow of the event horizon by the end of the decade [4, 5]. Furthermore, gravitational wave detection experiments, including advanced LIGO and Pulsar Timing Arrays, might soon be sensitive enough to detect gravity wave signals of black hole collisions and mergers. Numerical relativity simulations are needed to provide accurate predictions of these wave forms, but a thorough analysis of the simulation results is needed.

In this thesis, we develop and present new tools to analyze solutions to Einstein's field equations. Although we apply these tools to exact solutions so far, the ultimate goal is make them useful and applicable to any spacetime, including numerical relativity simulations as well. In the following section we explain the motivation behind developing each tool. After that, we present some technical background that provides the foundation of the first tool.

1.1 Motivation

Using geometric natural units, where $G = c = 1$, Einstien's field equations can be written as

$$R_{\mu\nu} - \frac{1}{2} g_{\mu\nu} R + g_{\mu\nu}\Lambda = 8\pi T_{\mu\nu} \tag{1.1}$$

where $R_{\mu\nu}$ is the Ricci tensor, R the Ricci scalar, Λ the cosmological constant and $T_{\mu\nu}$ the energy - momentum tensor. The equations are in principle second order partial differential equations of the metric $g_{\mu\nu}$, and the two main issues that make the theory especially complicated can be summarized as the following

- The equations are highly non-linear. This makes the theory very difficult to solve from a mathematical point of view. Furthermore, even when solutions are found, there is not a systematic way to produce more solutions by superposition of known ones, which is a useful property of other classical linear theories like Newtonian gravity and classical electromagnetism.

- There is no background geometry or preferred coordinates on which to build solutions. The source of the spacetime determines the geometry, and each

geometry can be written in infinitely many coordinate systems. It can be useful to have the freedom to choose any coordinates that are convenient to solve the field equations (e.g. with some specific symmetries), but the meaning of the solutions obtained this way can be extremely obscured by the choice of coordinates.

In order to demonstrate how these two issues complicate the understanding of spacetimes, we will breifly discuss here two specific solutions, the Curzon-Chazy metric, and the McVittie metric. Later in Chapters 2, 4 and 5, these solutions will be thoroughly analyzed.

1.1.1 The Curzon-Chazy Solution

This metric is the topic of Chapter 2, so for a thorough review of this solution, refer to that chapter and references within. In simple terms, the Curzon-Chazy metric is a static, axisymmetric vacuum solution of Eienstein's field equations (1.1). It can be written in the Weyl canonical coordinates as

$$ds^2 = -e^{-2m/\sqrt{\rho^2+z^2}}\,dt^2 + e^{2m/\sqrt{\rho^2+z^2}}\left(e^{-[m\rho/(\rho^2+z^2)]^2}\left(d\rho^2+dz^2\right)+\rho^2 d\phi^2\right), \quad (1.2)$$

where $m > 0$, which is understood to be the mass of the source of the metric at $(\rho, z) = (0, 0)$. Although this solution was discovered back in 1924, it has evaded thorough analysis for decades. It is a perfect example of how a smart choice of coordinates can simplify the field equations and provide us with a simple solution, but this choice of coordinates completely hides the meaning and true nature of the source of the gravitational field. The coordinates used above resemble cylindrical coordinates, which might be misleading. In the weak field limit, $g_{tt} \approx -\left(1 - 2\frac{m}{\sqrt{\rho^2+z^2}}\right)$, which

implies that in this limit, the corresponding Newtonian potential is $\Phi = \frac{-m}{\sqrt{\rho^2+z^2}}$. Since this potential resembles the one for a point mass, this might lead us to conclude that this metric describes the gravitational field produced by a point mass, or outside a spherical object. However, this would be correct only if ρ and z were truly cylindrical coordinates, but they most certainly are not. Furthermore, the Schwarzschild spacetime is known to describe the gravitational field of a spherically symmetric object or a point mass, and these two spacetimes are not isometric. The Schwarzschild metric can be transformed and written in Weyl coordinates, and it does not equal equation (1.2). This leaves us with a puzzle: What does a simple looking vacuum solution such as the Curzon-Chazy metric mean?

The fact that this question has not been answered for many decades demonstrates the need for additional relativistic tools to analyze spacetimes in general. The coordinate confusion present in this metric requires a coordinate independent way of analyzing solutions. In Section 1.3 we introduce a new tool based on analyzing the gradient fields of curvature invariants. We apply this tool and use it to thoroughly explore the Curzon-Chazy spacetime in Chapter 2, and conclude that it most resembles a non-rotating ring.

1.1.2 The McVittie Solution

Before introducing the McVittie solution, we will first briefly present the Schwarzschild metric, and the Friedman-Lemaitre-Robertson-Walker (FLRW) metric. The Schwarzschild solution describes the gravitational field outside a spherically symmetric object or a black hole of mass m, and can be be written as

$$ds^2 = -\left(1 - \frac{2m}{r}\right) dt^2 + \left(1 - \frac{2m}{r}\right)^{-1} dr^2 + r^2 \left(d\theta^2 + \sin^2\theta d\phi^2\right). \tag{1.3}$$

The FLRW metric is the foundation of modern cosmology, and it describes the spacetime of homogeneous and isotropic universe. It is usually written in comoving coordinates as

$$ds^2 = -dt^2 + a^2(t)\left(\frac{dr^2}{1-kr^2} + r^2\left(d\theta^2 + \sin^2\theta d\phi^2\right)\right), \tag{1.4}$$

where $a(t)$ is the scale factor function, determined by the constituents of the universe, and k is a constant representing the spacial curvature. These two spacetimes are milestones in gravitational physics and cosmology and thorough analysis of each can be found in many standard and advanced textbooks [2, 3, 6]. However, since we have two well established and understood solutions, is it possible to combine them? In other words, is it possible to use the two solutions to construct a metric that describes the gravitational field outside a black hole or spherically symmetric object that is embedded in an isotropic universe?

As mentioned above, the non-linearity of the field equations makes the task nearly impossible. We cannot simply add the two metrics, and more troubling, there is not a systematic way to combine the two solutions to produce a new physically meaningful one. However, one attempt to do so is the McVittie solution, which can be written as

$$ds^2 = -\left(\frac{1-m/2u}{1+m/2u}\right)^2 dt^2 + e^{\beta(t)}(1+m/2u)^4\left(dr^2 + r^2\left(d\theta^2 + \sin^2\theta d\phi^2\right)\right), \tag{1.5}$$

where $u \equiv re^{\beta/2}$, m is a positive constant. Interestingly, for a constant β, the solution reduces to the Schwarzschild metric (different coordinates than the ones used above), and for $m = 0$, the metric reduces to the spatially flat FLRW metric (i.e. $k = 0$, and note that $a(t) = e^{\beta(t)/2}$). The fact that this solution simplifies to the desired metrics at the desired limits does not guarantee that it physically represents the combination

of these two limits. In Chapters 4 and 5, we thoroughly explore the global structure of the McVittie metric after developing a numerical tool to produce accurate conformal Penrose diagrams for the first time for this spacetime. The casual structure revealed by these diagrams confirms the long held suspicion that this solution indeed describes the spacetime of a black hole embedded in an isotropic universe.

1.2 The Riemann Tensor and its Invariants

Within the mathematical context of general relativity, a solution to Einstein's field equations given by a metric tensor $g_{\mu\nu}$ represents a 4-d semi-Riemannian manifold (M, g). Scalar invariants can be constructed from contractions of the metric tensor and its partial derivatives. The number of algebraically independent invariants that can be constructed in 4-d spacetimes considering only up to second partial derivatives of the metric tensor (i.e. no derivatives of the Riemann or Weyl tensors) is still an active field of research from a mathematical point of view. However we will use the list of 16 scalars proposed by Carminati and McLenaghan (CM scalars) [7], which is becoming widely adopted in the relativity community to some extent. Note that the completeness of the set has not been proven. However, we will show below that even if additional invariants do exist, it turns out that any higher orders of contractions will not be of interest to the analysis tool we present in the following sections. The list of invariants is constructed from various contractions of the Riemann curvature tensor. We will present the list in the tensor formalism. First, find the Christoffel symbol of the second kind:

$$\Gamma^{\lambda}_{\ \mu\nu} \equiv \tfrac{1}{2} g^{\lambda k} \left(\frac{\partial g_{k\nu}}{\partial x^{\mu}} + \frac{\partial g_{k\mu}}{\partial x^{\nu}} - \frac{\partial g_{\mu\nu}}{\partial x^{k}} \right) . \tag{1.6}$$

The Riemann curvature tensor is defined as

$$R^{\lambda}_{\ \mu\nu k} \equiv \frac{\partial \Gamma^{\lambda}_{\mu\nu}}{\partial x^{k}} - \frac{\partial \Gamma^{\lambda}_{\mu k}}{\partial x^{\nu}} + \Gamma^{\eta}_{\mu\nu} \Gamma^{\lambda}_{k\eta} - \Gamma^{\eta}_{\mu k} \Gamma^{\lambda}_{\nu\eta} . \tag{1.7}$$

The Ricci curvature tensor is defined as

$$R_{\mu\nu} \equiv R^{\lambda}_{\ \mu\lambda\nu} , \tag{1.8}$$

and the Ricci scalar is

$$R = g^{\mu\nu} R_{\mu\nu} = R^{\nu}_{\ \nu} . \tag{1.9}$$

The Ricci scalar is the first invariant in the CM list. Note that we can think of the Ricci tensor and Ricci scalar as the "trace" components of the Riemann tensor. Next, we define Weyl tensor, which can be understood as the "trace-free" part of the Riemann tensor:

$$C_{\alpha\beta\mu\nu} \equiv R_{\alpha\beta\mu\nu} - \left\{ (g_{\alpha[\mu} R_{\nu]\beta} - g_{\beta[\mu} R_{\nu]\alpha}) - \frac{R}{3} g_{\alpha[\mu} g_{\nu]\beta} \right\} . \tag{1.10}$$

The dual of the Weyl tensor is defined as

$$C^{*}_{\mu\nu k\lambda} \equiv \frac{1}{2} \sqrt{-g}\ \epsilon_{\mu\nu\delta\gamma} C^{\delta\gamma}_{\ \ k\lambda} , \tag{1.11}$$

where $\epsilon_{\mu\nu k\lambda}$ is the four dimensional Levi-Civita symbol, which is defined as

$$\epsilon_{\mu\nu k\lambda} = \begin{cases} +1 & \text{if } (\mu,\nu,k,\lambda) \text{ is an even permutation of } (1,2,3,4) \\ -1 & \text{if } (\mu,\nu,k,\lambda) \text{ is an odd permutation of } (1,2,3,4) \\ 0 & \text{otherwise} \end{cases} \tag{1.12}$$

Now we are ready to define the next four scalars, called the Weyl invariants.

$$w1R \equiv \frac{1}{8} C_{\alpha\beta\gamma\delta} C^{\alpha\beta\gamma\delta} \tag{1.13}$$

and

$$w1I \equiv \frac{1}{8} C^{*}_{\alpha\beta\gamma\delta} C^{\alpha\beta\gamma\delta} \ , \tag{1.14}$$

where the two scalars above are usually presented as the real and imaginary parts of the complex first Weyl invariant[1], $w1 = w1R + i\, w1I$. Also,

$$w2R \equiv -\frac{1}{16} C_{\alpha\beta}{}^{\gamma\delta} C_{\gamma\delta}{}^{\epsilon\zeta} C_{\epsilon\zeta}{}^{\alpha\beta} \tag{1.15}$$

and

$$w2I \equiv -\frac{1}{16} C^{*}_{\alpha\beta}{}^{\gamma\delta} C_{\gamma\delta}{}^{\epsilon\zeta} C_{\epsilon\zeta}{}^{\alpha\beta} \ , \tag{1.16}$$

similarly are usually presented as the real and imaginary parts of the complex second Weyl invariant, $w2 = w2R + i\, w2I$. Alternatively, the four Weyl invariants can be expressed in terms of the "electric" and "magnetic" parts of the Weyl tensor. The electric part is defined as

$$E_{\mu\nu} \equiv C_{\mu\beta\nu\delta} u^{\beta} u^{\delta} \ , \tag{1.17}$$

and the magnetic part is

$$B_{\mu\nu} \equiv C^{*}_{\mu\beta\nu\delta} u^{\beta} u^{\delta} \ , \tag{1.18}$$

where u^{μ} is an arbitrary timelike vector. The four Weyl invariants can now be expressed in the following way [8]

[1]In vacuum, where $R = 0$ and $R_{\mu\nu} = 0$, the Riemann tensor equals the Weyl tensor. Therefore, $w1R = \frac{1}{8} C_{\alpha\beta\gamma\delta} C^{\alpha\beta\gamma\delta} = \frac{1}{8} R_{\alpha\beta\gamma\delta} R^{\alpha\beta\gamma\delta} = \frac{1}{8} K$, where K is the Kretschmann scalar. In older literature the Kretschmann scalar was widely used, but it is not considered a fundamental independent invariant in the formalism presented here.

$$w1R = \frac{1}{16}(E_{\alpha\beta}E^{\alpha\beta} - B_{\alpha\beta}B^{\alpha\beta}) \ , \tag{1.19}$$

$$w1I = \frac{1}{8}(E_{\alpha\beta}B^{\alpha\beta}) \ , \tag{1.20}$$

$$w2R = \frac{1}{32}\left(3E^{\alpha}_{\beta}B^{\beta}_{\gamma}B^{\gamma}_{\alpha} - E^{\alpha}_{\beta}E^{\beta}_{\gamma}E^{\gamma}_{\alpha}\right) \tag{1.21}$$

and

$$w2I = \frac{1}{32}\left(B^{\alpha}_{\beta}B^{\beta}_{\gamma}B^{\gamma}_{\alpha} - 3E^{\alpha}_{\beta}E^{\beta}_{\gamma}B^{\gamma}_{\alpha}\right) \ . \tag{1.22}$$

We can see one of the reasons these tensor are called the electric and magnetic components of Weyl, since now the Weyl invariants above 1.19, and 1.20 resemble the Lorentz invariants of electromagnetism (i.e. $\mathbf{E}^2 - \mathbf{B}^2$, and $\mathbf{E} \cdot \mathbf{B}$). However, in the context of general relativity, the electric part of the Weyl tensor contains information about the tidal forces produced by the spacetime, while the magnetic part contains information about the frame-dragging forces, and spin-spin interactions. Therefore, the Weyl curvature invariants actually represent the cumulative tidal and frame-dragging effects of the spacetime. In other words, these invariants describe the strength of the tidal and frame-dragging forces produced in all directions collectively at each point, but we lose the directional sense of these effects in the process.

The invariants listed so far will be the main focus of the spacetime analysis and visualization in Chapters 2 and 3, where we examine the Curzon-Chazy metric, and the Kerr metric, both vacuum solutions. However there are 11 remaining invariants in the CM scalars list, and we present them here for completeness. To proceed we

need to introduce the "trace-free" Ricci tensor

$$S_{\mu\nu} \equiv R_{\mu\nu} - \frac{1}{4} R g_{\mu\nu} \ . \tag{1.23}$$

There are three other Ricci invariants

$$r_1 \equiv \frac{1}{4} S^{\alpha}{}_{\beta} S^{\beta}{}_{\alpha} \ , \tag{1.24}$$

$$r_2 \equiv -\frac{1}{8} S^{\alpha}{}_{\beta} S^{\beta}{}_{\gamma} S^{\gamma}{}_{\alpha} \tag{1.25}$$

and

$$r_3 \equiv \frac{1}{16} S^{\alpha}{}_{\beta} S^{\beta}{}_{\gamma} S^{\gamma}{}_{\delta} S^{\delta}{}_{\alpha} \ . \tag{1.26}$$

It can be shown that any Ricci invariant, r_n, with $n > 3$ is not algebraically independent, but can be written in terms of r_1, r_2 and r_3 defined above [9]. Therefore, any higher order invariant r_n is irrelevant to the CM list of independent invariants. Eight scalars remain, constructed by contracting a combination of the Weyl tensor and the trace-free Ricci tensor:

$$m1R \equiv \frac{1}{8} C_{\alpha\beta\gamma\delta} S^{\alpha\delta} S^{\beta\gamma} \tag{1.27}$$

$$m1I \equiv \frac{1}{8} C^{*}_{\alpha\beta\gamma\delta} S^{\alpha\delta} S^{\beta\gamma} \tag{1.28}$$

$$m2R \equiv \frac{1}{16} \left(C_{abcd} \, C^{aefd} - C^{*}_{acdb} \, C^{*aefd} \right) S^{bc} \, S_{ef} \tag{1.29}$$

$$m2I \equiv \frac{1}{8} C^{*}_{abcd} \, C^{aefd} \, S^{bc} \, S_{ef} \tag{1.30}$$

$$m3 \equiv \frac{1}{16}\left(C_{abcd}\, C^{aefd} + C^{*}_{acdb}\, C^{*\,aefd}\right) S^{bc}\, S_{ef} \tag{1.31}$$

$$m4 \equiv -\frac{1}{32}\left(C_{ac}{}^{db}\, C_{befg} + C^{*}_{ac}{}^{db}\, C^{*\,befg}\right) S^{ag}\, S^{ef}\, S^{c}{}_{d} \tag{1.32}$$

$$m5R \equiv \frac{1}{32}\left(C_{acdb}\, C_{gefh} + C^{*}_{acdb}\, C^{*}_{gefh}\right) C^{aghb}\, S^{cd}\, S^{ef} \tag{1.33}$$

$$m5I \equiv \frac{1}{32}\left(C_{acdb}\, C_{gefh} + C^{*}_{acdb}\, C^{*}_{gefh}\right) C^{*\,aghb}\, S^{cd}\, S^{ef} \tag{1.34}$$

For vacuum solutions, $R = 0$, and $R_{\mu\nu} = 0$, so $S_{\mu\nu} = 0$ as well. Therefore, 12 of the 16 CM invariants vanish, and the four Weyl invariants are the only non-vanishing ones. This is the case for the Curzon-Chazy metric, the subject of Chapter 2, and the Kerr metric, the subject of Chapter 3.

1.3 A New Approach to Analyze Spacetimes

1.3.1 Gradient Fields of Curvature Invariants

The first spacetime analysis tool we explore in this thesis is based on a thorough examination of the gradient fields of the curvature scalar invariants, and was introduced in [10]. Consider a curvature invariant $\mathcal{I}$, then the associated gradient field k_μ is defined as the covariant derivative of the invariant

$$k_\mu \equiv -\nabla_\mu \mathcal{I} = -\frac{\partial \mathcal{I}}{\partial x^\mu}\,. \tag{1.35}$$

The resulting vector fields are not geodesics of the metric in general, and actually can be timelike, null or spacelike in different regions of the spacetime. These gradient flows provide an unprecedented level of understanding the underlying geometry and physics of spacetimes. The images produced by visualizing these gradient flows give an intuitive picture of the spacetime curvature associated with each invariant, where the flowlines seek the extrema of the associated scalar. In Chapter 2 we apply this tool to the Curzon-Chazy metric (section 1.1.1), revealing a rich structure that resembles that of a non-rotating ring. In Chapter 3 we analyze the celebrated and thoroughly studied Kerr metric, and discover fundamental and unknown properties of that spacetime. We focus our analysis on the critical points of the fields, and the unique flowlines connecting these critical points, or connecting a critical point to a singular point (i.e. a point where k_μ is undefined).

1.3.2 Critical Points Classification and Winding Numbers

Critical points, defined as points where the field vanishes, are one of the most important aspects of a vector field to be examined. In standard vector fields in Euclidean geometry, the procedure to analyze and classify critical points resulting from a gradient field of a scalar is well established [11], where they can be classified into different types of nodes, and represent extrema or saddle points of that scalar. However, the gradient fields we analyze here are in curved spacetimes. Therefore, a generalization of the standard analysis of critical points in curved spacetimes was developed in [10], and in this section we summarize this generalization.

The new classification procedure is properly formulated within the mathematical context of pseudo-Riemannian geometry, and most importantly, the entire procedure

is coordinate-independent. As defined above 1.35, we consider the covariant gradient field of a scalar $k_\mu = -\nabla_\mu \mathcal{I}$. A critical point $\mathcal{P}$ is a point where $k_\mu = 0$. Note that $k^\mu = k_\nu g^{\nu\mu} = 0$ at any $\mathcal{P}$. However, the inverse is not true. It is possible to have a point where $g^{\nu\mu} = 0$, which leads to $k^\mu = 0$, but is not a genuine critical point of the scalar $\mathcal{I}$. In this case the contravariant field vanishes because of a coordinate artifact. Therefore, it is crucial for the entire analysis to be constructed in a covariant form, in order to guarantee that the result is always coordinate independent. The covariant Hessian is defined as

$$H_{\mu\nu} \equiv -\nabla_\mu k_\nu. \tag{1.36}$$

The determinant of the Hessian, $H \equiv \det(H_{\mu\nu})$, is a scalar density. In other words, for a coordinate transformation $x'^\nu(x^\mu)$, we get $H' = \mathcal{J}^2 H$, where $\mathcal{J}$ is the Jacobian. Therefore, the sign of the determinant is coordinate-independent, which is crucial to the classification procedure.

For simple spacetimes, especially the ones with some symmetries, it is possible to have $H|_\mathcal{P} = 0$ for the entire spacetime, as we will see in Chapters 2 and 3. This occurs as a result of one or more components of k_μ vanishing for the entire spacetime. In such cases we have to restrict the critical point classification analysis to the subspace associated with the gradient field [2]. Taking into consideration the appropriate subspace, we have 3 possibilities for the classification of $\mathcal{P}$: a local minimum, a local maximum, or a saddle point. However, at a critical point the covariant Hessian reduces to the

[2]Nonetheless, it is important to note the the calculations for k_μ must be done in the full spacetime, just like the calculations for the spacetime invariants.

standard Hessian [3], this allows us to use the same procedure from standard mathematical analysis. In order to find whether $\mathcal{I}$ has a local minimum or maximum at $\mathcal{P}$, we apply the following theorem [11]. If $H|_{\mathcal{P}} = 0$, then the procedure is inconclusive and $\mathcal{P}$ is a degenerate critical point. Otherwise, $\mathcal{P}$ is non-degenerate, and we proceed in the following way. Let n go from 0 to d, where d is the number of dimensions of the subspace under consideration. Let $\Delta_0 = 1$, and for $n > 0$, $\Delta_n = \det(H_{ij})$, where H_{ij} is a the submatrix containing only the first n-th rows and columns of of $H_{\mu\nu}$ (i.e. $i, j = 1...n$). If the $d + 1$ numbers $\Delta_0, \Delta_1, ..., \Delta_d$ are all positive, then $\mathcal{I}$ has a local minimum at $\mathcal{P}$. If these numbers are alternating positive and negative, then $\mathcal{I}$ has a local maximum at $\mathcal{P}$. Otherwise, $\mathcal{P}$ is a saddle point. To summarize:

- If $H|_{\mathcal{P}} = 0$, the critical point $\mathcal{P}$ is degenerate, and the classification procedure is inconclusive.
- If the $d+1$ numbers $\Delta_0, \Delta_1, ..., \Delta_d$ are all positive, then $\mathcal{I}$ has a local minimum at $\mathcal{P}$, and this point is an asymptotically stable node of the field.
- If the $d + 1$ numbers $\Delta_0, \Delta_1, ..., \Delta_d$ are alternative positive and negative, then $\mathcal{I}$ has a local maximum at $\mathcal{P}$, and this point is unstable node of the field.
- Otherwise, the critical point $\mathcal{P}$ is a saddle point.

Another property of critical and singular points that we examine is the associated winding number, or index. For a two-dimensional flow, the winding number of a critical point can be evaluated through the following integral

$$I = \frac{1}{2\pi} \int_C d\theta$$

[3] At a critical point $\mathcal{P}$, the covariant derivative of the field $\nabla_\mu k_\nu = \partial k_\nu / \partial x^\mu - \Gamma^\lambda_{\mu\nu} k_\lambda = \partial k_\nu / \partial x^\mu$, because $k_\lambda(\mathcal{P}) = 0$. Therefore, the covariant Hessian reduces to the standard partial derivative Hessian.

where $\theta = tan^{-1}\left(\frac{v_y}{v_x}\right)$, for any vector field $\vec{v}$, and the loop C can be any loop that encloses only the critical point around which the winding number is calculated. There is some connection between the classification of a critical point and its index:

- The index of a node, source or sink is $+1$.
- The index of a saddle point is -1.
- The index of a closed curve containing critical points is equal to the sum of the indices of the critical points within.

These indices are very useful in qualitatively comparing the behavior of fields of different spacetimes, and different gravity theories altogether, as we can see in Chapter 2. Furthermore, the indices play a major role in the Poincaré - Hopf theorem, which states that the sum of the indices over all the isolated critical points equals the Euler characteristic index of the spacetime.

1.3.3 The Newtonian analog

In order to construct a Newtonian analog to the gradient fields presented in the previous section, first we need to establish the Newtonian equivalent to the Riemann curvature tensor $R_{\alpha\beta\mu\nu}$ as well as the Weyl tensor $C_{\alpha\beta\mu\nu}$. For a thorough review see [12] and references within, here we will summarize the argument. The Riemann tensor directly provides information about the tidal forces (i.e geodesic deviations) that a spacetime exerts at each point. Specifically, the tidal forces in General Relativity are given by $\frac{D^2}{D\tau^2}\delta x^\alpha = -R^\alpha{}_{\beta\mu\nu}\, u^\beta \delta x^\mu u^\nu$, where $u^\mu = \frac{dx^\mu}{d\tau}$, and $\frac{D}{D\tau}$ is the covariant derivative along u^μ. On the other hand, the Newtonian tidal forces are calculated through the Hessian of the gravitational potential. The Newtonian tidal tensor is

defined as $\mathcal{T}_{ij} \equiv \nabla_i \nabla_j \Phi = \Phi_{,i,j}$. The tidal forces are then given by $\frac{d^2}{dt^2}\delta x^i = -\mathcal{T}_{ij}\ \delta x^j$. Therefore, we can see that $\mathcal{T}_{ij}$ is the suitable Newtonian analog to $R_{\alpha\beta\mu\nu}$. The Riemann tensor has 20 independent components, while $\mathcal{T}_{ij}$ has 6 independent ones. The Riemann tensor can be separated into two parts; the first one is the trace part with 10 independent component contained in the Ricci tensor and Ricci scalar. The second part, the trace free part, with the remaining 10 independent components is the Weyl tensor $C_{\alpha\beta\mu\nu}$ defined as

$$\underbrace{C_{\alpha\beta\mu\nu}}_{\text{trace free part}} \equiv R_{\alpha\beta\mu\nu} - \underbrace{\left\{ (g_{\alpha[\mu}R_{\nu]\beta} - g_{\beta[\mu}R_{\nu]\alpha}) - \frac{R}{3} g_{\alpha[\mu}g_{\nu]\beta} \right\}}_{\text{trace part}} . \tag{1.37}$$

The Weyl tensor has all the symmetries of the Riemann tensor, as well as the property that it is trace free by construction, namely $C^{\alpha}{}_{\mu\alpha\nu} = 0$. Similarly, we can separate the Newtonian analog of the Riemann tensor ($\mathcal{T}_{ij}$), into two parts, and define the Newtonian analog to the Weyl tensor in the following way

$$\underbrace{E_{ij}}_{\text{trace free part}} \equiv \mathcal{T}_{ij} - \underbrace{\frac{1}{3} h_{ij}\mathcal{T}^{k}{}_{k}}_{\text{trace part}} , \tag{1.38}$$

where h_{ij} is the Euclidean metric tensor, and note that by constructtion, E_{ij} is trace free (i.e. $E^{i}{}_{i} = 0$). In this context, the Newtonian analog to the Weyl first and second invariants are [4]

$$w1_{Newtonian} \equiv \frac{1}{16} E_{ij}E^{ij} \tag{1.39}$$

$$w2_{Newtonian} \equiv -\frac{1}{32} E_{i}{}^{j}E_{j}{}^{k}E_{k}{}^{i} \tag{1.40}$$

It is important to note that there is no Newtonian equivalent to the magnetic part of the Weyl tensor. Standard Newtonian gravity has no frame-dragging forces

[4] We can also construct the analog to the Kretschmann scalar, where $K_{Newtonian} \equiv \mathcal{T}_{ij}\mathcal{T}^{ij}$.

or spin-spin interactions, only tidal forces. The Newtonian analog to the Weyl tensor introduced above can be thought of as pure electric. Therefore, we can only construct analog invariants for the "electric" part of the gravitational field. By finding the gradient fields of the Newtonian analog to the Weyl invariants, we can visualize the Newtonian gravitational field of any density distribution or potential in an analogous way to the general relativistic tool introduced in the previous section.

1.4 References

[1] D. Howard and J. Stachel, "*Einstein and the history of general relativity*", Birkhuser (1989).

[2] S. Weinberg, "*Gravitation and Cosmology: Principles and Applications of the General Theory of Relativity*", John Wiley & Sons (1972).

[3] J. Plebanski and Andrzej Krasinski, "*An Introduction to General Relativity and Cosmolog*", Cambridge University Press (2006).

[4] S. S. Doeleman et al., Nature, **455**, 7209 (2008).

[5] S. S. Doeleman et al., Science, **338**, 6105 (2012).

[6] E. Poisson, "*A Relativist's Toolkit: The Mathematics of Black-Hole Mechanics*", Cambridge University Press, Cambridge (2004).

[7] J. Carminati and R. G. McLenaghan, J. Math. Phys, **32**, 3135 (1991).

[8] See the reprint, L. Bel, General Relativity and Gravitation **32**, 10, 2047 (2000).

[9] K. Santosuosso, D. Pollney, N. Pelavas, P. Musgrave and K. Lake, "*Invariants of the Riemann tensor for class B warped product space-times*", Computer Physics Communications ,**115**, 2-3 (1998).

[10] K. Lake, "Visualizing Spacetime Curvature via Gradient Flows I: Introduction", Phys. Rev. D, **86**, 10 (2012).

[11] T. M. Apostol, "*Mathematical Analysis*" Addison-Wesley, London (1964).

[12] G. Ellis, "*Republication of: Relativistic cosmology*", General Relativity and Gravitation, **41**, 3 (2009).

Chapter 2

Paper I: The Curzon-Chazy metric and Non-Rotating Rings

Paper Title[1]: "Visualizing Spacetime Curvature via Gradient Flows II: An Example of the Construction of a Newtonian analogue"

[1]This chapter contains a version of a paper published in Physical Review D as: Majd Abdelqader and Kayll Lake, Physical Review D **86**, 12, 124037 (2012).

2.1 Abstract

This is the first in a series of papers in which the gradient flows of fundamental curvature invariants are used to formulate a visualization of curvature. We start with the construction of strict Newtonian analogues (not limits) of solutions to Einstein's equations based on the topology of the associated gradient flows. We do not start with any easy case. Rather, we start with the Curzon - Chazy solution, which, as history shows, is one of the most difficult exact solutions to Einstein's equations to interpret physically. A substantial part of our analysis is that of the Curzon - Chazy solution itself. Eventually we show that the entire field of the Curzon - Chazy solution, up to a region very "close" to the the intrinsic singularity, strictly represents that of a Newtonian ring, as has long been suspected. In this regard, we consider our approach very successful. As regards the local structure of the singularity of the Curzon - Chazy solution within a fully general relativistic analysis, however, whereas we make some advances, the full structure of this singularity remains incompletely resolved.

2.2 Introduction

Perhaps the most familiar example of an exact solution to Einstein's equations, generated by way of a Newtonian "analogue", is the Curzon - Chazy solution wherein the Laplacian for a point mass in a fictitious Euclidean 3 - space is used to generate an exact static axially symmetric vacuum solution of Einstein's equations. Unfortunately, the Curzon - Chazy solution bears little resemblance to a point mass. Indeed, its singularity structure appears, at present, to be at least as complicated as that of the Kerr solution.

In this paper, following the introduction given by [1], we consider the gradient fields of the two non-differential invariants of the Curzon - Chazy solution. These alone reveal previously unknown properties of the solution. Further, following the procedure given in [1] for the construction of strict Newtonian analogues, based on gradient flows, we suggest, and explain in a quantitative way, that a pure Newtonian ring is "almost" a complete analogue of the Curzon - Chazy solution. Whereas our main aim here is the construction of the analogue, we have had to do a fair amount of analysis of the Curzon - Chazy solution itself.

2.3 The Curzon-Chazy Metric

The line element for a static and axially symmetric spacetime can be written in Weyl's canonical coordinates [2]

$$ds^2 = -e^{2U}\,dt^2 + e^{-2U}\left(e^{2\gamma}\left(d\rho^2 + dz^2\right) + \rho^2 d\phi^2\right)\ , \tag{2.1}$$

where U and γ are functions of ρ and z. It is well known that these coordinates do not behave like typical cylindrical coordinates. Einstein's field equations in vacuum with zero cosmological constant give the following *linear* partial differential equation for U,

$$\frac{\partial^2 U}{\partial \rho^2} + \frac{1}{\rho}\frac{\partial U}{\partial \rho} + \frac{\partial^2 U}{\partial z^2} = 0. \tag{2.2}$$

Equation (2.2) is Laplace's equation in a Euclidean 3-space in cylindrical polar coordinates. The general solution to (2.2) can be written out and the associated Einstein equations

$$\frac{\partial \gamma}{\partial \rho} = \rho\left(\left(\frac{\partial U}{\partial \rho}\right)^2 - \left(\frac{\partial U}{\partial z}\right)^2\right), \quad \frac{\partial \gamma}{\partial z} = 2\rho\frac{\partial U}{\partial \rho}\frac{\partial U}{\partial z} \tag{2.3}$$

can be considered solved. Since in the weak field we have $g_{tt} \sim -(1+2U)$, it is tempting to consider a solution-generating procedure wherein one takes a known Newtonian potential U (in an unphysical Euclidean 3-space), and solves (2.3) for γ. We then have an exact solution to Einstein's equations. Unfortunately, the resultant Weyl solution bears little similarity to the Newtonian solution and the physical meaning of most Weyl solutions so produced remain unclear. The culprit is the *non-linearity* of Einstein's equations that enters via (2.3).

The Curzon [3] - Chazy [4] solution (CC hereafter) is one of the simplest special cases of the Weyl metric (2.1).[2] The potential is taken to be the Newtonian potential of a point mass (m) at the center of a fictitious Euclidean 3-space, $\rho = z = 0$,

$$U = -\frac{m}{\sqrt{\rho^2 + z^2}}, \quad m > 0. \tag{2.4}$$

With (2.4) it follows from (2.3) that

$$\gamma = -\frac{m^2\rho^2}{2(\rho^2 + z^2)^2}. \tag{2.5}$$

The resultant metric components are well defined except at $(\rho, z) = (0, 0)$. The circumference of a trajectory of constant t, ρ and z is equal to $2\pi\rho\, e^{m/\sqrt{\rho^2+z^2}}$, which behaves like Euclidean cylindrical coordinates for ρ/m or $z/m \gg 1$, but the circumference diverges in the plane $z = 0$ as ρ goes to zero. Further, the meaning of m in the CC solution is no longer obvious.

Since the CC solution is a vacuum solution, the Ricci and mixed invariants vanish. There are then only 4 Weyl invariants to consider [1]. Moreover, since the CC solution is static, it is a purely electric spacetime (all magnetic components of the Weyl tensor

[2]For a review see [5].

vanish). We are left with only two invariants to consider,

$$w1R = \frac{1}{16} E_{\alpha\beta} E^{\alpha\beta} \tag{2.6}$$

and

$$w2R = -\frac{1}{32} E^{\alpha}_{\beta} E^{\gamma}_{\alpha} E^{\beta}_{\gamma}. \tag{2.7}$$

For convenience, define

$$r^2 = \rho^2 + z^2. \tag{2.8}$$

We find

$$w1R = 2\,m^2 \exp\left(\frac{2m\rho^2}{r^4}\right) \frac{\left(3\,r^6 - 6\,mr^5 + 3\,m^2r^4 + 3\,m^2\rho^2r^2 - 3\,\rho^2m^3r + \rho^2m^4\right)}{r^{12}\left(e^{\frac{m}{r}}\right)^4} \tag{2.9}$$

and

$$w2R = 3\,m^3 \exp\left(\frac{3m^2\rho^2}{r^4}\right) \frac{(m-r)\left(2\,r^6 - 4\,mr^5 + 2\,m^2r^4 + 3\,m^2r^2\rho^2 - 3\,\rho^2m^3r + \rho^2m^4\right)}{r^{16}\left(e^{\frac{m}{r}}\right)^6}. \tag{2.10}$$

At first glance, it would appear that $r = 0$ is singular. However, along $\rho = 0$, we note that

$$\chi \equiv -\frac{w2R}{6}\bigg|_{\rho=0} = \left(\frac{w1R}{6}\right)^{3/2}\bigg|_{\rho=0} = \frac{m^3\,(z-m)^3}{z^{12}\left(e^{\frac{m}{z}}\right)^6} \tag{2.11}$$

and, in particular,

$$\lim_{z\to 0} \chi = 0. \tag{2.12}$$

Now, whereas χ has a local minimum ($= 0$) at $z = \pm m$, and a local maximum at $z = \pm(1 \pm 1/\sqrt{3})m$, it is clear that there is no scalar polynomial singularity along $\rho = 0$. Yet, more generally, except perhaps for selected trajectories, $w1R$ and $w2R$ both diverge at $\rho = z = 0$. The directional divergence of $w1R$ [3] was, as far as

[3]The older literature refers to the Kretschmann scalar, which, as explained in [1], is $8w1R$ here.

we know, first noticed by Gautreau and Anderson [6]. This observation generated much further consideration. In terms of "polar" coordinates (r, θ) $(\rho = r\sin(\theta), z = r\cos(\theta))$, Stachel [7] showed that the area of surfaces of constant t and r decreases with decreasing r up to a minimum (which can be shown to be $r/m \simeq 0.5389$) and then diverges as $r/m \to 0$. These surfaces can be shown to be topologically spherical. Cooperstock and Junevicus [8] showed that even trajectories of the simple form $z = C\rho^n$, where C and n are positive constants, give $w1R$ a rich structure. Further analysis of the geodesics followed in order to explore the singularity and the global structure of the metric [9], [10], [11], [12].[4] The general consensus is that the singularity has a "ring-like", rather than "point-like", structure. This is not so simple as it first sounds. The "ring" has finite radius but infinite circumference [10]. Rather remarkably late was the computation of $w2R$ in [13], a work which gave visual information on the CC metric based on the principal null directions. This procedure gives much less information than the visualization procedure considered here. More recently, Taylor [14] has suggested a technique for unravelling directional singularities.[5]

2.4 Gradient fields

As in [1] we define the gradient fields

$$k_n^\alpha \equiv -\nabla^\alpha \mathcal{I}_n = -g^{\alpha\beta}\frac{\partial \mathcal{I}_n}{\partial x^\beta}, \quad k_{n\,\alpha} = -\frac{\partial \mathcal{I}_n}{\partial x^\alpha}, \tag{2.13}$$

[4]It is remarkable that the simple coordinates used by Stachel (which we refer to as Stachel, rather than "polar" coordinates) have not been exploited further in the study of the CC metric. This is examined in Appendix A where the relevant results of Cooperstock and Junevicus, and Scott and Szekeres are generalized.

[5]Taylor's technique is not applicable to the CC solution due to a critical point along $\rho = 0$ as $z \to 0$.

where n labels the invariant and now

$$\mathcal{I}_1 = w1R, \quad \mathcal{I}_2 = w2R. \tag{2.14}$$

2.4.1 Stachel Coordinates

The explicit forms for the gradient fields are given in Appendix B in Stachel coordinates. Here we prefer to draw the flows explicitly in Weyl coordinates. There is no loss of information in doing this since the inverse transformations, $r = \sqrt{\rho^2 + z^2}, \theta = \arctan(\rho/z)$, are so simple.[6]

2.4.2 Weyl Coordinates

The First Weyl Invariant: $\mathcal{I}_1$ Along $\rho = 0$ we find

$$k_{1\,\alpha} = \frac{12m^2(3z^3\epsilon - 9z^2m + 8m^2z\epsilon - 2m^3)\epsilon}{z^{10}\exp(\frac{4m\epsilon}{z})}\delta^z_\alpha \tag{2.15}$$

where $\epsilon \equiv sign(z)$. The flow (2.15) has 7 critical points (ρ, z): $(0,0)$ (along $\rho = 0, z \to 0$), $(0, \pm m)$, $\left(0, \pm m(1 - 1/\sqrt{3})\right)$ and $\left(0, \pm m(1 + 1/\sqrt{3})\right)$. Note that the gradient field is undefined at $(0,0)$ (along $z = 0, \rho \to 0$). To classify these critical points we calculate the Hessian

$$H_{\alpha\beta} \equiv -\nabla_\alpha k_\beta. \tag{2.16}$$

Let H be the determinant of $H_{\alpha\beta}$. In the full spacetime it can be shown that $H = 0$ at all critical points. Similarly, in the 3 - dimensional subspace $\phi = constant$ again $H = 0$. In the $\rho - z$ plane we calculate

$$H = -\frac{m^4 h1h2}{z^{24}\exp\left(\frac{8m\epsilon}{z}\right)} \tag{2.17}$$

[6]That is, to view the flow in Stachel coordinates simply think of r as a circle centered on an origin at $\rho = z = 0$, and θ a straight line through the origin measured from 0 along the vertical to $\pi/2$ in the equatorial plane.

where

$$h1 \equiv 9\,\epsilon\, z^4 - 36\, m z^3 + 42\, m^2 \epsilon\, z^2 - 15\, m^3 z - m^4 \epsilon \tag{2.18}$$

and

$$h2 \equiv 21\,\epsilon\, z^4 - 87\, m z^3 + 117\, m^2 \epsilon\, z^2 - 60\, m^3 z + 10\, m^4 \epsilon. \tag{2.19}$$

Since

$$w1R = \frac{6\, m^2\, (z^2 - 2\, zm + \epsilon\, + m^2 \epsilon)}{\epsilon z^8 \exp\left(\frac{4m\epsilon}{z}\right)} \tag{2.20}$$

along $\rho = 0$, we are in a position to classify the critical points[7]: $(0, \pm m)$ (asymptotically stable nodes of index $+1$ and isotropic critical points [1] with $w1R = 0$), $\left(0, \pm m(1 - 1/\sqrt{3})\right)$ (hyperbolic saddle points of index -1), and $\left(0, \pm m(1 + 1/\sqrt{3})\right)$ (hyperbolic saddle points of index -1). The overall index for any hypersurface of constant t and ϕ is $+1$. The flow is shown in Figure 2.1 in the first quadrant only, since the metric is axially symmetric, as well as symmetric about the equatorial plane $(z \to -z)$.

[7]Since the flows are only two-dimensional, to find the winding number (i.e. index) of a critical point numerically, we evaluate the following integral

$$I = \frac{1}{2\pi} \int_C d\theta$$

where $\theta = tan^{-1}\left(\frac{v_y}{v_x}\right)$, for any vector field $\vec{v}$, and the loop C can be any loop that encloses only the critical point around which the winding number is calculated.

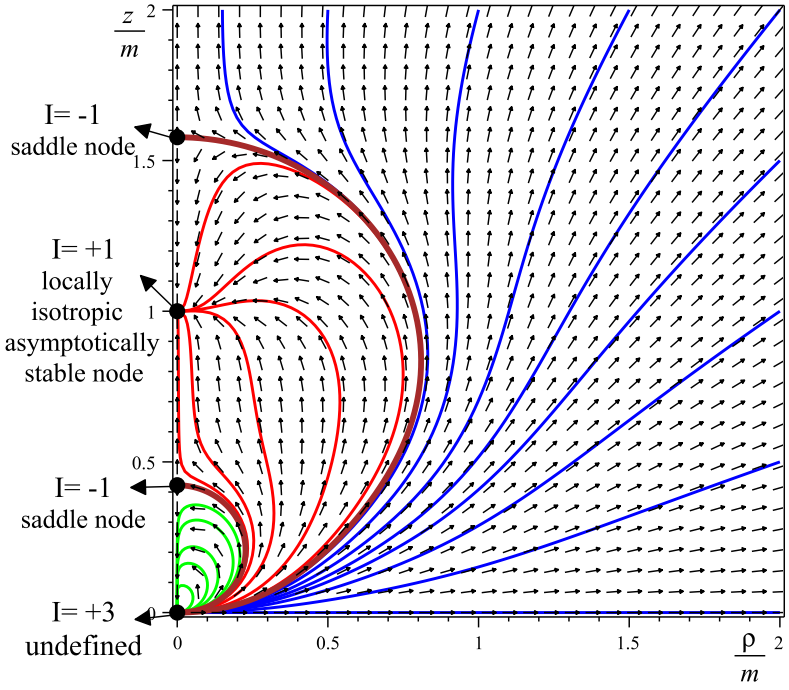

Figure 2.1: The gradient field $k_{1\,\alpha}$ of the Weyl invariant $w1R$ for the CC metric, presented in Weyl coordinates. The field is normalized for visual representation, and the flowlines are colored (online) to categorize them into distinct groups according to their global behavior (blue, red and green). Critical points are represented by black circles, and critical directions of the fields are brown. The character of the critical points along with their associated indices are shown and discussed in the text.

The Second Weyl Invariant: $\mathcal{I}_2$ Following the same procedure given above, for $\mathcal{I}_2$ along $\rho = 0$ we find the critical points: $(0, \pm m)$ (degenerate isotropic critical points of index 0), $\left(0, \pm m(1 - 1/\sqrt{3})\right)$ (hyperbolic saddle points of index -1), and $\left(0, \pm m(1 + 1/\sqrt{3})\right)$ (hyperbolic saddle points of index -1). In addition, along $z = 0$ we find critical points at $\rho \cong \pm 1.1101m$, asymptotically stable nodes of index $+1$. The overall index for any hypersurface of constant t and ϕ is again $+1$.[8] The flow is shown in Figure 2.2.

[8]Of course the indices must be calculated in the full "plane", for both positive and negative z and for $\phi = 0$ and $\phi = \pi$.

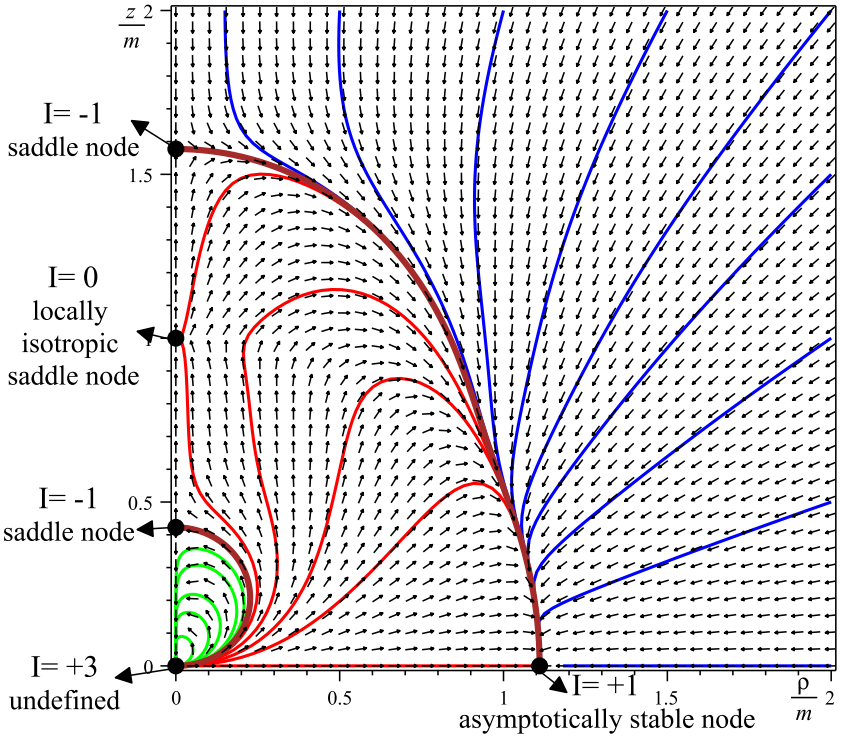

Figure 2.2: As in Figure 2.1 but for $k_{2\,\alpha}$.

2.4.3 Scott - Szekeres Unfolding

The unfolding of $(\rho, z) = (0, 0)$, given by Scott and Szekeres in [10] and [11], is reproduced in Appendix C. Spacelike infinity ($r \to \infty$) is mapped onto $0 \leq X \leq \pi$ with $Y = \pi/2$ and $X = \pi$ with $0 \leq Y \leq \pi/2$, the z axis maps onto $-\pi/2 < Y < \pi/2$ with $X = 0$ and the ρ axis onto $\pi/2 < X < \pi$ with $Y = 0$. Now $r = 0$ corresponds to $0 \leq X \leq \pi/2$ with $Y = -\pi/2$ *and* $X = \pi/2$ with $-\pi/2 \leq Y \leq 0$. The singularity of the CC metric is represented only by $X = \pi/2$ with $Y = 0$.The gradient fields of the CC metric, with this unfolding, are shown in Figures 2.3 and 2.4. The unfolding of the Weyl coordinate point $(0, 0)$ is now evident: All of the flowlines intersect the singularity $(X, Y) = (\pi/2, 0)$. The flowlines of the inner (green) region also intersect

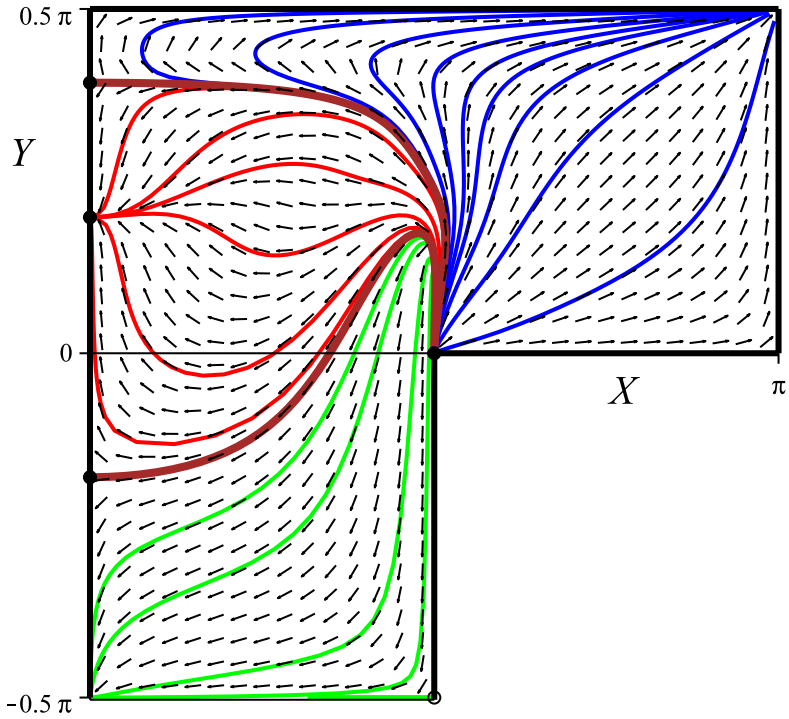

Figure 2.3: As in Figure 2.1 but with the Scott - Szekeres unfolding. All flow lines intersect the singularity at $(X, Y) = (\pi/2, 0)$. All green flow lines also intersect $(X, Y) = (\pi/2, -\pi/2)$ which is the critical point $(\rho, z) = (0, 0)$ along $\rho = 0, z \to 0$.

$(X, Y) = (\pi/2, -\pi/2)$.

2.4.4 A New Unfolding

Whereas the unfolding of $(\rho, z) = (0, 0)$ given by Scott and Szekeres accomplishes the task, the rather complicated procedure also modifies the entire spacetime representation. Here we seek a new unfolding of $(\rho, z) = (0, 0)$ which does not modify the spacetime in the large. It turns out that we need only modify ρ. On reviewing Appendix A we see that the most important term to consider is the exponent of $\sin(\theta)/x$

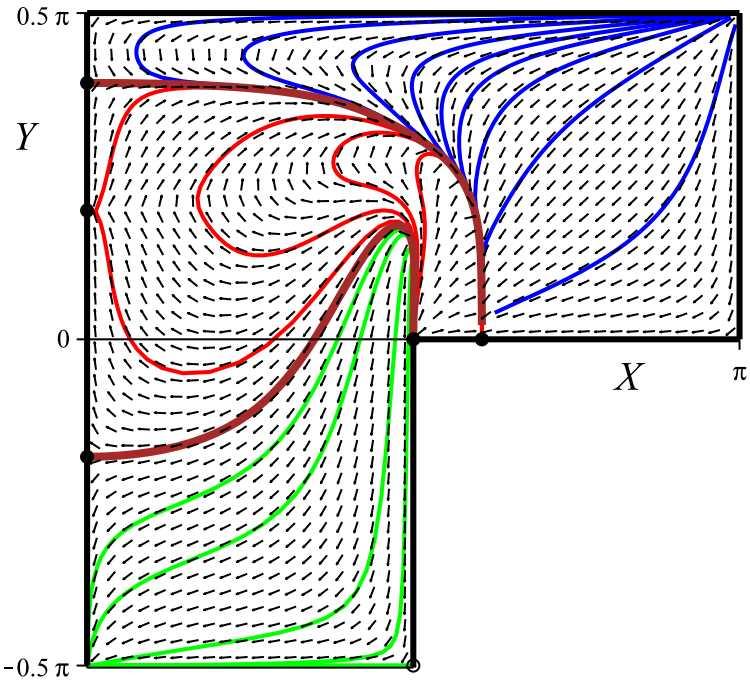

Figure 2.4: As in Figure 2.2 but with the Scott - Szekeres unfolding.

(where $x \equiv r/m$). We can write

$$\frac{\sin(\theta)}{x} = \frac{\rho m}{r^2}. \tag{2.21}$$

Now either this exponent diverges or it does not. If it diverges we can compactify this divergence with a tanh function. If it does not diverge we can set the term to zero by multiplying by ρ. Finally, let us require that the new ρ and old ρ approach each other for sufficiently large r. We arrive at the unfolding

$$\frac{\tilde{\rho}}{m} = \frac{\rho}{m} + \tanh\left(\frac{\rho}{m} e^{\rho m/r^2}\right)\left(1 - \tanh(\frac{r}{m})\right). \tag{2.22}$$

The singularity is at $(\tilde{\rho}, 0) = (m, 0)$ and the critical point is at $(\tilde{\rho}, 0) = (0, 0)$. No flow lines cross the "edge" $0 < \tilde{\rho} < m$ where $r = 0$. Indeed, whereas the trajectories

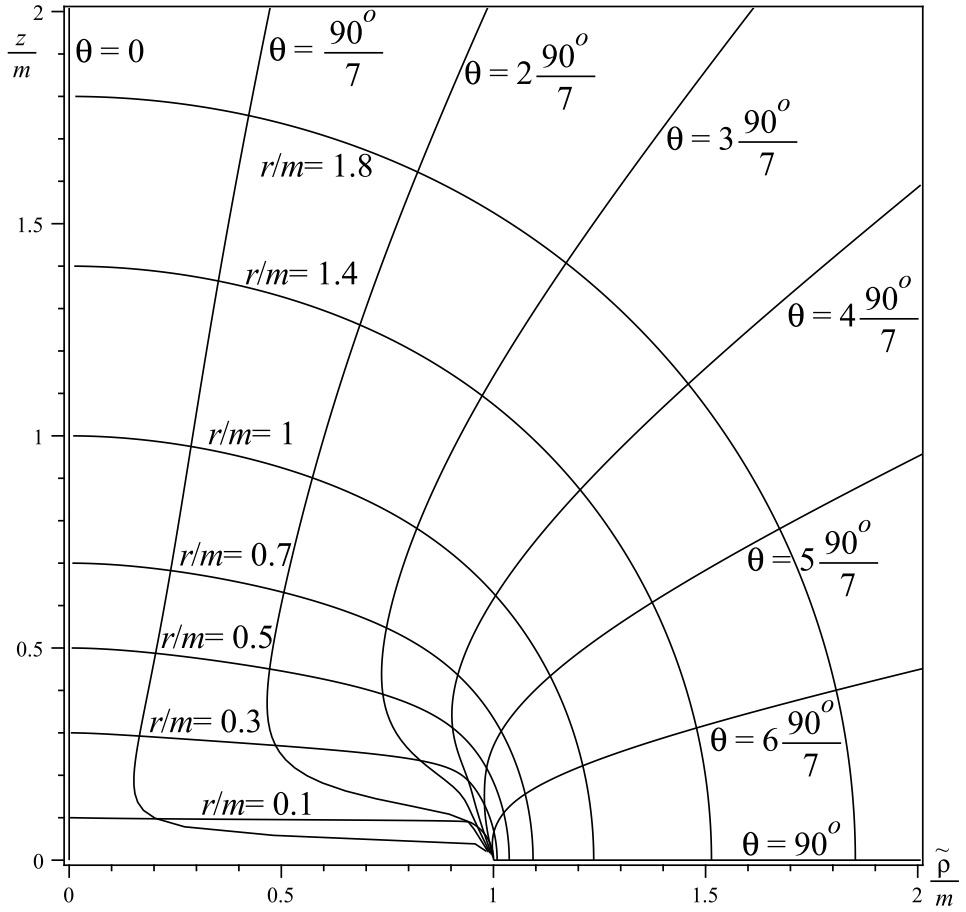

Figure 2.5: The $z/m - \tilde{\rho}/m$ quarter plane. These are *not* oblate spheroidal coordinates. The "edge" $0 < \tilde{\rho} < m$, where $r = 0$, is not part of the spacetime.

$\theta = 0$ and $\theta = \pi$ reach $\tilde{\rho} = 0$, all other trajectories of constant θ reach $\tilde{\rho} = m$. This is shown in figure 2.5.

The gradient fields of the CC metric are shown in Figures 2.6 and 2.7 with this new unfolding. It is very important to realize that this unfolding cannot correct all misrepresentations created by the Weyl coordinates. In particular, if the Weyl coordinates do not cover the "edge", neither does the unfolding.

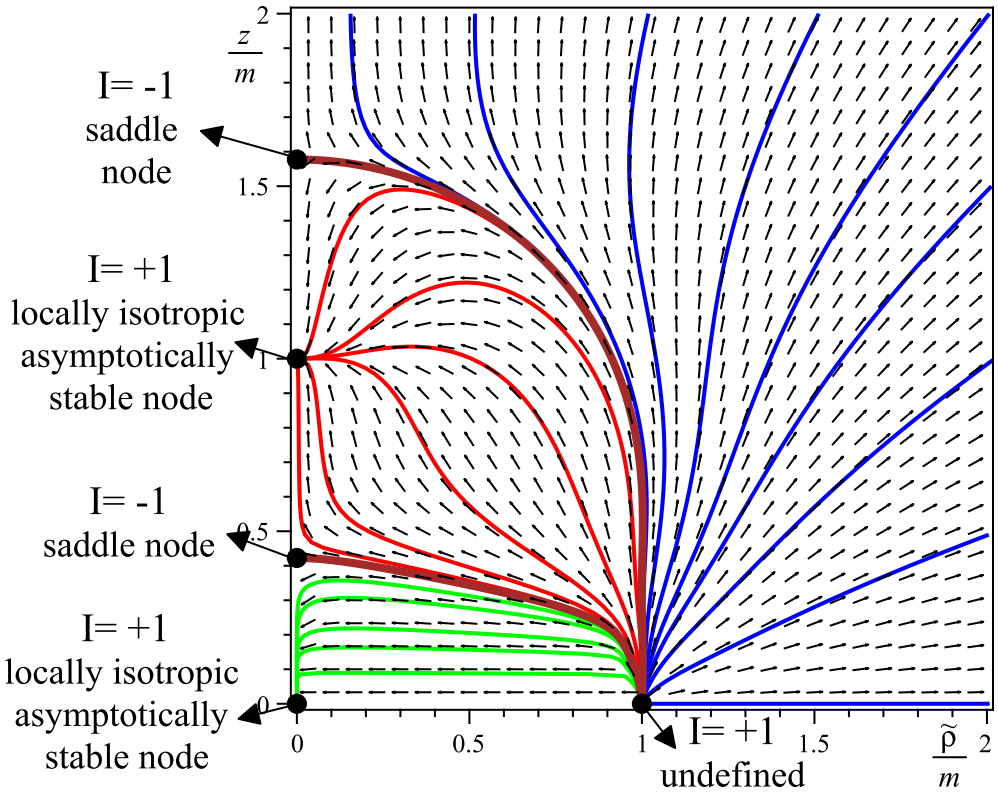

Figure 2.6: As in Figure 2.1 but with the new unfolding.

2.4.5 Mass

Whereas the constant m has entered the CC solution via the Newtonian potential (2.4), the meaning of m within the CC solution is no longer obvious. This is explored in Appendix D where we show that m is certainly the "mass" at spatial infinity. However, away from spatial infinity, looking at quasi local and local constructions, we find that the Hawking mass $\mathcal{M}_H$ provides no useful information for the CC solution for small r. Rather, it is the classical effective gravitational mass $\mathcal{M} \equiv \mathcal{R}_{\theta\ \phi}^{\ \theta\ \phi} g_{\theta\theta}^{\ 3/2}/2$ [1] that provides useful information on the CC solution. Whereas this $\mathcal{M}$ rapidly converges to m with increasing r, near $r = 0$, $\mathcal{M}$ shows considerable structure. Most interesting is the fact that $\mathcal{M} = 0$ at the (naked) singularity, reminiscent of spherically

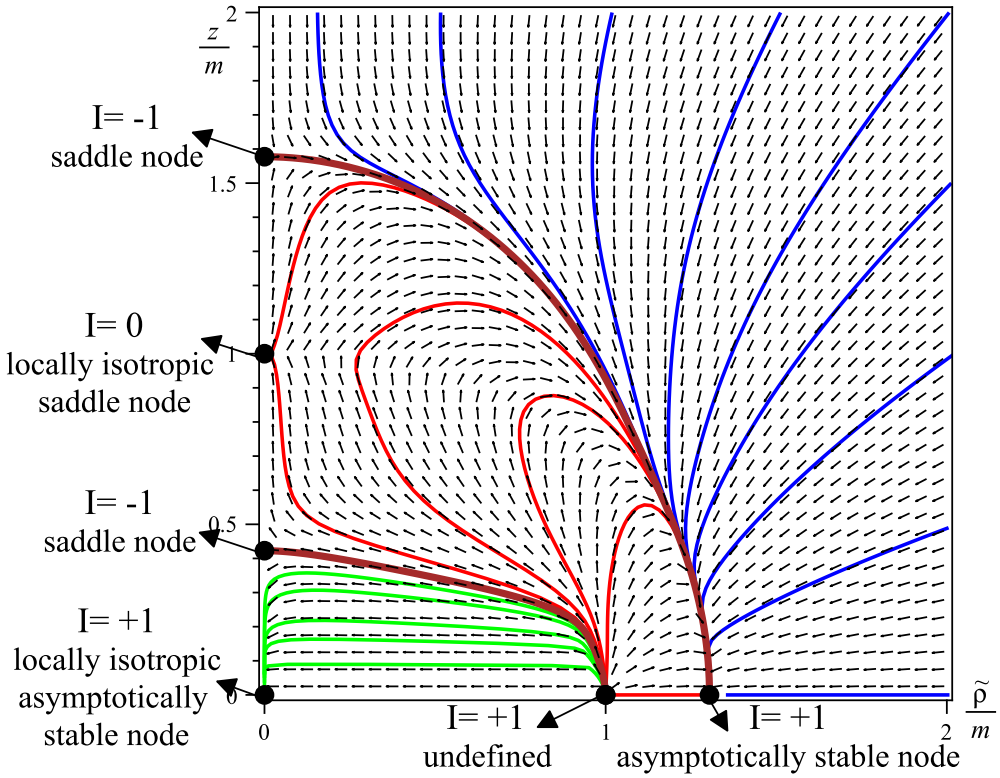

Figure 2.7: As in Figure 2.2 but with the new unfolding.

symmetric naked singularities [18].

2.5 The Newtonian analogue

2.5.1 Construction

As explained previously [1], we construct the Newtonian tidal tensor

$$E_{ab} = \Phi_{,a,b} - \frac{1}{3}\eta_{ab}\Box\,\Phi, \tag{2.23}$$

and define the associated invariant

$$\mathcal{I}_1 = E_{ab}E^{ab} = \Phi_{,a,b}\Phi^{,a,b} - \frac{1}{3}(\Box\,\Phi)^2. \tag{2.24}$$

We now construct the gradient field

$$l_{1\,c} \equiv -\nabla_c(E_{ab}E^{ab}). \tag{2.25}$$

We say that l_1 is a Newtonian analogue (in no way any limit) of k_1 if their associated phase portraits are "analogous", a designation which is explained quantitatively in detail below. This analogy is strict since, as explained in [1], $k_{1\,\alpha} = -\nabla_\alpha(E_{\beta\gamma}E^{\beta\gamma})$ where $E_{\beta\gamma}$ is the usual electric component of the Weyl tensor; that is, the general - relativistic tidal tensor in the Ricci - flat case. The generalization of (2.25) for comparison with k_2 is

$$l_{2\,d} \equiv -\nabla_d(E^b_a E^c_b E^a_c), \tag{2.26}$$

but, we caution, the physical meaning of the associated scalar is not known.

The Newtonian potential for an infinitely thin ring in vacuum with radius a and mass m is

$$\Phi_{ring}(\rho, z) = -\frac{\tilde{m}}{2\pi}\int_0^{2\pi} \frac{d\theta}{\sqrt{\tilde{\rho}^2 + \tilde{z}^2 + 1 - 2\tilde{\rho}\cos\theta}}, \tag{2.27}$$

where $\tilde{x} \equiv x/a \quad \forall\ x$. Note that m only affects the intensity of the gradient field, but does not change the shape of the flow lines or the normalized field when the coordinates are parameterized by the radius a. We now drop $\tilde{}$ and take $m = 1$.

Even though we are in Newtonian vacuum ($\Box\,\Phi = 0$), the formulae off $\rho = 0$ are too large to give here (we give the general formulae in Appendix E). Along $\rho = 0$ we find

$$l_{1\,a} = \frac{7z(2z^2-1)(2z^2-3)}{(z^2+1)^6}\delta^z_a, \tag{2.28}$$

and so we have critical points at $z = 0, \pm 1/\sqrt{2}$ and $\pm\sqrt{3/2}$. The non -zero components of the Hessian are given by

$$H_{\rho\rho} = \frac{-28z^6 + 116z^4 - 39z^2 + 12}{(z^2+1)^7} \tag{2.29}$$

and

$$H_{zz} = \frac{7(28z^6 - 92z^4 + 57z^2 - 3)}{(z^2+1)^7} \tag{2.30}$$

so that the determinant is given by $H = H_{\rho\rho}H_{zz}$. Finally, again along $\rho = 0$, we find

$$\mathcal{I}_1 = \frac{7(2z^2-1)^2}{6(z^2+1)^5}. \tag{2.31}$$

Since E_{ab} vanishes at the critical points $z = \pm 1/\sqrt{2}$, and borrowing the notation from the relativistic case, we call these critical points "isotropic". Otherwise the critical points are classified in the usual way. The Newtonian gradient field, obtained numerically, is shown in Figure 2.8. The overall index is +1. Following an analogous procedure for l_2 we obtain Figure 2.9. Again the overall index is +1.

2.5.2 Comparison

Now in comparing Figures 2.6 and 2.8 we need to be quantitative, not just qualitative. It is important to recall that the existence of a critical point is coordinate independent (up to the use of defective coordinates) as is the classification of critical points. We say that two flows are analogous, within respective regions, if the flows give the same number and type and order of critical points and, therefore, the same Euler characteristic for the regions. Once again, this comparison is coordinate independent. Comparing Figures 2.6 and 2.8 we see that the flow in the CC metric, excluding the inner (green) region, is analogous to the flow associated with a Newtonian ring. An unfolding of the CC metric at $(\rho, z) = (0, 0)$ is central to this comparison. The fact

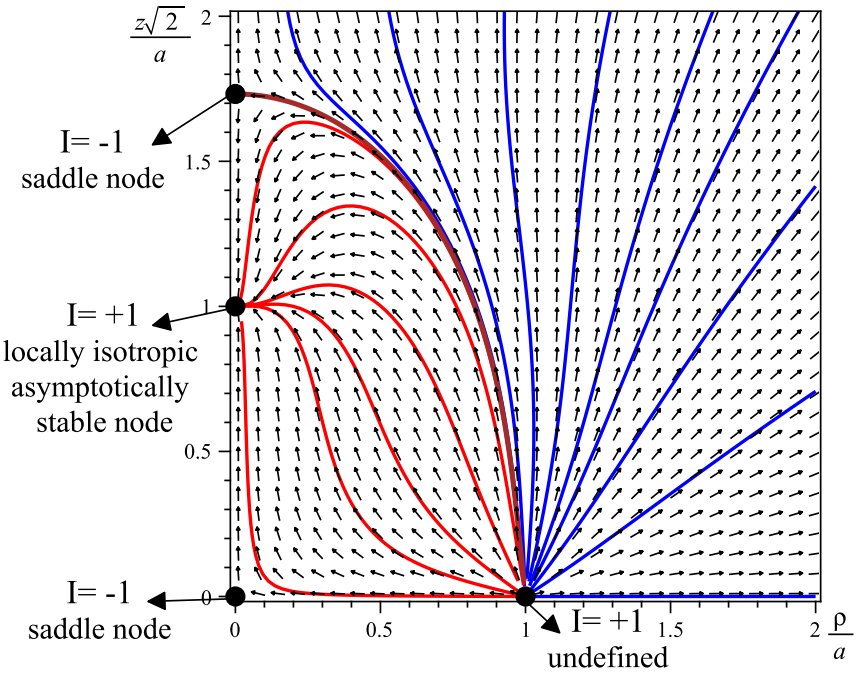

Figure 2.8: Gradient field $l_{1\,a}$, defined by (2.25), for a Newtonian ring in vacuum. We have used $\sqrt{2}z$ for visualization purposes only. Compare Figure 2.6.

that the CC solution contains an additional flow (the inner (green) flow) not present for a Newtonian ring is a fact we simply have to accept. We must also accept the fact that the CC solution itself is incompletely understood in this region.

Comparing Figures 2.7 and 2.9 we see that as well as the additional inner flow (green) in the CC metric, there is also an additional critical point in the equatorial plane not present for a Newtonian ring. Otherwise, as is evident, the gradient flows are remarkably similar. Since the physics of (2.26) has not been established, we content ourselves with a comparison of Figures 2.6 and 2.8.

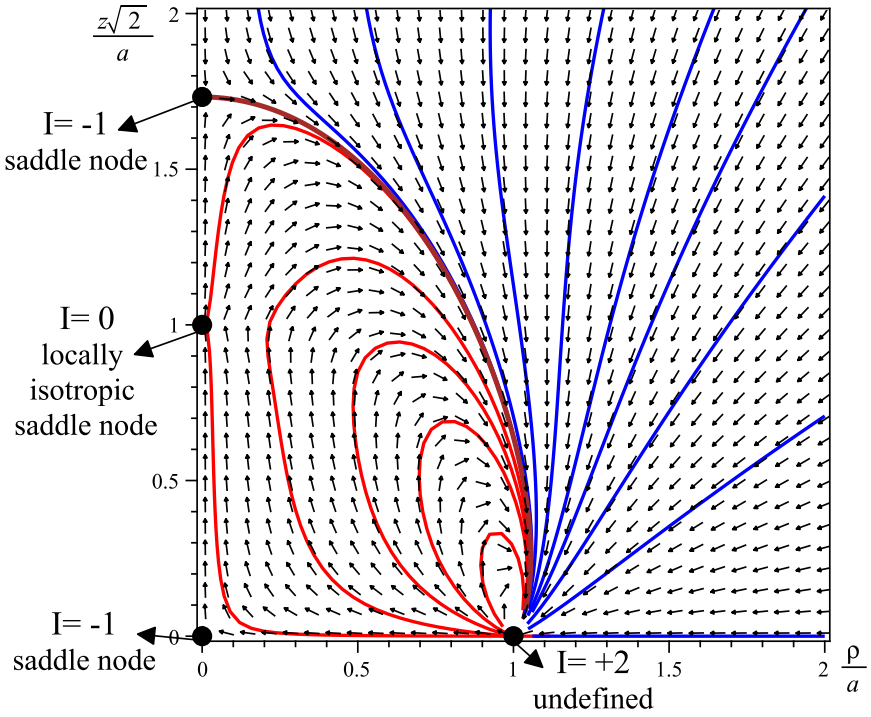

Figure 2.9: Gradient field $l_{2\,a}$, defined by (2.26), for a Newtonian ring in vacuum. Compare Figure 2.7.

2.6 Discussion and Conclusion

We have demonstrated a new tool designed to visualize spacetime curvature based on the construction of gradient flows of invariants. The emphasis here has been on the construction of strict Newtonian analogues wherein the invariants are the relativistic and Newtonian tidal invariants. The case we have considered, the Curzon - Chazy solution, is by no means an easy case to start out with. Despite this, we have shown that the gradient flows for the tidal invariant in the Curzon - Chazy solution, and that for an infinitely thin Newtonian ring, are, in a quantitative sense, remarkably similar in detail. This quantitative comparison of regions involves the number, type and order of critical points (and so the associated Euler characteristic). This comparison

is coordinate independent. Only "interior to" and "close to" the Curzon - Chazy "ring" (within the framework of a new unfolding of the Curzon - Chazy solution) do the flows differ. This region is absent in the Newtonian case. For completeness we have included all non - differential invariants of the Curzon - Chazy solution and so we have also included a study of the second Weyl invariant and its Newtonian counterpart for an infinitely thin ring. Again we find that the gradient flows are remarkably similar in detail except for the same region close to the Curzon - Chazy ring and the addition of an external, but "close", critical "ring" of the flow in the equatorial plane not present for the Newtonian ring. The arguments presented here, we believe, go a long way to clarify the notion that the "source" of the Curzon - Chazy solution is "ring - like" and that the construction of strict Newtonian analogues, correct "in the large", is possible.

2.7 Appendix

2.7.1 Stachel Coordinates

Under the transformations

$$\rho = r\sin(\theta), \quad z = r\cos(\theta) \tag{2.32}$$

the CC metric takes the form

$$ds^2 = -e^{-\frac{2m}{r}}dt^2 + e^{\frac{2m}{r}}(e^{-\frac{m^2\sin(\theta)^2}{r^2}}(dr^2 + r^2d\theta^2) + r^2\sin(\theta)^2d\phi^2). \tag{2.33}$$

Either from (2.33), or from CC metric and (2.32), we obtain

$$w1 \equiv (w1R)m^4 = 2e^{2t1}\frac{(3t2 + \sin(\theta)^2t3)}{x^{10}} \tag{2.34}$$

and

$$w2 \equiv (w2R)m^6 = -3e^{3t1}\frac{(x-1)(2t2+\sin(\theta)^2 t3)}{x^{14}} \tag{2.35}$$

where

$$x \equiv r/m, \tag{2.36}$$

$$t1 \equiv \frac{\sin(\theta)^2 - 2x}{x^2}, \tag{2.37}$$

$$t2 \equiv x^2(x-1)^2, \tag{2.38}$$

and

$$t3 \equiv 3x^2 - 3x + 1. \tag{2.39}$$

Now let us take

$$\sin(\theta) \equiv a(x), \tag{2.40}$$

where $0 \leq a \leq 1$, in order to define trajectories $\theta(x)$. We are interested in limits as $x \to 0$. First let us assume $a \in C^2$.

i) $a(0) = a_o \neq 0$

We find

$$w1 \sim 2e^{2\frac{a_o^2}{x^2}}\frac{a_o^2}{x^{10}} \to \infty, \tag{2.41}$$

and

$$w2 \sim -3e^{3\frac{a_o^2}{x^2}}\frac{a_o^2}{x^{14}} \to -\infty. \tag{2.42}$$

ii) $a(0) = 0$

We find

$$w1 \sim \frac{6}{e^{\frac{4}{x}} x^8} \to 0, \tag{2.43}$$

and

$$w2 \sim -\frac{6}{e^{\frac{6}{x}} x^{12}} \to 0. \tag{2.44}$$

Historically, $a \in C^0$ have played a role. Following [8], in the notation of [10], consider the trajectories

$$\frac{z}{m} = b(\frac{1}{2})^{\frac{1}{3}}(\frac{\rho}{m})^n, \quad (b, n > 0), \tag{2.45}$$

that is,

$$x\cos(\theta) = b(\frac{1}{2})^{\frac{1}{3}}(x\sin(\theta))^n. \tag{2.46}$$

Now if $a(0) = 0$, we can use the small angle formula to obtain

$$a = \frac{x^{\frac{1-n}{n}}}{B^{\frac{1}{n}}}, \quad B \equiv b(\frac{1}{2})^{\frac{1}{3}}. \tag{2.47}$$

Of particular interest is the case $n = 2/3$ for which

$$a = \left(\frac{2x}{b^3}\right)^{\frac{1}{2}}. \tag{2.48}$$

For the convergence of $w1$ and $w2$ we must have

$$\frac{a^2 - 2x}{x^2} < 0, \tag{2.49}$$

that is, $b > 1$ for the case (2.48). This is the correction in [10] to an error in [8]. Further details concerning the very particular choice (2.45) can be found in [10]. Here we simply note that $a \in C^1$ requires $n < 1/2$ and $a \in C^2$ requires $n < 1/3$ for this particular choice. In [10], Scott and Szekeres go on to argue (on page 562) that they found a trajectory along which $w1R$ goes to a finite non - zero constant as $r \to 0$. We have examined this claim in detail and find the claim to be false. Along

the suggested trajectory we find that the scalar $w1$ goes to zero.[9] Our understanding is that only two limits are possible within known coordinates: zero and $\pm$ infinity.

Now for the metric (2.33), $\xi^\alpha = \delta^\alpha_t$ is a Killing vector. As a result, for all geodesics with tangents u^α we have a constant of the motion $\xi^\alpha u_\alpha \equiv -\gamma$. As a result, for all geodesics we have

$$\frac{dt}{d\lambda} = \pm\gamma e^{\frac{2}{x}} \tag{2.50}$$

where λ is an affine parameter. This shows the inadequacy of the coordinate t as $x \to 0$.

2.7.2 Gradient Fields in Stachel Coordinates

The gradient flow associated with the invariant $w1r$ is given by

$$m^5 k_{1\,r} = 2e^{2t1}\frac{\sin(\theta)^2(4\sin(\theta)^2 t3 + t4) + 6t5}{x^{13}} \tag{2.51}$$

and

$$m^6 k_{1\,\theta} = -4e^{2t1}\frac{\sin(\theta)\cos(\theta)(2\sin(\theta)^2 t3 + t6)}{x^{14}} \tag{2.52}$$

where

$$t4 \equiv x(36x^3 - 63x^2 + 34x - 4), \tag{2.53}$$

$$t5 \equiv x^3(3x^2 - 6x + 2)(x - 1), \tag{2.54}$$

and

$$t6 \equiv x^2(9x^2 - 15x + 7). \tag{2.55}$$

The gradient flow associated with the invariant $w2r$ is given by

[9] This is rather unfortunate in the sense that had the claim been correct, a further unfolding of the singularity would be absolutely necessary for a complete understanding of the singularity.

$$m^7 k_{2\,r} = -3e^{3t1}\frac{6(x-1)t5 + \sin(\theta)^2(6\sin(\theta)^2(x-1)t3 + xt7)}{x^{17}} \tag{2.56}$$

where

$$t7 \equiv 45x^4 - 126x^3 + 124x^2 - 50x + 6, \tag{2.57}$$

and

$$m^8 k_{2\,\theta} = 6e^{3t1}\frac{\sin(\theta)\cos(\theta)(x-1)(3\sin(\theta)^2 t3 + t6)}{x^{18}}. \tag{2.58}$$

2.7.3 Scott - Szekeres Unfolding

The unfolding of $(\rho, z) = (0, 0)$ given by Scott and Szekeres in [10] and [11], obtained by trial and error, is

$$X = \arctan((\rho/m)\, e^{m/z}) + \arctan((\rho/m)\, e^{(-\sqrt{2}m/\rho)^{2/3}}) \tag{2.59}$$

and

$$Y = \arctan\left(3\frac{z}{m} - \frac{(z/m)^2\, e^{m/r - m^2\rho^2/2r^4})}{((r/m)^8 + 1 + \frac{1}{3}(\rho/m)^2\,(r/m)^{-4})^{1/4}}\right) \tag{2.60}$$

in Weyl coordinates. In Stachel coordinates we find

$$X = \arctan(x\sin(\theta)e^{1/x\cos(\theta)}) + \arctan(x\sin(\theta)e^{(-\sqrt{2}/x\sin(\theta))^{2/3}}) \tag{2.61}$$

and

$$Y = \arctan\left(3x\cos(\theta) - \frac{x^2\cos(\theta)^2 e^{-t1/2}}{(x^8 + 1 + \sin(\theta)^2/3x^2)^{1/4}}\right). \tag{2.62}$$

2.7.4 "mass"

We are interested to see how the constant m in the CC solution is related to "mass". First, let us rewrite (2.33) via Taylor series about $1/r = 0$ with explicit terms to order $1/r$. We have

$$ds^2 = -(1 - \frac{2m}{r})dt^2 + (1 + \frac{2m}{r})(dr^2 + r^2 d\Omega_2^2) \tag{2.63}$$

where $d\Omega_2^2$ is the metric of a unit 2-sphere $(d\theta^2 + \sin^2(\theta)d\phi^2)$. To this order in r we find that the Einstein tensor for (2.63) vanishes. Due to the spherical symmetry of (2.63) we can consider the mass defined by $\mathcal{M} \equiv \mathcal{R}_{\theta\ \phi}^{\ \theta\ \phi} g_{\theta\theta}^{\ 3/2}/2$ [2]. To order $1/r$ we find

$$\frac{\mathcal{M}}{m} = 1 - \frac{3}{2}\left(\frac{1}{x}\right). \tag{2.64}$$

As a result, at spatial infinity, m is the "mass". We need not consider the ADM mass, the Komar integrals nor the Bondi -Sachs mass [15]. Rather, we are interested in exploring the meaning of m away from spatial infinity. We are, therefore, interested in local and quasi-local quantities.

Let us look at the Hawking mass [16], which can be defined by

$$\mathcal{M}_H = \left(\frac{A(\mathcal{S})}{16\pi}\right)^{1/2}\left(1 - \frac{1}{2\pi}\oint_{\mathcal{S}} \rho\mu d\mathcal{S}\right) \tag{2.65}$$

where $\mathcal{S}$ is a spacelike topological two-sphere, $A(\mathcal{S})$ is the associated area and here ρ and μ are the Newman - Penrose spin coefficients. As mentioned above, Stachel [7] showed that for $\mathcal{S}$ defined by surfaces of constant t and r in (2.33), A decreases with decreasing r up to a minimum (which we find to be $r/m \simeq 0.5389$) and then diverges as $r \to 0$. To ensure that $\mathcal{S}$ is a topological two - sphere we use the standard Gauss

- Bonnet theorem

$$\frac{1}{2}\int\int_{\mathcal{S}} \mathcal{R}\sqrt{g}dx^a dx^b = 2\pi\chi(\mathcal{S}) \tag{2.66}$$

where x^a are the coordinates on $\mathcal{S}$, g is the determinant of the metric on $\mathcal{S}$, $\mathcal{R}$ is the Ricci scalar on $\mathcal{S}$, and $\chi(\mathcal{S})$ is the Euler characteristic of $\mathcal{S}$. Again taking $\mathcal{S}$ to be defined by surfaces of constant t and r in (2.33) we find

$$\chi(\mathcal{S}) = 2, \tag{2.67}$$

and so we are indeed considering topological two - spheres. Constructing a complex null tetrad in the usual way, we find that for (2.33)

$$-\rho\mu = -\frac{1}{8}\frac{\exp\left(\frac{m^2\sin(\theta)^2}{r^2}\right)(-2mr+2r^2+m^2\sin(\theta)^2)^2}{e^{(\frac{m}{r})^2}r^6} \tag{2.68}$$

and so we find

$$\begin{aligned}\frac{\mathcal{M}_H}{m} &= -1/32\,\sqrt{2}e^{y}\sqrt{\int_0^{\pi}\frac{\sin(\theta)}{\sqrt{e^{(\sin(\theta))^2y^2}}}d\theta} \\ &\times\left(-8-2\,\sqrt{2}y^2\pi-3/4\,\sqrt{2}y^4\pi+\frac{5}{32}\,\sqrt{2}y^5\pi+7/4\,\sqrt{2}y^3\pi+\sqrt{2}y\pi\right)y^{-1}\end{aligned} \tag{2.69}$$

where $y \equiv m/r = 1/x$. Expanding about $y = 0$ we find that

$$\frac{\mathcal{M}_H}{m} = 1 - \frac{1}{15x^3} - \frac{2}{315x^5} + \mathcal{O}(\frac{1}{x^6}). \tag{2.70}$$

Examining (2.69) in more detail we find that $\mathcal{M}_H = 0$ for $r/m \sim .5742$ and $\mathcal{M}_H \to -\infty$ as $r \to 0$. In this regard, one is reminded of the result of Hansevi [17] who showed that the Hawking mass can be negative even for convex two - surfaces in Minkowski spacetime. We have to conclude that $\mathcal{M}_H$ is not a good measure of "mass" for the CC solution except for large r (in fact $\mathcal{M}_H$ converges very rapidly to m, for example, $\mathcal{M}_H/m \simeq .9914$ at $x = 2$).

Returning to $\mathcal{M} \equiv \mathcal{R}_{\theta\,\phi}{}^{\theta\,\phi} g_{\theta\theta}{}^{3/2}/2$, whereas this quantity is usually restricted to

strict spherical symmetry, it is well defined for (2.33). Indeed, a straightforward calculation gives

$$\frac{\mathcal{M}}{m} = e^{-\frac{t1}{2}}\left(1+\frac{t1}{2}\right), \tag{2.71}$$

where $t1$ is given by (2.37). Continuing with (2.40) we find

$$\lim_{x\to 0}\left(\frac{\mathcal{M}}{m}\right) \to 0, \tag{2.72}$$

for $a(0) = a_o \neq 0$ and

$$\lim_{x\to 0}\left(\frac{\mathcal{M}}{m}\right) \to -\infty, \tag{2.73}$$

for $a(0) = a_o = 0$. In strict spherical symmetry, it is known that naked singularities are massless ($\mathcal{M} = 0$) [18]. The result (2.72) suggests that this might hold away from spherical symmetry. It should be noted that $\frac{\mathcal{M}}{m}$ converges very rapidly to 1 for all θ with increasing x. We conclude that $\mathcal{M}$, if not the "mass", at least summarizes some important properties of the CC solution.

2.7.5 Newtonian $\mathcal{I}_1$ for vacuum

In Newtonian vacuum we have $\Box\,\Phi(\rho,z) = 0$. The components of E_{ab} are obvious. For $\mathcal{I}_1$ we find

$$\mathcal{I}_1 = \frac{(\frac{\partial^2}{\partial\rho^2}\Phi)^2\rho^2 + 2\,(\frac{\partial^2}{\partial\rho\partial z}\Phi)^2\rho^2 + (\frac{\partial^2}{\partial z^2}\Phi)^2\rho^2 + (\frac{\partial}{\partial\rho}\Phi)^2}{\rho^2}. \tag{2.74}$$

The components of $l_{1\,a}$ are

$$l_{1\,\rho} = -\frac{2}{\rho^3}\,((\frac{\partial^2}{\partial\rho^2}\Phi)\rho^3\frac{\partial^3}{\partial\rho^3}\Phi + 2\,(\frac{\partial^2}{\partial\rho\partial z}\Phi)\rho^3\frac{\partial^3}{\partial\rho^2\partial z}\Phi + (\frac{\partial^2}{\partial z^2}\Phi)\rho^3\frac{\partial^3}{\partial z\partial\rho\partial z}\Phi + \rho\,(\frac{\partial}{\partial\rho}\Phi)\frac{\partial^2}{\partial\rho^2}\Phi - (\frac{\partial}{\partial\rho}\Phi)^2), \tag{2.75}$$

and

$$l_{1\,z} = -\frac{2}{\rho^2}\,((\frac{\partial^2}{\partial\rho^2}\Phi)\rho^2\frac{\partial^3}{\partial\rho^2\partial z}\Phi + 2\,(\frac{\partial^2}{\partial\rho\partial z}\Phi)\rho^2\frac{\partial^3}{\partial z\partial\rho\partial z}\Phi + (\frac{\partial^2}{\partial z^2}\Phi)\rho^2\frac{\partial^3}{\partial z^3}\Phi + (\frac{\partial}{\partial\rho}\Phi)\frac{\partial^2}{\partial\rho\partial z}\Phi). \tag{2.76}$$

The components of the Hessian are

$$\begin{aligned} H_{\rho\rho} = \frac{2}{\rho^4}(\,&(\frac{\partial^3}{\partial\rho^3}\Phi)^2\rho^4 + (\frac{\partial^2}{\partial\rho^2}\Phi)\rho^4\frac{\partial^4}{\partial\rho^4}\Phi + 2\,(\frac{\partial^3}{\partial\rho^2\partial z}\Phi)^2\rho^4 + 2\,(\frac{\partial^2}{\partial\rho\partial z}\Phi)\rho^4\frac{\partial^4}{\partial\rho^3\partial z}\Phi + (\frac{\partial^3}{\partial z\partial\rho\partial z}\Phi)^2\rho^4 + \\ &(\frac{\partial^2}{\partial z^2}\Phi)\rho^4\frac{\partial^4}{\partial z\partial\rho^2\partial z}\Phi - 4\,\rho\,(\frac{\partial}{\partial\rho}\Phi)\frac{\partial^2}{\partial\rho^2}\Phi + (\frac{\partial^2}{\partial\rho^2}\Phi)^2\rho^2 + \rho^2(\frac{\partial}{\partial\rho}\Phi)\frac{\partial^3}{\partial\rho^3}\Phi + 3\,(\frac{\partial}{\partial\rho}\Phi)^2), \end{aligned} \tag{2.77}$$

$$\begin{aligned} H_{\rho z} = \frac{2}{\rho^3}(\,&(\frac{\partial^3}{\partial\rho^2\partial z}\Phi)\rho^3\frac{\partial^3}{\partial\rho^3}\Phi + (\frac{\partial^2}{\partial\rho^2}\Phi)\rho^3\frac{\partial^4}{\partial\rho^3\partial z}\Phi + 2\,(\frac{\partial^3}{\partial z\partial\rho\partial z}\Phi)\rho^3\frac{\partial^3}{\partial\rho^2\partial z}\Phi + 2\,(\frac{\partial^2}{\partial\rho\partial z}\Phi)\rho^3\frac{\partial^4}{\partial z\partial\rho^2\partial z}\Phi + \\ &(\frac{\partial^3}{\partial z^3}\Phi)\rho^3\frac{\partial^3}{\partial z\partial\rho\partial z}\Phi + (\frac{\partial^2}{\partial z^2}\Phi)\rho^3\frac{\partial^4}{\partial z^2\partial\rho\partial z}\Phi + \rho\,(\frac{\partial^2}{\partial\rho\partial z}\Phi)\frac{\partial^2}{\partial\rho^2}\Phi + \rho\,(\frac{\partial}{\partial\rho}\Phi)\frac{\partial^3}{\partial\rho^2\partial z}\Phi - 2\,(\frac{\partial}{\partial\rho}\Phi)\frac{\partial^2}{\partial\rho\partial z}\Phi), \end{aligned} \tag{2.78}$$

$$H_{zz} = \frac{2}{\rho^2}((\frac{\partial^3}{\partial\rho^2\partial z}\Phi)^2\rho^2 + (\frac{\partial^2}{\partial\rho^2}\Phi)\rho^2\frac{\partial^4}{\partial z\partial\rho^2\partial z}\Phi + 2(\frac{\partial^3}{\partial z\partial\rho\partial z}\Phi)^2\rho^2 + 2(\frac{\partial^2}{\partial\rho\partial z}\Phi)\rho^2\frac{\partial^4}{\partial z^2\partial\rho\partial z}\Phi + (\frac{\partial^3}{\partial z^3}\Phi)^2\rho^2 + (\frac{\partial^2}{\partial z^2}\Phi)\rho^2\frac{\partial^4}{\partial z^4}\Phi + (\frac{\partial^2}{\partial\rho\partial z}\Phi)^2 + (\frac{\partial}{\partial\rho}\Phi)\frac{\partial^3}{\partial z\partial\rho\partial z}\Phi) \tag{2.79}$$

and

$$H_{\theta\theta} = 2\,\frac{(\frac{\partial^2}{\partial\rho^2}\Phi)\rho^3\frac{\partial^3}{\partial\rho^3}\Phi + 2(\frac{\partial^2}{\partial\rho\partial z}\Phi)\rho^3\frac{\partial^3}{\partial\rho^2\partial z}\Phi + (\frac{\partial^2}{\partial z^2}\Phi)\rho^3\frac{\partial^3}{\partial z\partial\rho\partial z}\Phi + \rho(\frac{\partial}{\partial\rho}\Phi)\frac{\partial^2}{\partial\rho^2}\Phi - \frac{\partial}{\partial\rho}\Phi)^2}{\rho^2}. \tag{2.80}$$

acknowledgments

This work was supported in part by a Duncan and Urlla Carmichael Graduate Fellowship (to MA) and a grant (to KL) from the Natural Sciences and Engineering Research Council of Canada. Portions of this work were made possible by use of *GRTensorII* [19].

2.8 References

[1] K. Lake, "Visualizing Spacetime Curvature via Gradient Flows I: Introduction", Phys. Rev. D (in press) (arXiv:1207.5493).

[2] H. Weyl, Annalen der Physik **10**, 185 (1919).

[3] H. E. J. Curzon, Proc. London Math. Soc. **23**, 477 (1925).

[4] J. Chazy, Bull. Soc. Math. France **52**, 17 (1924).

[5] J. Griffiths and J. Podolský, *Exact Space-Times in Einstein's General Relativity* (Cambridge University Press, Cambridge, 2009).

[6] R. Gautreau and J. L. Anderson, Physics Letters A **25**, 291 (1967).

[7] J. Stachel, Physics Letters A **27**, 60 (1968).

[8] F. I. Cooperstock and G. J. Junevicus, Int. J. Th. Phys. **9**, 59 (1974).

[9] P. Szekeres and F. H. Morgan, Commun. Math. Phys. **4**, 313 (1973).

[10] S. M. Scott and P. Szekeres, G. R. G. **18**, 557 (1986).

[11] S. M. Scott and P. Szekeres, G. R. G. **18**, 571 (1986).

[12] F. de Felice, G. R. G. **23**, 135 (1991).

[13] R. Arianrhod, S. Fletcher and C. B. G. McIntosh, Class. Quan. Grav. **8**, 1519 (1991).

[14] J. P. W. Taylor, Class. Quantum Grav. **22**, 4961 (2005).

[15] E. Poisson, *A Relativist's Toolkit The Mathematics of Black-Hole Mechanics* (Cambridge University Press, Cambridge, 2004).

[16] See, for example, L. B. Szabados, Living Rev. Relativity, **12**, (2009), `http://www.livingreviews.org/lrr-2009-4`

[17] Daniel Hansevi, *The Hawking mass for ellipsoidal 2-surfaces in Minkowski and Schwarzschild spacetimes*, thesis Linköpings Universitet, downloaded from `http://www.mai.liu.se/ gober/theses.html`

[18] K. Lake, Phys. Rev. Lett. **68**, 3129 (1992).

[19] This package runs within Maple. The GRTensorII software and documentation is distributed freely from the address *http://grtensor.org*

Chapter 3

Paper II: The Kerr Metric and Rotating Black Holes

Paper Title[1]: "Visualizing Spacetime Curvature via Gradient Flows III: The Kerr Metric and the Transitional Values of the Spin Parameter"

[1]This chapter contains a version of a paper published in Physical Review D as: Majd Abdelqader and Kayll Lake, Physical Review D **88**, 064042 (2013).

3.1 Abstract

The Kerr metric is one of the most important solutions to Einstein's field equations, describing the gravitational field outside a rotating black hole. We thoroughly analyze the curvature scalar invariants to study the Kerr spacetime by examining and visualizing their covariant gradient fields. We discover that the part of the Kerr geometry outside the black hole horizon changes qualitatively depending on the spin parameter, a fact previously unknown. The number of observable critical points of the curvature invariants' gradient fields along the axis of rotation changes at several transitional values of the spin parameter. These transitional values are a fundamental property of the Kerr metric. They are physically important since in general relativity these curvature invariants represent the cumulative tidal and frame-dragging effects of rotating black holes in an observer-independent way.

3.2 Introduction

The discovery of the Kerr metric in 1963 was a milestone in mathematical relativity and astrophysics. It is a vacuum solution to Einstein's field equations that describes the gravitational field outside a massive axisymmetric rotating object, and no interior solution has been found so far. This solution established that general relativity predicts the existence of the objects we now call black holes, even with angular momentum and away from perfect spherical symmetry. The Kerr metric provides the foundation and framework to study and understand many aspects of modern astrophysics, ranging from supermassive black holes at the center of most galaxies, to supernova explosions and gamma ray bursts. For a thorough review of the Kerr

metric and its impact and applications to modern astrophysics, see Ref. [1]. In Boyer-Lindquist coordinates and using natural units ($G = c = 1$), the Kerr metric can be expressed as

$$\begin{aligned} ds^2 = &- \left[1 - \frac{2mr}{r^2 + a^2\cos^2\theta}\right] dt^2 - \frac{4mr\,a\,\sin^2\theta}{r^2 + a^2\cos^2\theta}\, dt\, d\phi \\ &+ \left[\frac{r^2 + a^2\cos^2\theta}{r^2 - 2mr + a^2}\right] dr^2 + (r^2 + a^2\cos^2\theta)\, d\theta^2 \\ &+ \left[r^2 + a^2 + \frac{2mr\,a^2\,\sin^2\theta}{r^2 + a^2\cos^2\theta}\right] \sin^2\theta\; d\phi^2, \end{aligned} \tag{3.1}$$

where m is the mass, and $a = J/m$, is the angular moment per unit mass, or spin parameter.

There is no established standard approach to analyze a metric or a spacetime in general relativity. A common tool used to achieve this is by studying the null and time-like geodesics (i.e. the paths photons and free falling test particles follow) produced by the metric. This approach has been applied extensively to the Kerr metric (see Ref. [1] and references within). In this letter we explore the geometry of the Kerr metric using a novel analysis and visualization tool proposed in [2, 3]. Instead of geodesics, we analyze the geodesic deviations (i.e. tidal and frame-dragging effects) produced by the metric through the Weyl curvature tensor. A somewhat similar approach has been proposed [4, 5, 6, 7], where the electric and magnetic components of the Weyl tensor, representing tidal and frame-dragging effects respectively, are visualized via tendex and vortex flowlines. Those flowlines are produced by an observer-projection of the electric and magnetic tensors into 3-D spacial coordinates, then obtaining the eigenvectors of those projections. Our approach has a common starting point, but in contrast, we base the analysis on observer-independent curvature invariants constructed from the Weyl tensor. The results obtained this way are

genuine properties of the underlying geometry, and independent of any observer or coordinate choice. We discover that the cumulative tidal and frame-dragging effects produced by a rotating black hole change qualitatively depending on the dimensionless ratio between its spin parameter and mass, $A \equiv a/m$. There are 7 unique values of A where critical points of the Weyl curvature invariants emerge from the rotating black hole, and become accessible to observers outside its horizon. This is a major difference compared to non-rotating black holes modeled by the Schwarzschild metric (i.e. $A = 0$), where there is only one critical point on the bifurcation 2-sphere, so it is never accessible to an observer outside the horizon, nor can it be produced via gravitational collapse [2].

3.3 Gradient Fields of the Weyl Invariants

As explained in the introductory paper by [2], we limit our analysis to the eight non-differential curvature scalar invariants that have the crucial property of being observer-independent; the four Ricci invariants, and the four Weyl invariants. The Kerr spacetime is Ricci flat, and the four Ricci invariants vanish. The four Weyl invariants for any Petrov type D spacetime, which is the case for the Kerr metric, are algebraically constrained by the complex syzygy $(w1)^3 = 6(w2)^2$, where $w1$ and $w2$ are the complex Weyl invariants, and the four Weyl invariants can be explicitly expressed as $w1R = \Re(w1)$, $w2R = \Re(w2)$, $w1I = \Im(w1)$, and $w2I = \Im(w2)$. Note that in vacuum solutions such as the Kerr metric, $w1R = 1/8R_{abcd}R^{abcd} = 1/8K$, where K is the Kretschmann scalar. However, in order to thoroughly explore the Kerr geometry, it is not sufficient to examine this scalar alone. Furthermore, the syzygy above means that only two of the four invariants are algebraically independent. In

spite of this, we find that it is still necessary to analyze the gradient fields for all of the four invariants, because, surprisingly, the structure revealed by each one of these fields is not constrained by the syzygy.

The simplified formulas in Boyer-Lindquist coordinates for each of the invariants are[2]

$$w1 = \frac{6\,m^2/a^6}{(R - i\cos\theta)^6}$$
$$w2 = \frac{-6\,m^3/a^9}{(R - i\cos\theta)^9} \tag{3.2}$$

where $R \equiv r/a$. The gradient field of an invariant is simply defined as the covariant derivative $k_\mu \equiv -\nabla_\mu I = -\partial I/\partial x^\mu$, where I is the scalar invariant (see Ref. [2]). The figures presented here are in Kerr coordinates, or pseudo-oblate spheroidal coordinates, inspired by the original Kerr coordinates [3], where the singularity is unfolded to a ring of radius a. Fig. 3.1 shows a 3-D visualization of the gradient flow of $w1R$ for the Kerr metric in the original Kerr coordinates. Fig. 3.2 shows the gradient fields of the four invariants, as well as the outer horizon for different values of the dimensionless spin parameter A. The transformation equations from Boyer-Lindquist coordinates to the coordinates used in Fig. 3.2 are

$$x = \sqrt{r^2 + a^2}\,\sin(\theta)\cos(\phi)$$
$$y = \sqrt{r^2 + a^2}\,\sin(\theta)\sin(\phi) \tag{3.3}$$
$$z = r\,\cos(\theta)$$

[2]This compact way of writing the invariants was pointed out to us by Jan Åman [private communication], up to integer factors to make the invariants consistent with the notation in [2].

[3]Although the shape of the plotted flowlines depends on the coordinate choice, the existence of each critical point, the classification of each critical point, and the existence of asymptotic critical directions of the fields between critical points is coordinate-independent (See [2, 3]).

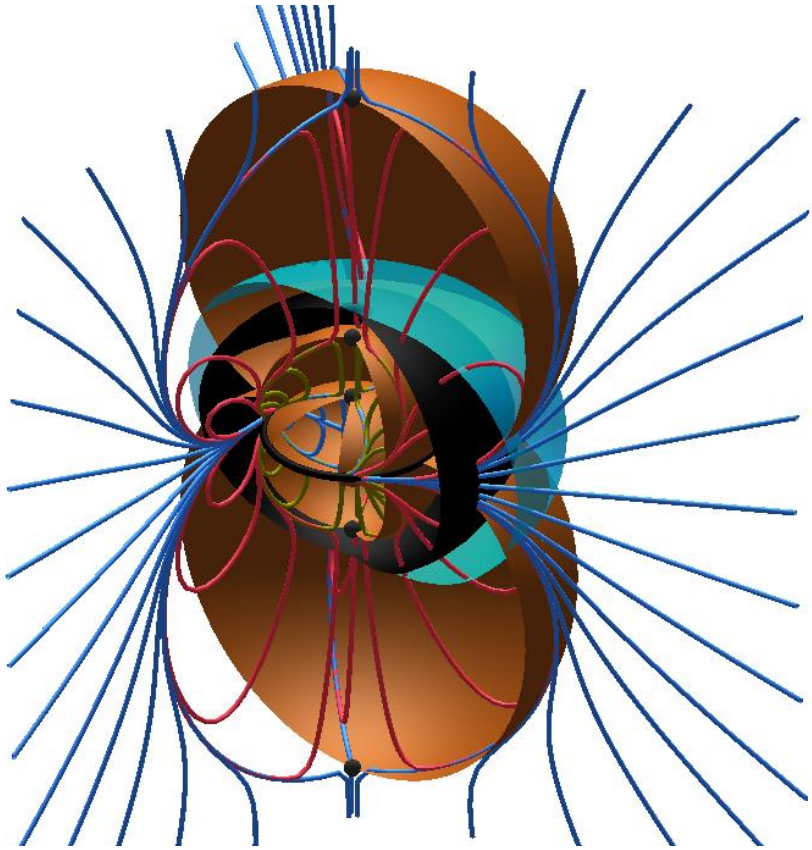

Figure 3.1: 3-D visualization of rotating black holes in Kerr coordinates via flowlines of the vector field $k_\mu \equiv -\nabla_\mu(w1R)$, for a dimensionless spin parameter value of $A = 0.9$. The transparent sky-blue surface is the ergosphere, and the horizon is the black surface. The black circles are the critical points of the gradient field. The colors of the flowlines are of no physical significance, used to distinguish the different regions of the spacetime with common flow structure separated by asymptotic critical directions of the field represented by the brown surfaces, which connect the critical points to the ring singularity.

where the only difference between these coordinates and the original Kerr coordinates is that $[\phi]$ is replaced by $[\phi - \tan^{-1}(a/r)]$ in the equations above for x and y. We choose to omit the $[\tan^{-1}(a/r)]$ term in Fig. 3.2 to keep the gradient fields ϕ-independent and allow us to plot a 2-D slice of the spacetime with constant ϕ. The spacetime in these coordinates is symmetric about the z-axis, and about the $x-y$ plane, therefore it is sufficient to plot one quadrant of the 2-D slice of the spacetime with constant ϕ and t, and in this case we use $\phi = 0$ (i.e. the $z-x$ plane). With the exception of the singularity, all of the critical points of the four gradient fields (i.e. the points where $k_\mu = 0$) lie on the z-axis [4]. There are exactly 7 critical points with $z > a$, more specifically $z_{critical}/a$ = [6.314, 4.381, 3.078, 2.077, 1.963, 1.376, 1.254] and another 7 critical points with $z < a$, where $z_{critical}/a$ =[0.7975, 0.7265, 0.5095, 0.4816, 0.3249, 0.2282, 0.1584]. The 14 values of $z_{critical}$ above are evaluated numerically to 4 significant figures.

3.4 Transitional Values of the Spin Parameter

The event horizons of the Kerr black hole are given by $r_\pm = m \pm \sqrt{m^2 - a^2}$. Therefore, when expressed in the dimensionless form, they simplify to $r_\pm/a = R_\pm = \left(1 \pm \sqrt{1 - A^2}\right)/A$. Note that the horizons still depend on the mass and spin parameter through A in a non-linear way. On the other hand, the locations of the critical points of the gradient fields along the axis of rotation scale linearly with a, as we stated above. Therefore, we find that the observable part of the gradient fields of the Weyl scalar invariants of the Kerr metric (i.e. the structure of curvature outside

[4] For a thorough definition and classification method of these critical points in general, see Ref. [2].

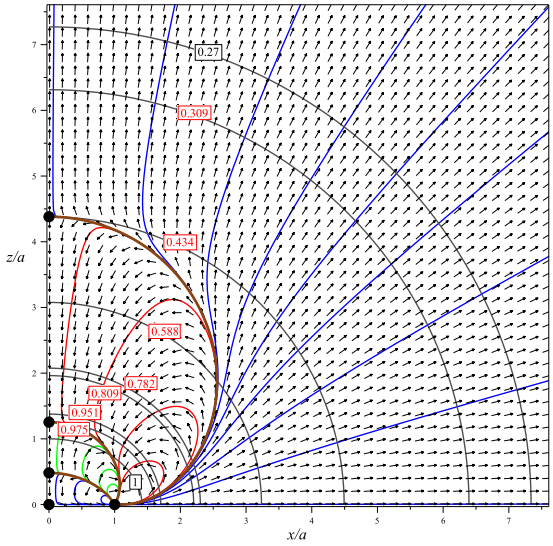

(a) $w1R$

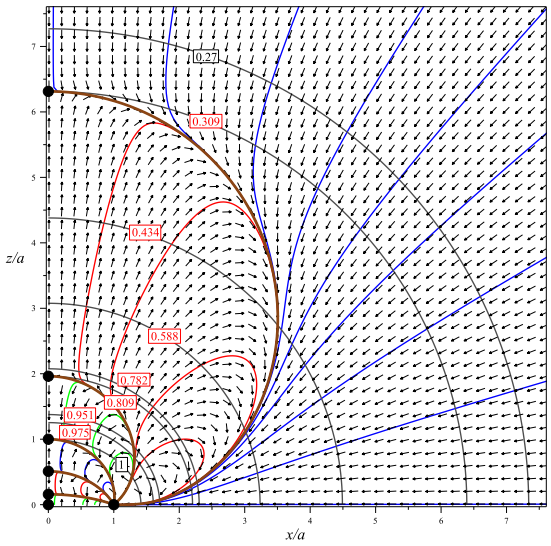

(b) $w2R$

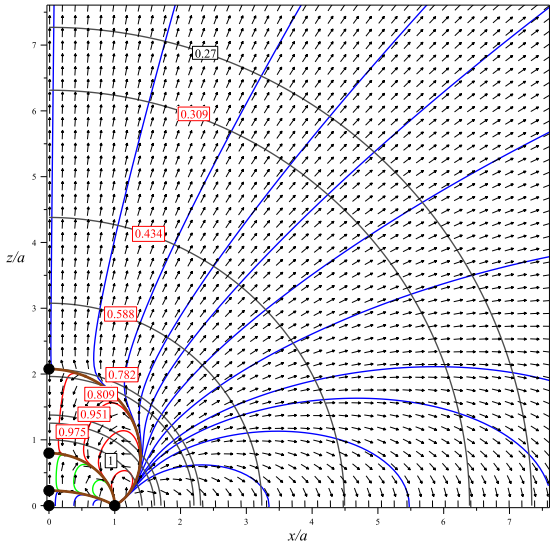

(c) $w1I$

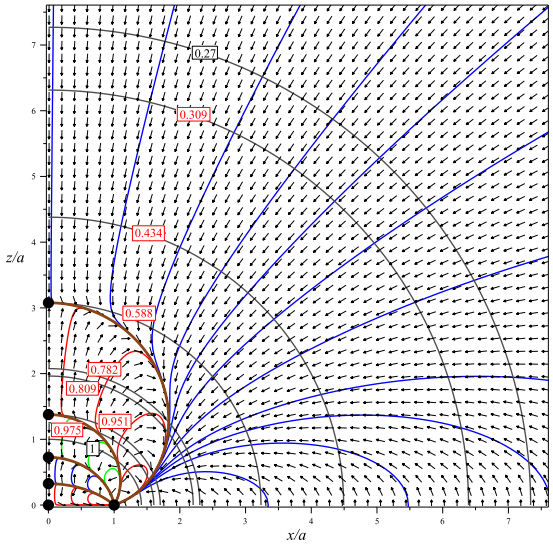

(d) $w2I$

Figure 3.2: (a) 2-D slice of Fig. 3.1 in Kerr-like coordinates introduced in Eq. (3.3). The ergosphere is omitted, and different horizons are plotted in grey, for the corresponding transitional values of A indicated in the small boxes, in addition to $A = 0.27$ which is not a transitional value but is plotted for presentation purposes. (b), (c), and (d) are the same as (a) but for the gradient vector fields of $w2R$, $w1I$, and $w2I$ respectively.

a rotating black hole) changes qualitatively depending the dimensionless spin parameter A. Furthermore, at very specific values of A, the outer horizon crosses one of the critical points of the four gradient fields, making that critical point accessible to an observer outside the black hole. The transitional values of the spin parameter are $A = [0.3090, 0.4339, 0.5878, 0.7818, 0.8090, 0.9511, 0.9749]$, evaluated to 4 significant figures. We also find that the inner horizon also crosses one of the critical points with $z_{critical} < a$ at each one of the transitional values of A stated above. This indicates a deeper connection between the four Weyl invariants and the horizons of the Kerr black hole, even though the algebraic form of the invariants does not seem to include any information about the horizons in Eq. 3.2. Fig. 3.3 summarizes the result, plotting the the outer and inner horizons as a function of A. The transitional values of A mentioned above are indicated on the curves, along with the value of $z_{critical}$ that the horizons cross at each transitional A.

3.5 Conclusion

We have applied a new curvature visualization and analysis tool to the Kerr metric, and have discovered some fundamental properties of the Kerr spacetime. The observable structure of the Kerr geometry outside the horizon of rotating black holes changes qualitatively at 7 specific values of the spin parameter. The invariants under scrutiny represent the cumulative tidal and frame dragging effects that the rotating black hole exerts on the surroundings, as explained in detail in [2, 3, 4, 5, 6, 7]. In other words, if one can send a spaceship with very precise tools to measure tidal and frame dragging forces, it is possible in principle to map the values of these invariants around a rotating black hole. Therefore, the critical points that emerge from the

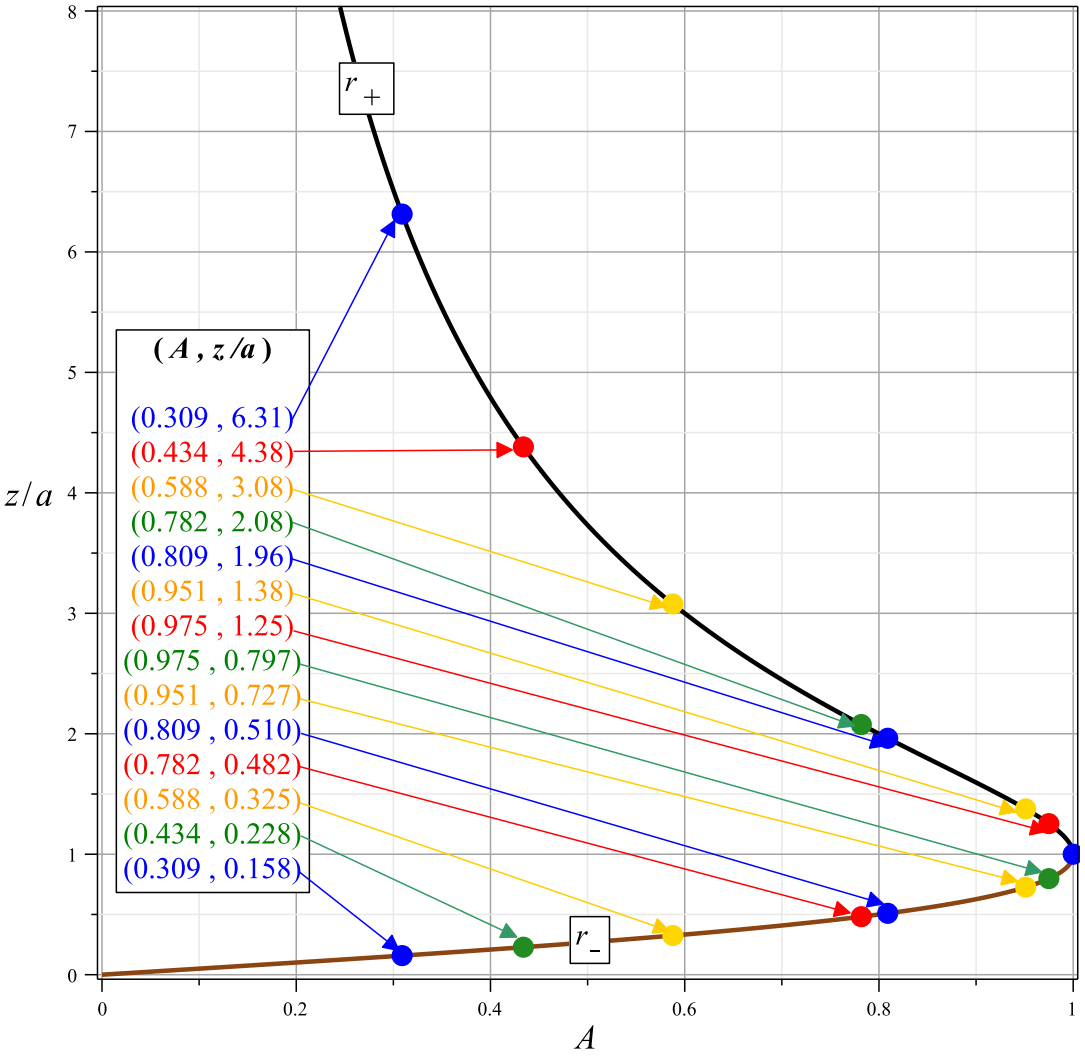

Figure 3.3: The outer horizon r_+ (black) and the inner horizon r_- (brown) of a rotating black hole vs. its dimensionless spin parameter A. The transitional values of A are indicated by the red, blue, green, and yellow points, associated with the horizons crossing one of the critical points of the invariant $w1R$, $w2R$, $w1I$ and $w2I$ respectively.

horizon at each transitional value of the spin parameter are observable in principle. It is interesting to note that the region surrounding the event horizon of Sagittarius A* will soon be visible by way of the Event Horizon Telescope [8, 9].

Another useful application of the technique in this letter would be in the analysis of numerical relativity simulations. The visualization tool presented here provides a coordinate-independent, observer-independent, and physically intuitive picture where the flowlines seek the extremum points of curvature associated with each invariant. Furthermore, proper lengths between the critical points (e.g. the null affine distances or the proper length of a time-like curve between points) would provide a coordinate independent way to extract angular moment and mass estimates of black holes in the simulations.

acknowledgments

The authors would like to thank Robert Owen for helpful discussions. This work was supported in part by a Duncan and Urlla Carmichael Graduate Fellowship (to MA) and a grant (to KL) from the Natural Sciences and Engineering Research Council of Canada. Portions of this work were made possible by use of *GRTensorII* [10].

3.6 References

[1] D. L. Wiltshire, M. Visser, and S. M. Scott, "The Kerr Spacetime: Rotating Black Holes in General Relativity", Cambridge University Press (2009).

[2] K. Lake, "Visualizing Spacetime Curvature via Gradient Flows I: Introduction", Phys. Rev. D, **86**, 10 (2012).

[3] M. Abdelqader, K. Lake, "Visualizing spacetime curvature via gradient flows. II. An example of the construction of a Newtonian analogue", Phys. Rev. D, **86**, 12 (2012).

[4] R. Owen, J. Brink, Y. Chen, J. Kaplan, G. Lovelace, K. Matthews, D. Nichols, M. Scheel, F. Zhang, A. Zimmerman, and K. Thorne, Phys. Rev. Letters, **106**, 15 (2011).

[5] D. A. Nichols, R. Owen, F. Zhang, A. Zimmerman, J. Brink, Y. Chen, J. D. Kaplan, G. Lovelace, K. D. Matthews, M. A. Scheel, and K. S. Thorne, Phys. Rev. D, **84**, 12 (2011).

[6] F. Zhang, A. Zimmerman, D. a. Nichols, Y. Chen, G. Lovelace, K. D. Matthews, R. Owen, and K. S. Thorne, Phys. Rev. D, **86**, 8 (2012).

[7] D. a. Nichols, A. Zimmerman, Y. Chen, G. Lovelace, K. D. Matthews, R. Owen, F. Zhang, and K. S. Thorne, Phys. Rev. D, **86**, 10 (2012).

[8] S. S. Doeleman et al., Nature, **455**, 7209 (2008).

[9] S. S. Doeleman et al., Science, **338**, 6105 (2012).

[10] This package runs within Maple. The GRTensorII software and documentation is distributed freely from the address *http://grtensor.org*

Chapter 4

Paper III: Penrose Diagrams of McVittie

Paper Title[1]: "More on McVittie's Legacy: A Schwarzschild - de Sitter black and white hole embedded in an asymptotically ΛCDM cosmology"

[1]This chapter contains a version of a paper published in Physical Review D as: Kayll Lake and Majd Abdelqader, Physical Review D, **84**, 4, 044045 (2011).

4.1 Abstract

Recently Kaloper, Kleban and Martin reexamined the McVittie solution and argued, contrary to a very widely held belief, that the solution contains a black hole in an expanding universe. Here we corroborate their main conclusion but go on to examine, in some detail, a specific solution that asymptotes to the ΛCDM cosmology. We show that part of the boundary of the solution contains the inner bifurcation two - sphere of the Schwarzschild - de Sitter spacetime and so both the black and white hole horizons together form a partial boundary of this McVittie solution. We go on to show that the null and weak energy conditions are satisfied and that the dominant energy condition is satisfied almost everywhere in the solution. The solution is understood here by way of a systematic construction of a conformal diagram based on detailed numerical integrations of the null geodesic equations. We find that the McVittie solution admits a degenerate limit in which the bifurcation two - sphere disappears. For solutions with zero cosmological constant, we find no evidence for the development of a weak null singularity. Rather, we find that in this case there is either a black hole to the future of an initial singularity or a white hole to its past.

4.2 Introduction

A simple, but painful truth is the fact that it is far easier to find an exact solution to Einstein's equations than it is to understand it. A fine example of this is given by McVittie's inhomogeneous cosmological solution [1], the meaning of which has been debated since 1933. In retrospect, this effort has to be considered an utterly remarkable step into an area of research which is, to this day, still in its infancy [2].

The McVittie solution has been the subject of a large number of investigations (we point to the recent thesis by Martin [3] and the review given in [4]), and generalizations [5], but only recently did Kaloper, Kleban and Martin [6] (henceforth KKM) explain the misinformation which has developed around this solution. In this paper we corroborate the main conclusion in KKM but also penetrate more deeply into an understanding of a specific solution. By way of the specification of a characteristic function for the solution, we exhibit a specific solution that asymptotes to the standard ΛCDM universe. Remarkably, part of the inner boundary of this solution contains the inner bifurcation two - sphere of the non - degenerate Schwarzschild - de Sitter spacetime. This tells us that both the black and white hole horizons of the extended Schwarzschild - de Sitter spacetime form part of the boundary of this McVittie solution, a possibility not envisioned in the KKM analysis. The specification of a characteristic function provides sufficient detail to allow for an examination of energy conditions and a systematic construction of the conformal diagram based on detailed numerical integrations of the null geodesic equations. The present work suggests that the very notion of an inhomogeneity in cosmology may well go beyond the concept of inhomogeneity in elementary physical variables. Finally, a minor point in the KKM analysis was the suggestion that in the case of a zero cosmological constant, the would - be horizon forms a weak null singularity. Here we find no evidence for this behaviour.[2]

[2]Whereas the analysis given here parallels, in some respects, that given in KKM, it also differs in a number of important aspects. We present a full discussion and point out at various stages agreement and disagreement with the KKM analysis.

4.3 The Solution

4.3.1 Overview

The particular solution we are concerned with here is the simplest of the McVittie class,[3] and this can be written in the form (e.g. [8]) [9]

$$ds^2 = -\left(\frac{1-m/2u}{1+m/2u}\right)^2 dt^2 + e^{\beta(t)}(1+m/2u)^4(dr^2+r^2d\Omega_2^2) \tag{4.1}$$

where $u \equiv re^{\beta/2}$, m is a positive constant and $d\Omega_2^2$ is the metric of a unit 2-sphere. Clearly, for $m = 0$ we obtain a spatially flat Robertson - Walker metric, and for constant β, we have the Schwarzschild metric (here in isotropic coordinates). These observations do not constitute an understanding of the metric (4.1). Indeed, it is a trivial exercise to construct distinct spacetimes with these two fundamental features. Perhaps, the enduring interest in the McVittie solution derives from the observation that if we take the coordinates of (4.1) as comoving then we obtain a perfect fluid with energy density ρ and isotropic pressure p given by (e.g. [8])

$$8\pi\rho = \frac{3}{4}\dot{\beta}^2, \;\; 8\pi p = -\frac{3}{4}\dot{\beta}^2 - \frac{\ddot{\beta}}{\sqrt{1-2m/R(t,r)}} \tag{4.2}$$

where $\dot{} \equiv d/dt$ and

$$R \equiv u(1+m/2u)^2. \tag{4.3}$$

The uniform nature of the energy density and non-uniform nature of the pressure is often brought forward as a reason to consider this solution unphysical. However, even in the static Schwarzschild interior solution, such conclusions can be considered hasty [10]. Our purpose here is not to argue, ab initio, for the physicality of the McVittie

[3]Recently, study of the McVittie solution has been denigrated [7] with the view, in part, that this class of solutions is but a simple subset of a larger class of known solutions. The results presented in this paper argue for the contrary view. Even a simple looking metric can, when properly studied, yield a rich geometric structure.

solution, but rather our purpose is to exhibit in detail the rather remarkable, and heretofore unrecognized, geometric structure that this solution presents. We comment on the idealization that the solution represents only once this structure is developed.

Under the coordinate transformation defined by (4.3), the metric (4.1) becomes (e.g. [8])

$$ds^2 = -f(t,R)dt^2 - \frac{2H(t)R}{\sqrt{1-2m/R}}dtdR + \frac{dR^2}{1-2m/R} + R^2 d\Omega_2^2 \tag{4.4}$$

where

$$f \equiv 1 - 2m/R - H^2R^2 \tag{4.5}$$

and H is the Hubble function, given by $H = \dot{\beta}/2 = \dot{a}/a$ where $a(t)$ is the usual scale factor for $m = 0$. The form (4.4) is the basis for much of the analysis in KKM. Here we use the form (4.4) and additional transformations suitable for numerical integrations. Let us note that the effective gravitational mass [11] associated with (4.4) is not m, but rather M, given by

$$M(t,R) = m + \frac{1}{2}H^2R^3. \tag{4.6}$$

4.3.2 The Function H

Here we are not interested in arbitrary functions H, but only those that reflect, in a general way, the background cosmological model as it is currently understood. In particular, we take $\dot{H} < 0$ for finite t,

$$\lim_{t\to\infty} H = H_0 > 0, \quad \lim_{t\to\infty} \dot{H} = \lim_{t\to\infty} \ddot{H} = 0, \quad \lim_{t\to 0} H = \infty, \tag{4.7}$$

and

$$\lim_{t\to 0} \beta = -\infty. \tag{4.8}$$

These general properties are in fact crucial to the present analysis.

As recognized in KKM, $t = 0$ is not, in general, part of the spacetime. To see this here, from the definition of u and (4.8), we find $\lim_{t\to 0} u = 0$ for all finite r. From the definition (4.3) then we have

$$\lim_{t\to 0} R = \begin{cases} 0 & \text{if } m = 0 \\ \\ \infty & \text{if } m \neq 0 \end{cases} \tag{4.9}$$

and so $t = 0$ is not, for $m \neq 0$, part of the spacetime (and no limit $m \to 0$ exists). This result depends on (4.8) and relaxation of (4.8) gives rise to other more involved possibilities not discussed here.

4.3.3 Scalar Singularities

Let us consider the singularities of (4.4), as revealed by scalars polynomial in the Riemann tensor. It turns out that we need only report the Ricci scalar $\mathcal{R}$, which we find is given by

$$\mathcal{R} = 12H^2 + \frac{6\dot{H}}{\sqrt{1-2m/R}}, \tag{4.10}$$

in agreement with KKM, since all other invariants, derived from (partial) derivatives of the metric tensor no higher than 2, add no new information. For $0 < t < \infty$, there is a singularity at $R = 2m$ ($u = m/2$), which, as is clear from (4.1), is spacelike in agreement with KKM. The apparent singularity at $t = 0$, over the range $2m < R < \infty$ is, as explained above, not part of the spacetime (4.4) due to (4.8).

4.3.4 Asymptotics

With conditions (4.7) let us also consider the asymptotic limit $t \to \infty$, and in particular the roots to $f_0 = 1 - 2m/R - H_0^2 R^2 = 0$. There are three cases: $27m^2H_0^2 > 1$, for which there are no positive roots, $27m^2H_0^2 = 1$, for which there is one (coincident) positive root $R = 3m$, and $27m^2H_0^2 < 1$ for which there are two distinct positive roots that satisfy $0 < 2m < R_- < 3m < R_+$. It is only the last case which is of central interest here. As explained in detail below, we are interested in solutions that asymptote to de Sitter space for R and $t \to \infty$ and become Schwarzschild - de Sitter space for $R \to R_-$ and $t \to \infty$. This requires (e.g. [12])

$$H_0^2 = \Lambda/3 \tag{4.11}$$

where Λ is the cosmological constant. For $27m^2H_0^2 \ll 1$ we note that $R_- \simeq 2m$ and $R_+ \simeq 1/H_0$, the Hubble length (e.g. [14]). The solution discussed here is essentially homogeneous at this length scale.

4.3.5 The Locus $f = 0$

Tangents to the locus $f = 0$, where f is defined by (4.5), are null for $\dot{R} = 2H^2R^2$, that is, $\dot{H} = 2H(3m - R)/R^2$, and timelike for $\dot{R} < 2H^2R^2$. The tangents are spacelike for $\dot{R} > 2H^2R^2$ and for $\dot{R} < 2H^2R^2$ along the branch $dR < 0, dt > 0$. The essential features are summarized schematically in Figure 4.1.

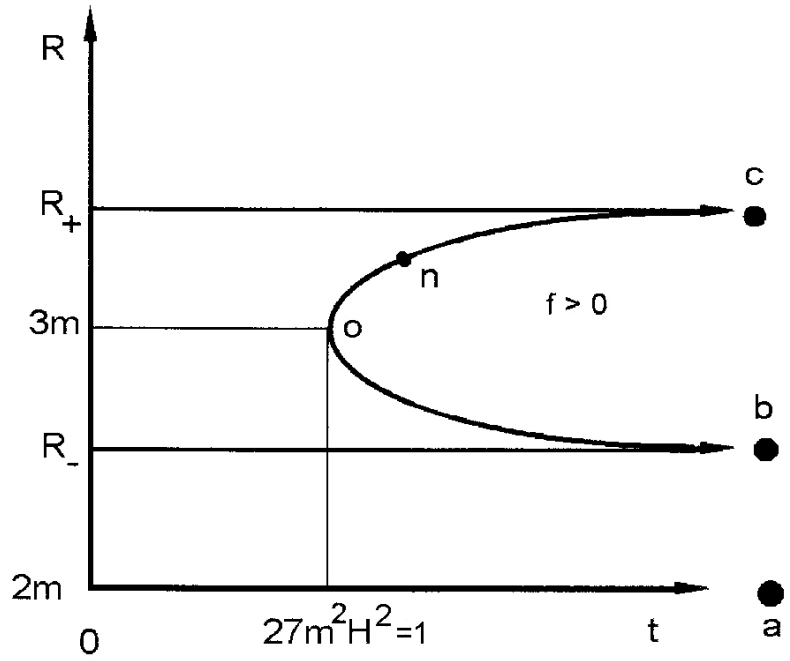

Figure 4.1: The $R-t$ plane and the locus $f=0$. The locus is timelike above and to the right of n where $\dot{H}=2H(3m-R)/R^2$. The locus is spacelike below n. $R=3m$ is also shown. It passes through $f=0$ at o where $t=T$ such that $27m^2H(T)^2=1$. $R=3M$ is spacelike to the left the locus and timelike to the right. The trajectories $R_\pm$ are spacelike. The asymptotic points are defined by $a:(t\to\infty, R=2m)$, b: $(t\to\infty, R=R_-)$ and c: $(t\to\infty, R=R_+)$. These are explained below.

4.4 Null Geodesics - Qualitative

4.4.1 Outgoing and Ingoing Geodesics

Let us first examine, qualitatively, general properties of the radial null geodesics (η) of (4.4). These must satisfy

$$\left.\frac{dR}{dt}\right|_\eta = \sqrt{1-2m/R}\left(HR \pm \sqrt{1-2m/R}\right) \tag{4.12}$$

in agreement with KKM. Now, whereas for the "+" ("outgoing") branch clearly $dR/dt>0$, the "-" ("ingoing") branch requires further examination. From (4.5) and

(4.12) it follows that for the "-" branch $dR/dt > 0$ for $f < 0$, $dR/dt < 0$ for $f > 0$, and $dR/dt = 0$ for $f = 0$. In particular, note that for $f < 0$, $dR/dt > 0$ along both branches of (4.12). It is appropriate here to note from (4.4) that tangents to surfaces of constant finite t are spacelike for $R > 2m$ (and so for finite t we set the future orientation $dt/d\lambda|_\eta > 0$ for affine λ increasing to the future) and tangents to surfaces of constant R are spacelike for $f < 0$, null for $f = 0$ and timelike for $f > 0$.

4.4.2 Expansions

Letting $k^\alpha_\pm$ signify the 4-tangents to the radial null geodesics, the associated expansions $\theta_\pm \equiv \nabla_\alpha k^\alpha_\pm$ follow as

$$\theta_\pm = \frac{2}{R}\sqrt{1-\frac{2m}{R}}\left(HR \pm \sqrt{1-\frac{2m}{R}}\right)\left.\frac{dt}{d\lambda}\right|_\pm , \tag{4.13}$$

where evaluation along η is now understood. This is in agreement with KKM up to the last term which is missing in the KKM analysis. The change in sign of θ_- at $f = 0$ led KKM to refer to $f = 0$ as an "apparent horizon". Normally, this description would be reserved for a change in sign of θ_+ since a change in sign of θ_- does not hide events below $f = 0$ from distant observers. Now to see the importance of the last term in (4.13) consider $t \to \infty$ along ingoing geodesics. Clearly all but the last term $\to 0$. However, as we show below, $t \to \infty$ at finite λ and so the last term in (4.13) diverges and as a result, θ_- becomes indeterminate in these coordinates. The removal of this ambiguity is discussed below.

4.4.3 Infinity

Let us examine the "outer" boundary of (4.4): $(R \to \infty,\ t \to \infty) \equiv \mathcal{I}^+$ (spacelike [13]). The radial null geodesic equations can be written in the form

$$\frac{d^2R}{d\lambda^2} = R(\lambda)\sqrt{1-2m/R(\lambda)}\frac{dH}{dt}\left(\left.\frac{dt}{d\lambda}\right|_{\pm}\right)^2 < 0 \tag{4.14}$$

where the inequality holds for finite t. From (4.14) it follows that $R \nrightarrow \infty$ for finite λ and so both branches are future null geodesically complete [4]. This is no surprise since $\mathcal{I}^+$ is indistinguishable from $\mathcal{I}^+$ for de Sitter space (given (4.11)). The "inner" boundary of (4.4) requires a much more detailed analysis. This is explained below. Here we simply introduce the notation: $(R = R_-, t = \infty) \equiv \mathcal{H}$ (null), and note that

$$f|_{\mathcal{H}} = (R - 2M)|_{\mathcal{H}} = 0, \tag{4.15}$$

and $(R_- < R < \infty, t = \infty) \equiv i^+$.

4.5 A Specific form for H

In order to examine the solutions to (4.12) we must first specify a specific background function H, which satisfies the conditions (4.7) and (4.8), since (4.12) appears to have no analytic solution for general H. Here we choose

$$H = \frac{H_0 \sinh(3H_0 t)}{\cosh(3H_0 t) - 1} = H_0 \coth(\frac{3H_0 t}{2}) \tag{4.16}$$

so as to reflect an asymptotic ΛCDM universe.[5]

[4] The same conclusion has been obtained by Brien Nolan (private communication).

[5] This choice does not limit all of what follows. For example, the completeness/incompleteness arguments given in Appendix A are unaffected by this choice.

4.6 Energy Conditions

Note that we apply the classical energy conditions to (4.1) by way of the Einstein equations (without an explicit cosmological constant). As is clear from (4.2), with our general conditions on H, $\rho > 0$ and $\rho + p > 0$ and so the null and weak energy conditions are satisfied. For the dominant energy condition, $-\rho < p < \rho$ and so from (4.2)

$$-\frac{3}{4}\dot{\beta}^2 < -\frac{3}{4}\dot{\beta}^2 - \frac{\ddot{\beta}}{\sqrt{1-2m/R}} < \frac{3}{4}\dot{\beta}^2. \tag{4.17}$$

Whereas the left hand inequality is always satisfied, given our general conditions on H, the right hand side can be given in the form

$$R(t) > \psi(t)m \tag{4.18}$$

where, from (4.16),

$$\psi = \frac{2(\cosh(3H_0t)+1)^2}{\cosh(3H_0t)(\cosh(3H_0t)+2)}. \tag{4.19}$$

Now whereas the explicit value of ψ at any t depends on H_0, the general form of ψ does not. In particular, $\lim_{t\to 0}\psi = 8/3$ and $\lim_{t\to\infty}\psi = 2$. The function ψ is shown in Figure 4.2. We conclude that the dominant energy condition is satisfied almost everywhere[6].

Finally, the strong energy condition requires $\rho + 3p \geq 0$. From (4.2) it follows that this condition requires

$$\frac{2m}{R(t)} \geq 1 - \frac{\dot{H}^2}{H^4}. \tag{4.20}$$

From (4.16) we find

$$1 - \frac{\dot{H}^2}{H^4} = \frac{(\cosh(3H_0t)+4)(\cosh(3H_0t)-2)}{(\cosh(3H_0t)+4)^2} \tag{4.21}$$

[6]We have no explanation for the curious position of the current epoch in Figure 4.2

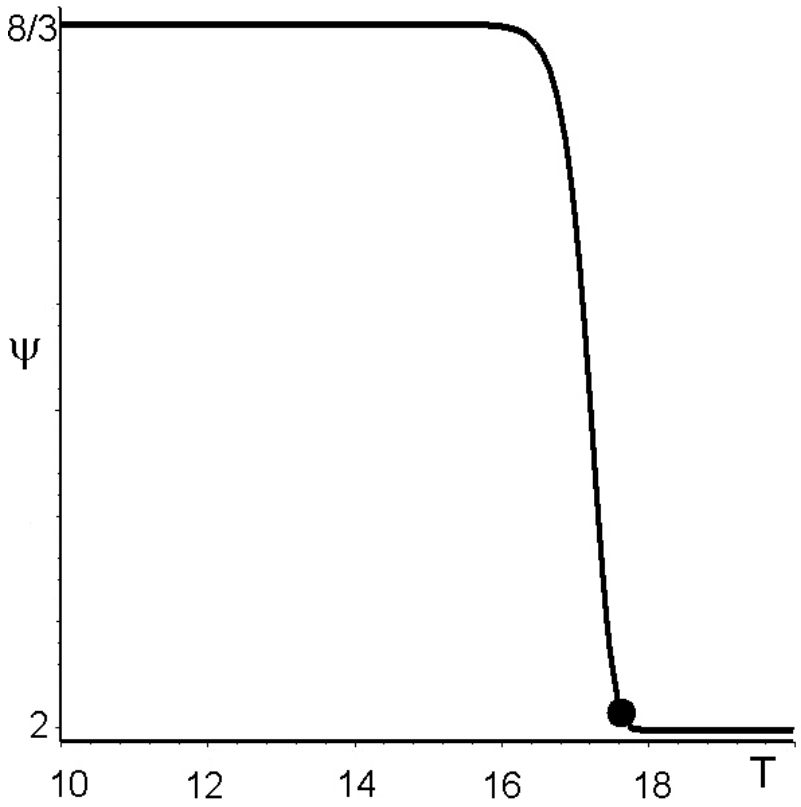

Figure 4.2: The function ψ given by (4.19). The curve has been constructed with $H_0 = 2.3\ 10^{-18} s^{-1}$. T is defined by $t = 10^T$ where $[t] = s$. The current epoch is shown as a dot.

and so we arrive at

$$1 - \frac{\dot{H}^2}{H^4} = \begin{cases} < 0 & t < t_0 \\ = 0 & t = t_0 \\ > 0 & t > t_0 \end{cases} \tag{4.22}$$

where

$$t_0 = \frac{\ln(2+\sqrt{3})}{2H_0} \tag{4.23}$$

and so the strong energy condition is satisfied everywhere for $t \leq t_0$. However, for

$t > t_0$ the strong energy condition is satisfied only for

$$R(t) < \delta(t)m \tag{4.24}$$

where, clearly,

$$\delta = \frac{2(\cosh(3H_0t) + 4)^2}{(\cosh(3H_0t) + 4)(\cosh(3H_0t) - 2)}. \tag{4.25}$$

Since, as it is easy to show, δ drops rapidly from ∞ at t_0 to $(\lim_{t\to\infty} \delta\, =)2$, we conclude that the strong energy condition is eventually satisfied almost nowhere, as expected.

4.7 Integration of the null geodesics

4.7.1 Integration of (4.12) in the $R - t$ plane

We now examine numerical solutions to the null geodesic equations (4.12), subject to the choice (4.16). First, consider the outgoing geodesics given by "+" in (4.12). The integrations are shown in Figure 4.3. These geodesics are monotone in the $R-t$ plane. In contrast, the ingoing geodesics ("-" in (4.12)) show considerably more structure. This is shown in Figure 4.4. We find 5 distinct types of evolution. Moving from the bottom right to the upper left in Figure 4.4 we find: (i) Geodesics which asymptote monotonically to $\mathcal{H}$ (again, defined by $(R = R_-, t = \infty)$) without crossing the locus $f = 0$, (ii) A last geodesic that asymptotes monotonically to $\mathcal{H}$ without crossing $f = 0$ (call it η_2), (iii) Geodesics which reach a maximum $R < R_+$ at $f = 0$ and then asymptote monotonically to $\mathcal{H}$, (iv) A last geodesic that asymptotes monotonically to R_+ and terminates in i^+(call it η_1), and (v) Geodesics that cross R_- and R_+ and monotonically evolve to $\mathcal{I}^+$. Now the cases (i) and the limit (ii), are absent

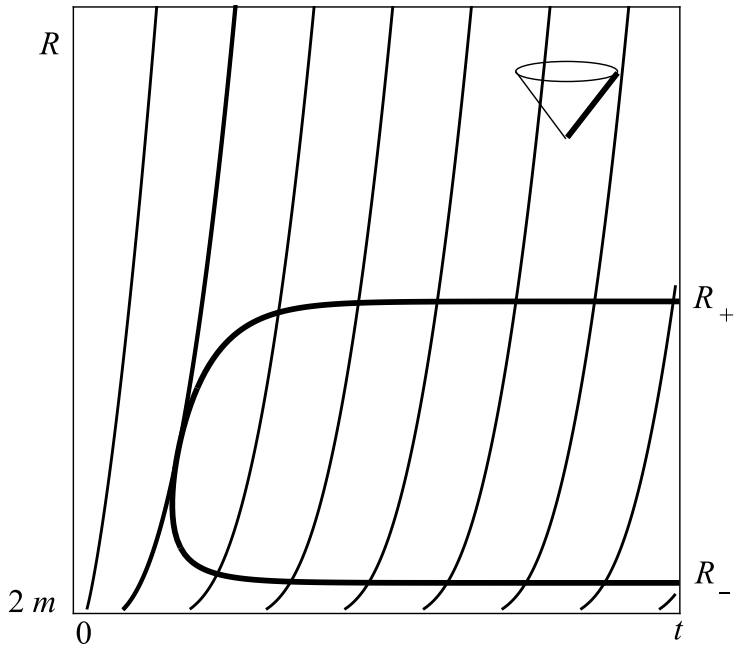

Figure 4.3: The outgoing solutions of the null geodesic equation (4.12) under the condition (4.16). The values taken are $H_0 = 1/3$ and $m = (1/(H_0 l_0)) = 958041/2000000 \sim 0.479$ (where l_0 is defined below). These values are of no consequence as we are simply interested in the qualitative behaviour of the solutions to (4.12). The locus $f = 0$ is also shown. The values of the roots $R_\pm$ are $R_+ \sim 2.29$ and $R_- \sim 1.11$. The cone shows the "leg" of the null cone under consideration.

in the KKM analysis, but are central to our examination of the inner boundary of (4.4). Since the form (4.12) is particularly sensitive to error for these cases, we now introduce new coordinates to demonstrate, in more detail, that there do indeed exist ingoing null geodesics that reach $\mathcal{H}$ without crossing $f = 0$.

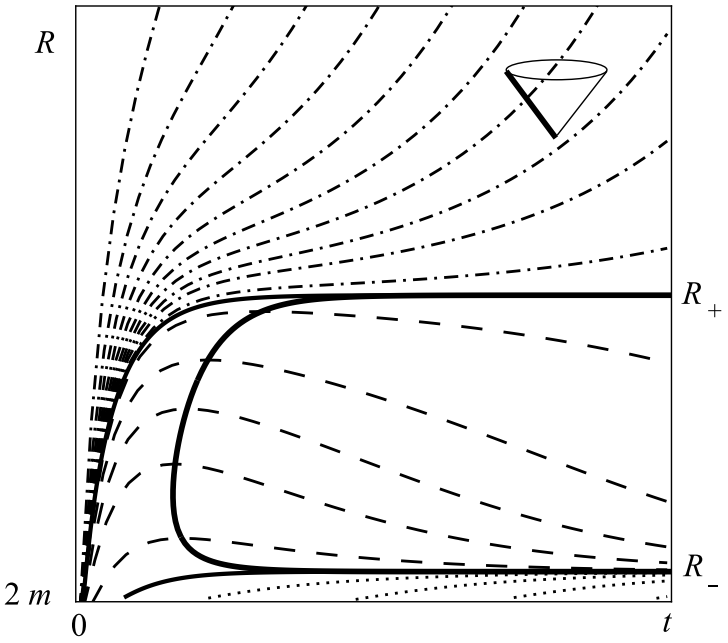

Figure 4.4: The ingoing solutions of the null geodesic equation (4.12) under the same conditions as Figure 4.3.

4.7.2 Integration of (4.12) in the $z - l$ plane

We recast the problem as follows: Let [7]

$$z \equiv \sqrt{1 - \frac{2m}{R}}, \tag{4.26}$$

and let

$$l \equiv \frac{1}{Hm}. \tag{4.27}$$

We observe the ranges

$$(R = 2m) \quad 0 < z < 1 \quad (R \to \infty) \tag{4.28}$$

and

$$(t \to 0) \quad 0 < l < l_0 \equiv \frac{1}{H_0 m} \quad (t \to \infty). \tag{4.29}$$

[7]This useful definition for z was pointed out to us by Brien Nolan (private communication).

With the definitions (4.26) and (4.27), equation (4.12) takes the form (using the asymptotic ΛCDM model as before)

$$\frac{dz}{dl} = \left(\frac{1-z^2}{l} - \frac{z(1-z^2)^2}{2}\right)\left(\frac{l_0^2}{3(l_0^2-l^2)}\right). \tag{4.30}$$

for the ingoing case. At first sight this might not appear to simplify things, but it does. First note that we need only specify l_0. For the case of central interest ($27m^2H_0^2 < 1$) we have

$$l_0 > 3\sqrt{3}. \tag{4.31}$$

As regards initial conditions, we have

$$\left.\frac{dz}{dl}\right|_{z=0,l=l_1} = \frac{l_0^2}{3l_1(l_0^2-l_1^2)} \tag{4.32}$$

which is regular over the range

$$0 < l_1 < l_0. \tag{4.33}$$

Moreover, we have

$$\frac{dz}{dl}\begin{cases} > 0 & f < 0, l < \frac{2}{z(1-z^2)} \\ = 0 & f = 0, l = \frac{2}{z(1-z^2)} \\ < 0 & f > 0, l > \frac{2}{z(1-z^2)}. \end{cases} \tag{4.34}$$

Numerical integrations are shown in Figure 4.5. Our conclusion is that null geodesics that reach $\mathcal{H}$ without crossing $f = 0$ are a fundamental feature of this solution.

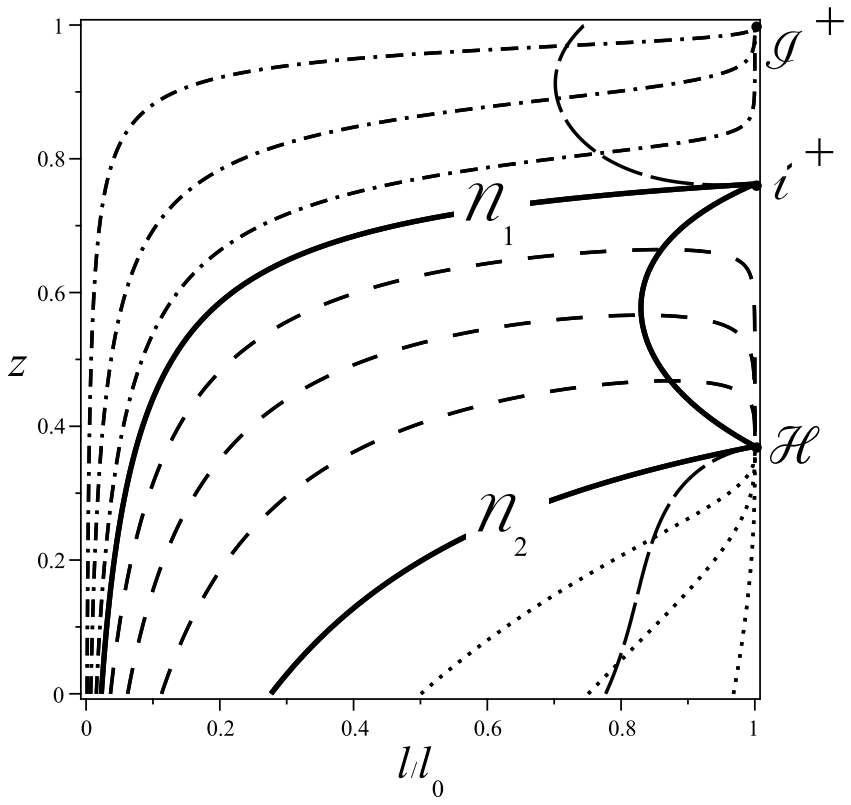

Figure 4.5: Integration of (4.30) for $l_0 = 2000000/319347 \sim 6.263$ so that $z_- = 37/100$ and $z_+ = -37/200 + 35893^{1/2}/200 \sim 0.76$ over the range $0 < l < l_0$. The limiting geodesics η_1 and η_2 are shown as is the locus $f = 0$ (which connects $\mathcal{H}$ with i^+). The dashed curves connecting $z = 0$ and $\mathcal{H}$ and i^+ with $z = 1$ indicate $d^2z/dl^2 = 0$.

4.8 Global structure of the spacetime

4.8.1 Construction of the Conformal Diagram

The conformal representation of a spacetime (Penrose - Carter diagram [15]) is, of course, not unique in detail. However, all conformal representations must show the global structure of the spacetime.[8] Here we construct the Penrose - Carter diagram in the following way: The construction of the diagram starts by solving the null

[8]All cases considered here are time-symmetric in the sense that the diagrams can be flipped upside down. Moreover, all diagrams can be rotated, interchanging the left and right hand sides.

geodesic equations numerically. This gives a general understanding of the global behavior of the spacetime. In the present case, all of the outgoing geodesics and all of the ingoing geodesics originate from the singularity at $R = 2m$. These geodesics intersect with $R = 2m$ at some finite value of $t > 0$. That is, any point in the spacetime $(t > 0, R > 2m)$ can be connected to the past boundary $(R = 2m, t > 0)$ by a unique null geodesic from each branch. We represent the boundary $R = 2m$ as a horizontal line in a Cartesian plane $(y = 0, -1 \leq x \leq 1)$, setting the right end of $R = 2m$ at $t = 0$, and the left end at $t = \infty$. To represent the interval $0 < t < \infty$, from $x = -1$ to 1, we use the transformation function

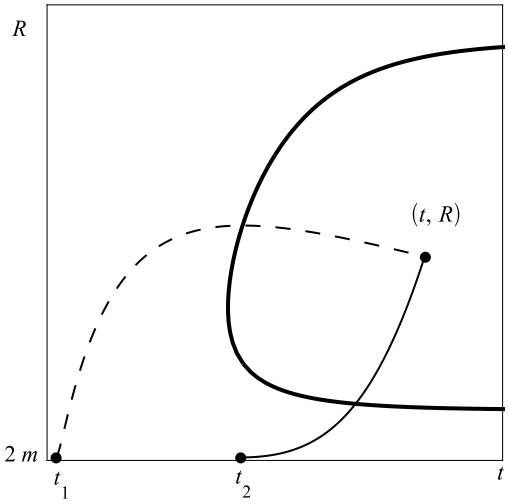

Figure 4.6: Locating t_1 and t_2 for any event via null geodesics. The locus $f = 0$ is shown. Note that t increases to the right.

$$t = A(1-x)^B \tan\left((1-x)\frac{\pi}{4}\right), \tag{4.35}$$

where A and B are adjustable constants. A represents the value of t at the center of the line $x = 0$ and B adjusts the position of b. These constants have no physical significance and where adjusted only for visual presentation (we chose $A \sim 0.39$ and

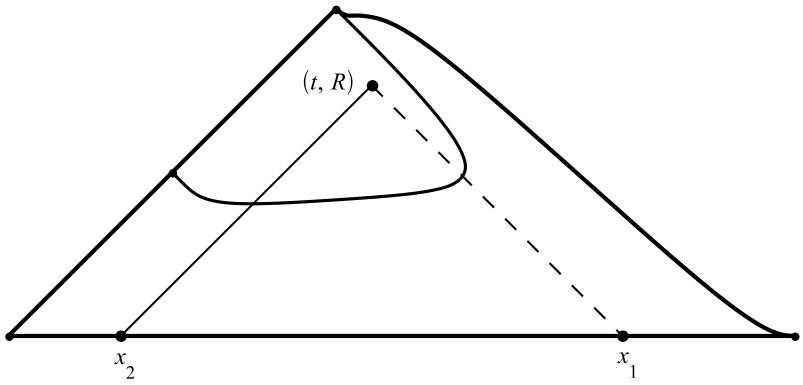

Figure 4.7: Conformal representation of the event (t, R). The locus $f = 0$ is shown. Note that t increases to the left.

$B \sim 0.75$). Once this line is adopted [16], any point in the spacetime can be projected onto the conformal diagram by solving for both null geodesics that pass through any point, and numerically solving for the value of t at which these two curves reach $R = 2m$; say t_1, and t_2. This is illustrated in Figure 4.6. Once these two values of t are found, we can represent them in the conformal diagram by solving for x in (4.35). This gives us x_1 and x_2. Finally, we find the conformal representation of the original point by finding the intersection of the same two null geodesics, but presented in the conformal diagram as $y = -x + x_1$ for one geodesic, and $y = x - x_2$ for the other. This is illustrated in Figure 4.7. By our choice (4.35), all diagrams are strongly compactified in the region $R > R_+$.

4.8.2 Null geodesics

Under the procedure described above, Figure 4.3 is mapped into the right hand side of Figure 4.8 and Figure 4.4 is mapped into the left hand side of Figure 4.8.

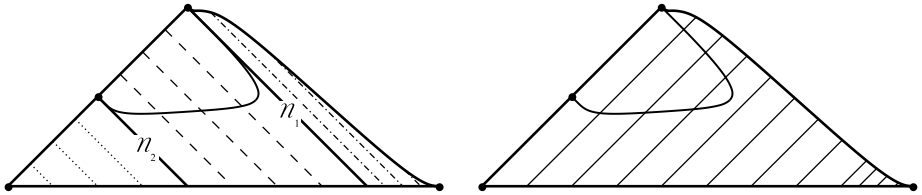

Figure 4.8: At right, the conformal representation of the outgoing null geodesics as given in Figure 4.3. The locus $f = 0$ is shown. The bottom horizontal line represents the singularity $R = 2m$. At left the conformal representation of the ingoing null geodesics as given in Figure 4.4.

4.8.3 Surfaces of constant R and t

Using the same procedure, at the left in Figure 4.9 we show surfaces of constant t and at the right in Figure 4.9 we show surfaces of constant R. The surfaces of constant t are spacelike for all finite t. The surfaces of constant R are spacelike for $f < 0$ and timelike for $f > 0$.

4.8.4 The fluid streamlines

The streamlines $r = constant$ can be written out explicitly in $z - l$ coordinates in the form

$$z(l) = \tanh\left(\frac{1}{6}\log\left(\left(\frac{l^2}{l_1^2}\right)\left(\frac{l_0^2 - l_1^2}{l_0^2 - l^2}\right)\right)\right) \tag{4.36}$$

where $z(l_1) = 0$. Transforming to the $R - t$ plane, these streamlines take the form

$$R(t) = 2m\cosh\left(\frac{1}{6}\log\left(\frac{H(t_1)^2 - H_0^2}{H(t)^2 - H_0^2}\right)\right) \tag{4.37}$$

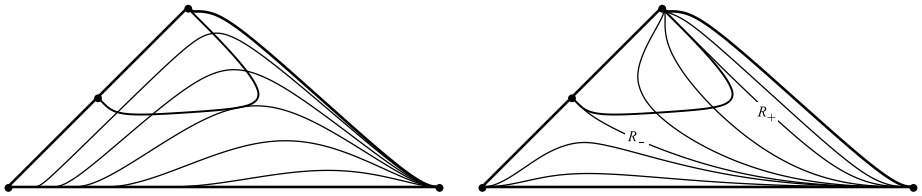

Figure 4.9: At left the conformal representation of surfaces of constant t. The locus $f = 0$ is also shown. Moving from the bottom right to the upper left we have: $t_0 < t < T$ (where $27m^2H(T)^2 = 1$), $t = T$, $t = t_1 > T$ and $t_2 > t_1$. The boundary has $t \to \infty$. At right the conformal representation of surfaces of constant R. The locus $f = 0$ is also shown. Moving from the bottom left to the upper right we have: $2m < R_0 < R < R_-$, $R = R_-$, $R_- < R < 3m$, $R = 3m$, $R = R_+$, $R_1 > R_+$. The right boundary has $R \to \infty$ and the left boundary has $R = R_-$.

where $R(t_1) = 2m$. These streamlines are shown in Figure 4.10. Note that the streamlines do not cross $\mathcal{H}$. This fact can be considered the source of relation (4.15) and is the central part of the original construction [1].

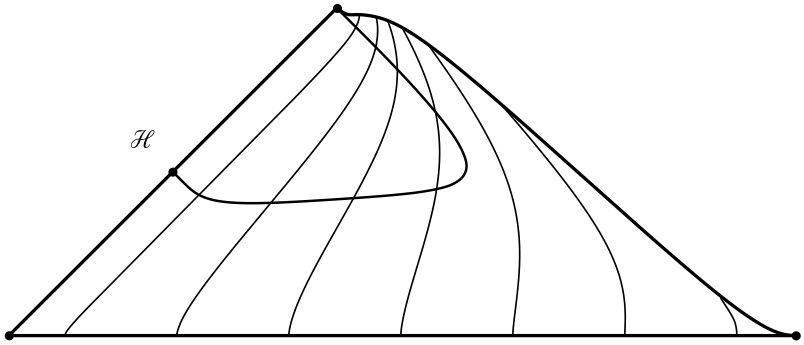

Figure 4.10: The fluid streamlines $r = constant > 0$ in the conformal diagram. The streamlines are timelike and r increases to the right. Note that the streamlines do not cross $\mathcal{H}$ which is the limit $r \to 0$.

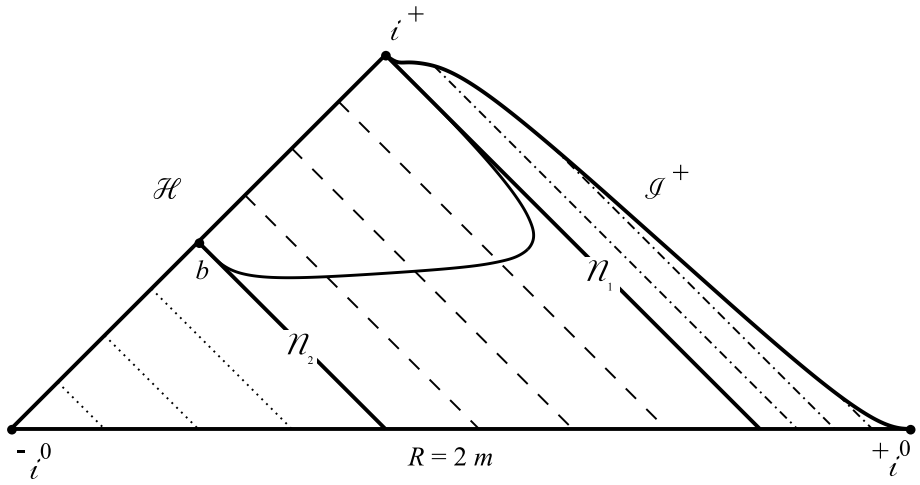

Figure 4.11: The conformal representation of the boundary to the spacetime (4.4) given (4.16). The boundary is defined as follows: The singularity $R = 2m$, $\mathcal{I}^+ \equiv (R = \infty, t = \infty)$, $i^+ \equiv (R_- < R < \infty, t = \infty)$, $\mathcal{H} \equiv (R = R_-, t = \infty)$, $^-i^0 \equiv (2m \leq R < R_-, t \to \infty)$ and $^+i^0 \equiv (2m \leq R < \infty, t > 0)$.

4.8.5 The boundary and ingoing geodesics

In Figure 4.11 we summarize the boundary of (4.4) and classify ingoing null geodesics which do not terminate on $\mathcal{I}^+$. We are now in a position do discuss the affine completeness/incompleteness of these geodesics. As is discussed in detail in Appendix A, all these geodesics are incomplete except η_1 which we find to be complete. This incompleteness is the central point in KKM, but their analysis revealed only the section (b, i^+) of $\mathcal{H}$. Here we observe that η_2 terminates at b on $\mathcal{H}$ and we observe very special properties associated with b as explained in Appendix B: b is characterized by vanishing expansion for both the ingoing and outgoing radial null geodesics. This is the hallmark of a bifurcation two - sphere. This bifurcation two - sphere divides $\mathcal{H}$ into two sections: a "black hole" horizon to the future of b and a "white hole" horizon to the past of b. This is explored in the completion to the spacetime given below.

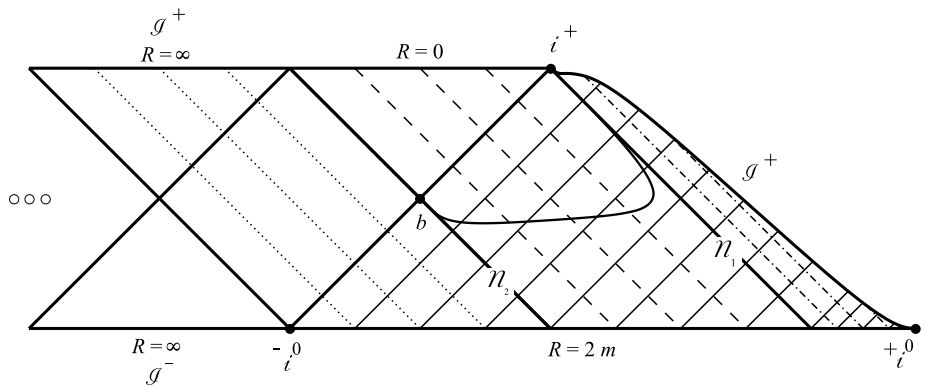

Figure 4.12: An extension of the McVittie spacetime which is null geodesically complete. The inner bifurcate two - sphere of the Schwarzschild - de Sitter spacetime (b) is identified with that of the McVittie spacetime.

4.8.6 A completion

One possible extension of the McVittie spacetime, which is null geodesically complete, is shown in Figure 4.12 where we have identified the inner bifurcation two - sphere of the Schwarzschild - de Sitter spacetime with that of the McVittie spacetime [20]. This enlarged spacetime now has a center of symmetry, the center of the Schwarzschild - de Sitter black hole at $R = 0$. Ingoing null geodesics below η_1 but above η_2 terminate at the singularity $R = 0$ in the Schwarzschild - de Sitter black hole. Whereas η_2 joins onto the "left" black hole horizon of the Schwarzschild - de Sitter spacetime, all "ingoing" geodesics below η_2 have R monotonically increasing, pass through the white hole horizon and terminate at $R = \infty$, that is, $\mathcal{I}^+$ of the Schwarzschild - de Sitter spacetime. Whereas the degenerate case $27m^2H_0^2 = 1$ is outside the cases of interest from a physical point of view, it offers a very instructive limit from a mathematical point of view since η_1 and η_2 then coincide and b disappears. This is examined in Appendix C.

4.9 Discussion

We have performed a detailed study of a particular McVittie solution, by way of the specification of a characteristic function, that asymptotes to the standard ΛCDM cosmology and that contains an inner boundary that is a slice of the extended Schwarzschild - de Sitter spacetime. We have found that this inner boundary contains a bifurcation two - sphere where the expansion of both the ingoing and outgoing radial null geodesics vanishes. To the future of this bifurcation on this inner boundary we have found a black hole horizon at finite affine distance and therefore we corroborate the main conclusion in the work of Kaloper, Kleban and Martin. In addition, however, we have found a white hole horizon to the past of the bifurcation which is also at finite affine distance. In the degenerate limit of this particular solution the bifurcation two - sphere and black hole horizon disappear leaving only the white hole horizon, also at finite affine distance. We have shown that the null and weak energy conditions are satisfied and that the dominant energy condition is satisfied almost everywhere. The global structure of the solution has been constructed systematically based on detailed numerical integrations of the null geodesic equations. In the case $H_0 = 0$, the work of Kaloper, Kleban and Martin suggested that the would - be horizon forms a weak null singularity. In Appendix D we argue that this is not the case. Moreover, we argue that this case is rather less interesting than $H_0 > 0$ since the solutions can have a black hole horizon to the future of the singularity at $R = 2m$ or a white hole horizon to the past of $R = 2m$.

The present analysis relies on the (standard) condition (4.8). Relaxing this, it is clear that we can maintain the conditions (4.7) but also violate (4.9). This means that in general the initial singularity will consist of two parts: the “pressure” singularity

at $R = 2m$, and a generalized "big bang" singularity at $t = 0$. In a sense this shows how "delicate" the solution is. The fact that the McVittie solution cannot represent a physically realistic inhomogeneity is, we think, best shown by a glance at Figure 4.10 and equation (4.15). By construction, no fluid streamlines can cross $\mathcal{H}$ and so the black and white hole horizons are present here by way of mathematical extensions, not physical processes. There is no easy fix for this situation, within the context of McVittie's approach, since a routine calculation shows that (4.1) is a perfect fluid if and only if $dm/dt = 0$. Nonetheless, the present analysis shows that a rather routine looking spacetime, like (4.1), can in fact harbor a rather exotic interior. Moreover, the present analysis suggests that the very notion of an inhomogeneity in cosmology may go beyond the concept of inhomogeneity in elementary physical variables.

What we have done here can be expanded in a number of ways. First, of course, one could relax condition (4.16) and consider a wider class of possibilities. In all cases one would find that if the vacuum boundary ($\mathcal{H}$) contains a bifurcate two - sphere, then this bifurcate two - sphere is also part of the McVittie solution itself. This geometric behaviour can be traced to McVittie's no - flux condition which preserves the integrity of $\mathcal{H}$. One can reasonably expect that the integrity of $\mathcal{H}$ is destroyed by any flux through it. To conclude, we believe that the McVittie solution is an instructive idealization very much like the Kruskal - Szekeres extension.

4.10 Appendix

4.10.1 Ingoing null geodesics

The arguments presented here[9] do not rely on a specific form for H. We are concerned only with ingoing radial null geodesics. It is convenient to write the associated null geodesic equation in the form

$$\frac{d^2t}{d\lambda^2} = -\left(\frac{H(1-\frac{m}{R})}{\sqrt{1-\frac{2m}{R}}} - \frac{2m}{R^2}\right)\left(\frac{dt}{d\lambda}\right)^2. \tag{4.38}$$

η_1

Along η_1, $f < 0$ and defining

$$h(R) \equiv \left(\frac{3m}{R} - 1\right)\frac{1}{R} \tag{4.39}$$

we have

$$\frac{d^2t}{d\lambda^2} < h(R)\left(\frac{dt}{d\lambda}\right)^2. \tag{4.40}$$

Now along η_1, R is strictly increasing to $R_+ > 3m$ and so $h(R)$ eventually becomes negative. Define some fiducial R_0 so that

$$h(R_0) = -\alpha \tag{4.41}$$

where $0 < \alpha < 1/12m$. Now (4.41) gives

$$R_0^{\pm} = \frac{1 \pm \sqrt{1-12\alpha m}}{2\alpha} \tag{4.42}$$

[9]Some of the conclusions in this Appendix (and we expect by now all) have also been obtained by Brien Nolan.

and since we can always choose α sufficiently small (but not zero) so that $R_0^- < R_+ < R_0^+$ we eventually have

$$\frac{d^2t}{d\lambda^2} < -\alpha \left(\frac{dt}{d\lambda}\right)^2 \tag{4.43}$$

along η_1 for $\lambda >$ some λ_*. Now write

$$\frac{dt}{d\lambda} = T \tag{4.44}$$

so that from (4.38) we have

$$\frac{dT}{d\lambda} < -\alpha T^2. \tag{4.45}$$

Integrating (4.45) we have

$$T < \frac{1}{\alpha(\lambda - \lambda_*) - 1/T_*}. \tag{4.46}$$

Finally, integration of (4.46) gives

$$t - t_* < \frac{1}{\alpha} \ln(T_* \alpha(\lambda - \lambda_*) + 1). \tag{4.47}$$

From (4.47) it follows that $t \nrightarrow \infty$ for finite λ and so η_1 is geodesically complete.

(b, i^+)

We consider the ingoing geodesics which reach $\mathcal{H}$ within the range (b, i^+). Sufficiently close to $\mathcal{H}$, R is strictly decreasing and $f \geq 0$ with equality holding only on $\mathcal{H}$. We now have

$$\frac{d^2t}{d\lambda^2} \geq h(R) \left(\frac{dt}{d\lambda}\right)^2 \tag{4.48}$$

where we continue to use (4.39). Now since R approaches $R_- < 3m$, $h(R)$ is strictly positive and increasing. Again, for some fiducial R_0, but now $> R_-$, write $h(R_0) =$

$\alpha > 0$. We now have

$$\frac{d^2t}{d\lambda^2} \geq \alpha \left(\frac{dt}{d\lambda}\right)^2 \tag{4.49}$$

for $\lambda >$ some λ_*. Now integrating in parallel to the details given in the above case we arrive at

$$t - t_* \geq \frac{1}{\alpha} \ln \left(\frac{1}{T_* \alpha (\lambda_* - \lambda) + 1} \right). \tag{4.50}$$

From (4.50) it follows that $t \to \infty$ for finite λ and so ingoing geodesics that reach $\mathcal{H}$ in the range (b, i^+) are geodesically incomplete. This observation is the principle contribution given in KKM.

$({}^-i^0, b]$

Finally, we consider the ingoing geodesics which reach $\mathcal{H}$ within the range $({}^-i^0, b]$. This includes η_2. Now R is strictly increasing and $f \leq 0$ with equality holding only on $\mathcal{H}$. We now have

$$\frac{d^2t}{d\lambda^2} \leq h(R) \left(\frac{dt}{d\lambda}\right)^2 \tag{4.51}$$

where we continue to use (4.39). Now since R approaches $R_- < 3m$, $h(R)$ is strictly positive and decreasing. Again, for some fiducial $R_0 < R_-$, write $h(R_0) = \alpha > 0$. We now have

$$\frac{d^2t}{d\lambda^2} \leq \alpha \left(\frac{dt}{d\lambda}\right)^2 \tag{4.52}$$

for $\lambda >$ some λ_*. Now integrating in parallel to the details given in the above cases we arrive at

$$t - t_* \leq \frac{1}{\alpha} \ln \left(\frac{1}{T_* \alpha (\lambda_* - \lambda) + 1} \right). \tag{4.53}$$

From (4.53) it follows that $t \to \infty$ for finite λ and so ingoing geodesics that reach $\mathcal{H}$ in the range $(^{-}i^{0}, b]$ are also geodesically incomplete.

4.10.2 Bifurcation two - spheres

A bifurcation two - sphere is usually discussed in terms of a vanishing time-translational Killing vector (e.g. [17]). Here we define a bifurcation two - sphere in terms of the simultaneous vanishing of both the ingoing and outgoing radial null geodesic expansions. First, for clarity, let us review the situation in the Schwarzschild vacuum. As shown in [18], the Kruskal - Szekeres metric can be given as

$$ds^2 = (2M)^2 d\tilde{s}^2 \tag{4.54}$$

with

$$d\tilde{s}^2 = \frac{-4}{(1+\mathcal{L})e^{1+\mathcal{L}}} du dv + (1+\mathcal{L})^2 d\Omega_2^2 \tag{4.55}$$

where

$$\mathcal{L} \equiv \mathcal{L}(-\frac{uv}{e}) \tag{4.56}$$

and $\mathcal{L}$ is the Lambert W function [19]. Trajectories with tangents $k^\alpha = e^{\mathcal{L}}(1+\mathcal{L})\delta^\alpha_v$ (constant $u = u_0, \theta$ and ϕ) are radial null geodesics given by

$$v(\lambda) = \lambda e^{-\frac{u_0 \lambda}{e}} \tag{4.57}$$

where λ is an affine parameter and we note the expansion

$$\nabla_\alpha k^\alpha = \frac{-2u_0}{e(1+\mathcal{L})}. \tag{4.58}$$

Trajectories with tangents $l^\alpha = e^{\mathcal{L}}(1+\mathcal{L})\delta^\alpha_u$ (constant $v = v_0, \theta$ and ϕ) are radial null geodesics given by

$$u(\lambda) = \lambda e^{-\frac{v_0 \lambda}{e}} \tag{4.59}$$

and we now note the expansion

$$\nabla_\alpha l^\alpha = \frac{-2v_0}{e(1+\mathcal{L})}. \tag{4.60}$$

On the horizons $u = 0$ and $v = 0$ then v and u are affine parameters. The bifurcation two - sphere is given by $u = v = 0$ and it is uniquely characterized by $\nabla_\alpha k^\alpha = \nabla_\alpha l^\alpha = 0$.

The McVittie solution under consideration in this paper reduces [20] to the Schwarzschild - de Sitter spacetime on $\mathcal{H}$ and so we need a more general construction. We follow [21]. It is shown there that for all static metrics

$$ds^2 = -f dt^2 + \frac{dr^2}{f} + r^2 d\Omega_2^2, \tag{4.61}$$

where f is a polynomial with simple root(s),

$$f(r) = (r-a)h(r) \tag{4.62}$$

where $h(a) \neq 0$, one can construct regular extensions about $r = a$ via the transformations

$$uv = \pm(r-a)\exp(\int 2\kappa \frac{k(r)}{h(r)} dr + \mathcal{E}), \tag{4.63}$$

where the sign depends on how we choose to orientate the $u - v$ axis, $\mathcal{E}$ is a constant and

$$\left|\frac{v}{u}\right| = \exp(2\kappa t) \tag{4.64}$$

where κ is the surface gravity given by

$$\kappa \equiv \frac{1}{2}\frac{df}{dr}\Big|_a \neq 0. \tag{4.65}$$

Note that according to (4.63) $r = r(uv)$ and $r'|_a \neq 0, ' \equiv d/duv$. Under these transformations the Killing vector $\eta^\alpha = \delta^\alpha_t$ becomes $\eta^\alpha = (u, -v, 0, 0)$ and one recovers the usual definition of the bifurcation two - sphere at $u = v = 0$. Note that the specified

construction can always be done. However, about a distinct root, say $r = b \neq a$, a new chart must be constructed about $r = b$.

To calculate null geodesic expansions note that the metric takes the form

$$ds^2 = K(r)dudv + r^2 d\Omega_2^2 \tag{4.66}$$

where

$$K(r) \equiv \pm \frac{ah(r)}{\kappa^2} \exp(-2\kappa \int \frac{k(r)}{h(r)} dr). \tag{4.67}$$

The integration constant has been absorbed into the factor a and again the choice of sign determines the orientation of the $u-v$ axis. Trajectories with tangents $k^\alpha = \frac{\delta^\alpha_v}{K(r)}$ (constant $u = u_0, \theta$ and ϕ) are radial null geodesics with expansions

$$\nabla_\alpha k^\alpha = \frac{u_0}{K(r)r} r', \tag{4.68}$$

and trajectories with tangents $l^\alpha = \frac{\delta^\alpha_u}{K(r)}$ (constant $v = v_0, \theta$ and ϕ) are radial null geodesics with expansions

$$\nabla_\alpha l^\alpha = \frac{v_0}{K(r)r} r'. \tag{4.69}$$

The bifurcation two - sphere associated with any non - degenerate horizon at $r = a$ is therefore characterized by the simultaneous vanishing of both the ingoing and outgoing radial null geodesic expansions; $\nabla_\alpha k^\alpha = \nabla_\alpha l^\alpha = 0$.

4.10.3 The degenerate case $27m^2H_0^2 = 1$

Since $\dot{H} < 0$, $f_0 \geq f$. In the degenerate case $27m^2H_0^2 = 1$ and so

$$f \leq -\frac{(3m - R)^2(6m + R)}{27m^2R}. \tag{4.70}$$

Throughout the associated McVittie solution $f < 0$ and $f = 0$ only at the horizon $\mathcal{H}$ where $R = 3m$. As a result, all ingoing and outgoing radial null geodesics have

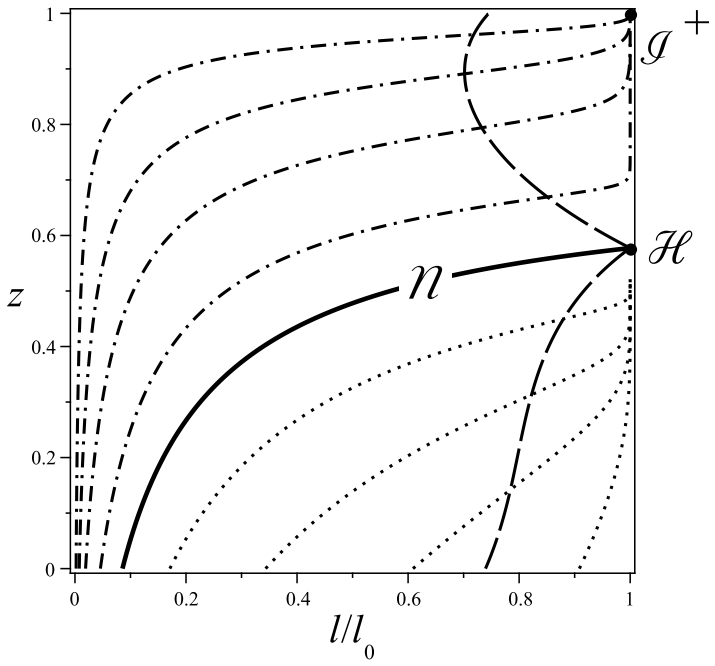

Figure 4.13: As in Figure 4.5 but for $l_0 = 1/H_0 m = 3\sqrt{3}$ (again we take $H_0 = 1/3$). The limiting geodesics η_1 and η_2 now coincide and give η. There is no locus $f = 0$. The dashed curves connecting $z = 0$ and $\mathcal{H}$ and $\mathcal{H}$ with $z = 1$ indicate $d^2z/dl^2 = 0$.

$dR/dt > 0$ and there can be no bifurcation two - sphere. All ingoing geodesics that reach $\mathcal{H}$ do so without crossing $f = 0$ first and as in the non - degenerate case we find that these ingoing geodesics are incomplete. The ingoing radial null geodesics in the $z - l$ plane are shown in Figure 4.13.

A possible extension of the associated McVittie solution is shown in Figure 4.14 where we have used the mapping function

$$t = A(1 - x)\tan\left((1 - x)\frac{\pi}{4}\right) \tag{4.71}$$

with $A \sim 1.9$ and a degenerate Schwarzschild - de Sitter "interior".

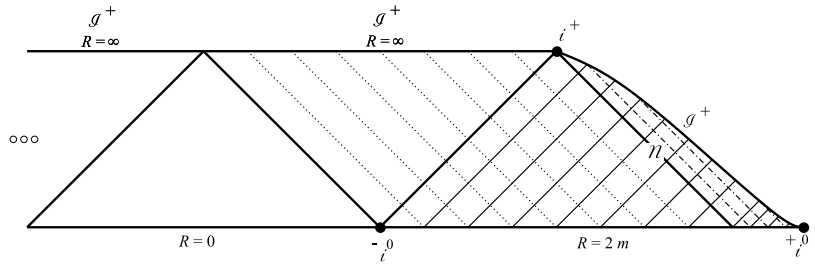

Figure 4.14: As in Figure 4.12 but now for the degenerate case.

4.10.4 $H_0 = 0$

The case $H_0 = 0$ proceeds in a fundamentally different way than the case $H_0 > 0$. To see this, consider the usual background of "dust" so that $H = 2/3t$. Defining $x = R/m$ and $T = t/m$ the locus $f = 0$ takes the form

$$T = \frac{2x^{3/2}}{3\sqrt{x-2}} \tag{4.72}$$

and so surfaces of constant t never intersect the locus for $t < 2\sqrt{3}m$, intersect it once for $t = 2\sqrt{3}m$ and intersect it twice for $t > 2\sqrt{3}m$. Moreover, every surface of constant R, for $2m < R < \infty$, crosses the locus once and at finite t. This last point shows us that eventually all ingoing radial null geodesics have $f > 0$ and so eventually $dR/dt < 0$. There is no bifurcation two - sphere in this McVittie spacetime. To integrate the radial null geodesics we continue to use (4.26) but replace (4.27) with

$$l = \frac{1}{1+mH}. \tag{4.73}$$

The radial ingoing null geodesic equations now take the form

$$\frac{dz}{dl} = \frac{(1-z^2)^2}{6(1-l^2)}\left(\frac{2(1-l)}{l(1-z^2)} - z\right). \tag{4.74}$$

The integrations are shown in Figure 4.15. Using the same procedures as before, the surfaces of constant R and constant t are shown in Figure 4.16. We find that $\mathcal{H}$ is at

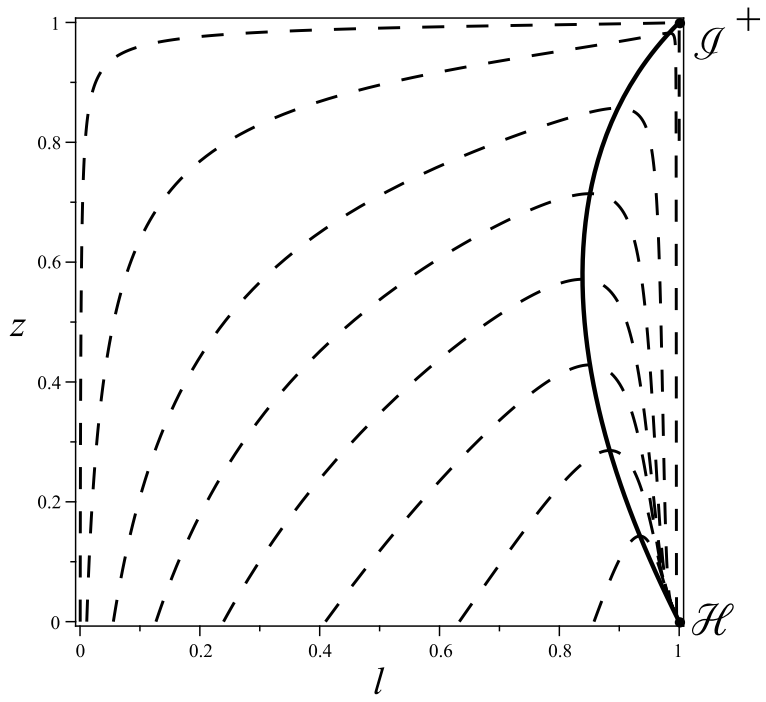

Figure 4.15: As in Figure 4.5 but for $H_0 = 0$. Note that $\mathcal{H}$ is now given by ($R = 2m, t = \infty$).

finite affine distance along ingoing null geodesics but $\mathcal{I}^+$ is at infinite affine distance along outgoing null geodesics (this spacetime is asymptotically flat).

The conformal diagram and a possible extension onto the Kruskal - Szekeres manifold is shown in Figure 4.17. There is now a black hole horizon to the future of the singularity and a white hole horizon in the past. These now form a wedge, not a straight line.

Now KKM argue, their considerations motivated by quantum gravity arguments, that the invariant

$$\Delta \equiv \nabla_\iota \nabla_\epsilon R_{\alpha\beta\gamma\delta} \nabla^\iota \nabla^\epsilon R^{\alpha\beta\gamma\delta} \tag{4.75}$$

diverges on the horizon. It is difficult to see how this would come about since at the

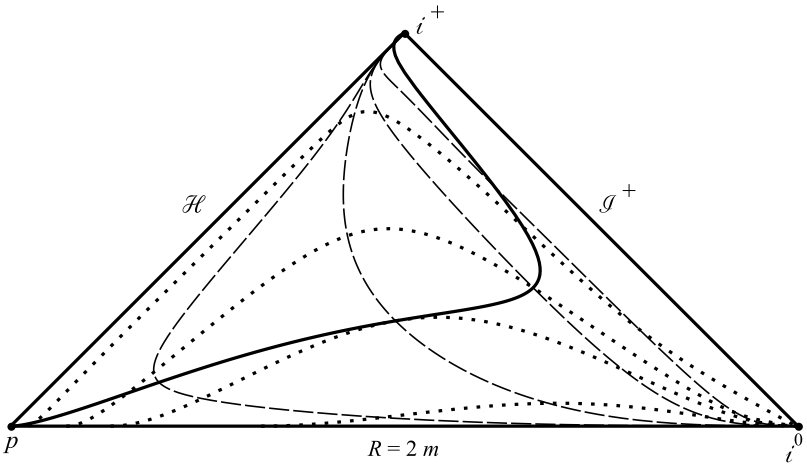

Figure 4.16: Conformal representation of surfaces of constant R (dashed) and constant t (dots) for the case $H_0 = 0$. The locus $f = 0$ from p to i^+ is shown (solid).

horizon, using conditions (4.7), with $H_0 \geq 0$, the metric tensor along with all first and second order (partial derivatives) are continuous. Using GRTensor II [22], and assuming H is $\in C^3$, we find

$$\lim_{t\to\infty} \Delta = \frac{1440m^2}{R^{12}}(H_0^2R^3(11H_0^2R^3 - 24R + 50m) + 14R^2 - 60Rm + 65m^2) \quad (4.76)$$

where evaluation along η_- is understood. We see no divergence for $R > 0$.

4.11 acknowledgments

This work was supported in part by a grant from the Natural Sciences and Engineering Research Council of Canada (to KL) and a Carmichael Fellowship (to MA). We have several people to thank for discussions which have improved our paper. In the early stages we benefited from discussions with David Garfinkle and Matt Visser. As the project developed, we had extensive discussions with Damien Martin, Matthew Kleban and Brien Nolan. Of course, we do not mean to suggest that these people

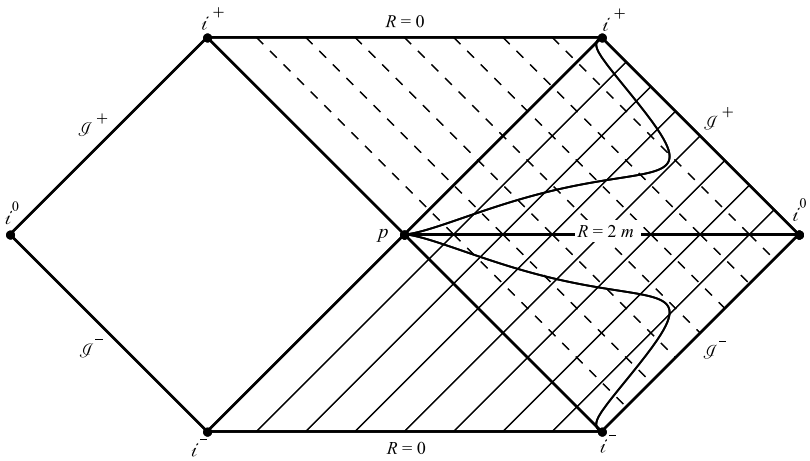

Figure 4.17: An extension of the McVittie spacetime for $H_0 = 0$ which is null geodesically complete. Note that all trajectories terminate on the spacelike singularity $R = 2m$. The loci $f = 0$ are shown.

necessarily agree or disagree with what we have concluded here.

4.12 References

[*] Electronic Address: lake@astro.queensu.ca

[**] Electronic Address: majd@astro.queensu.ca

[1] G. C. McVittie, Mon. Not. R. Astron. Soc. **93**, 325 (1933). See also Ap. J. **143**, 682 (1966) and *General Relativity and Cosmology* (University of Illinois Press 1962)

[2] For discussions of a black holes embedded in an expanding universe see A. Krasiński and C. Hellaby, Phys. Rev. D **69**, 043502 (2004) [arXiv:gr-qc/0309119v2], P. Jacewicz and A. Krasiński [arXiv:gr-qc/1101.5307v1] and references therein. For a recent discussion of inhomogeneous cosmologies see K. Bolejko, A. Krasiński, C.

Hellaby and M-N Célérier, *Structures in the Universe by Exact Methods* (Cambridge University Press, Cambridge, 2009) and references therein.

[3] Damien Martin, Ph. D. thesis, University of California, Davis (2011)

[4] M. Carrera and D. Giulini, Rev. Mod. Phys. **82**, 169 (2010) [arXiv:gr-qc/0810.2712v2]

[5] M. Carrera and D. Giulini, Phys. Rev. D **81**, 043521 (2010) [arXiv:gr-qc/0908.3101]

[6] N. Kaloper, M. Kleban and D. Martin, Phys. Rev. D **81**, 104044 (2010) [arXiv:hep-th/1003.4777v3]

[7] K, Bolejko, M-N Célérier and A. Krasiński, Classical Quantum Gravity (in press) (2011) [arXiv:astro-ph/1102.1449]

[8] B. C. Nolan, Classical Quantum Gravity **16**, 1227 (1999).

[9] We use geometrical units and a signature of +2 throughout. Functional dependence is designated only on the first appearance of a function.

[10] C. W. Misner, K. S. Thorne and J. A. Wheeler, *Gravitation*, (W. H. Freeman, San Francisco, 1973)

[11] $M \equiv \mathcal{R}_{\theta\phi}{}^{\theta\phi} R^3/2$ where $\mathcal{R}$ is the Riemann tensor.

[12] See, for example, K. Lake and R. Roeder, Phys. Rev. D **15**, 3513 (1977).

[13] R. Penrose in *Battelle Rencontres*, edited by C. M. DeWitt and J. A. Wheeler (W. A Benjamin, New York, 1968)

[14] M. J. Jaklitsch, C. Hellaby and D. R. Matravers, GRG **21**, 941 (1989).

[15] J. Griffiths and J. Podolský, *Exact Space-Times in Einstein's General Relativity* (Cambridge University Press, Cambridge, 2009)

[16] The choice of the shape of the singularity $R = 2m$ as a straight horizontal line is arbitrary, as is the choice of the time transformation function (4.35). Any spacelike curve (i.e. $-1 < slope < 1$) with a finite length, and any function, that is monotonically increasing, and spans $0 < t < \infty$ in a finite interval of the new variable, could be used to construct the conformal diagram.

[17] See, for example, E. Poisson, *A Relativist's Toolkit: The Mathematics of Black-Hole Mechanics* (Cambridge University Press, Cambridge, 2004)

[18] K. Lake, Classical Quantum Gravity **27**, 097001 (2010) [arXiv:gr-qc/1002.3600]

[19] This is defined by $\mathcal{L}(x)e^{\mathcal{L}(x)} = x$. See, for example, R. M. Corless, G. H. Gonnet, D. E. G. Hare, D. J. Jeffrey, and D. E. Knuth, Advances in Computational Mathematics **5**, 329 (1996).

[20] With conditions (4.7) the metric tensor and all derivatives to order 2 are continuous accross $\mathcal{H}$ and so matching accross $\mathcal{H}$ is complete under any formulation of matching conditions.

[21] W. Ballik and K. Lake, "The volume of static black holes" [arXiv:1005.1116]

[22] This is a package which runs within Maple. It is entirely distinct from packages distributed with Maple and must be obtained independently. The GRTensorII software and documentation is distributed freely on the World-Wide-Web from the address *http://grtensor.org*

Chapter 5

Paper IV: Penrose Diagrams of McVittie with $\Lambda < 0$

Paper Title[1]: "The McVittie solution with a negative cosmological constant"

[1]This chapter contains a version of a paper published in Physical Review D as: Philippe Landry, Majd Abdelqader, and Kayll Lake, Physical Review D, **86**, 8, 084002 (2012).

5.1 Abstract

Whereas current cosmological observations suggest that the universe is dominated by a positive cosmological constant ($\Lambda > 0$), the AdS/CFT correspondence tells us that the case $\Lambda < 0$ is still worthy of consideration. In this paper we study the McVittie solution with $\Lambda < 0$. Following a related study, the solution is understood here by way of a systematic construction of conformal diagrams based on detailed numerical integrations of the null geodesic equations. As in the pure Robertson - Walker case, we find that $\Lambda < 0$ ensures collapse to a Big Crunch, a feature which completely dominates the global structure.

5.2 Introduction

Recently [1], a detailed study of the McVittie solution [2] was carried out for a non-negative cosmological constant ($\Lambda \geq 0$). The McVittie solution has been known for many years, but it continues to attract interest [3]. Even though it is now widely believed that the universe is dominated by a positive cosmological constant, the remarkable AdS/CFT correspondence [4] presents a strong argument that the case $\Lambda < 0$ should also be examined. Following [1] we systematically construct a global view of the McVittie solution with $\Lambda < 0$ based on numerical integrations of the null geodesics. What results is a situation very distinct from the case $\Lambda \geq 0$: the global structure is completely dominated by a collapse to a Big Crunch, just as in the pure Robertson - Walker case.

5.3 The Solution

5.3.1 Overview

For a perfect fluid with energy density ρ and isotropic pressure p the strong energy condition [5] is given by

$$\rho + 3p \geq 0. \tag{5.1}$$

For a Robertson - Walker background with scale factor $a(t)$, for (5.1), Einstein's equations with $\Lambda < 0$ give

$$-3\frac{\ddot{a}}{a} \geq -\Lambda > 0 \tag{5.2}$$

where $\dot{} \equiv d/dt$, and so we necessarily have a Big Crunch [6]. The particular solution we are concerned with here is the simplest of the McVittie class, and this can be written in the form (e.g. [7]) [8]

$$ds^2 = -\left(\frac{1-m/2u}{1+m/2u}\right)^2 dt^2 + a^2(1+m/2u)^4(dr^2 + r^2 d\Omega_2^2) \tag{5.3}$$

where $u \equiv ra$, m is a positive constant and $d\Omega_2^2$ is the metric of a unit 2-sphere. If the McVittie solution (5.3) asymptotes to a reasonable Robertson - Walker background, then, as in the pure Robertson - Walker case, $\Lambda < 0$ gives rise to a Big Crunch which dominates the global structure. As previously [1], we use the coordinate transformation

$$R(t,r) \equiv u(1+m/2u)^2 \tag{5.4}$$

to obtain

$$ds^2 = -f(t,R)dt^2 - \frac{2H(t)R}{\sqrt{1-2m/R}}dtdR + \frac{dR^2}{1-2m/R} + R^2 d\Omega_2^2 \tag{5.5}$$

where

$$f \equiv 1 - 2m/R - H^2R^2 \tag{5.6}$$

and H is the Hubble function $\dot{a}/a$. From (5.5) it follows that tangents to surfaces of constant finite t are spacelike for $R > 2m$ (and so for finite t we set the future orientation $dt/d\lambda > 0$ for affine λ increasing to the future) and tangents to surfaces of constant R are spacelike for $f < 0$, null for $f = 0$ and timelike for $f > 0$. We note again that the effective gravitational mass [9] associated with (5.5) is not m, but rather M, given by

$$M(t, R) = m + \frac{1}{2}H^2R^3. \tag{5.7}$$

5.3.2 The function H

Quite unlike [1], we note that because of (5.2),

$$t \to \infty \quad \nexists. \tag{5.8}$$

Rather, we are now interested in models for which

$$a(0) = a(t_f) = 0, \quad \dot{a}(t_0) = 0 \tag{5.9}$$

where

$$0 \quad < \quad t_0 \quad < \quad t_f, \tag{5.10}$$

and

$$H(0 < t < t_0) > 0, \; H(t_0) = 0, \;\; H(t_0 < t < t_f) < 0. \tag{5.11}$$

Note that from (5.7)

$$M(t_0, R) = m, \tag{5.12}$$

and from (5.2)

$$\dot{H} < 0. \tag{5.13}$$

Whereas from the definition of u, $\lim_{t\to 0,t_f} u = 0$ for all finite r, from the transformation (5.4)

$$\lim_{t\to 0,t_f} R = \begin{cases} 0 & \text{if } m = 0 \\ \\ \infty & \text{if } m \neq 0 \end{cases} . \tag{5.14}$$

As a result, neither $t = 0$ nor $t = t_f$ are part of the spacetime (5.5) for $m \neq 0$. We note that (5.14) shows us that there is no continuous transition from $m \neq 0$ to $m = 0$.

5.3.3 Scalar Singularities

As explained previously [1], singularities, as revealed by scalars polynomial in the Riemann tensor, are reflected here by the Ricci scalar $\mathcal{R}$,

$$\mathcal{R} = 12H^2 + \frac{6\dot{H}}{\sqrt{1-2m/R}} , \tag{5.15}$$

since all other invariants, derived from (partial) derivatives of the metric tensor no higher than 2, add no new information in the cases under consideration. For $0 < t < t_f$, since $\dot{H} \neq 0$, there are singularities at $R = 2m$ ($u = m/2$), which are spacelike. The apparent singularities at $t = 0$ and at $t = t_f$[2], over the range $2m < R < \infty$ are, as explained above, not part of the spacetime.

5.3.4 The locus $f = 0$

As in the previous analysis [1], the locus $f = 0$ is important for an understanding of the spacetime (5.5). However, due to the nature of the function H studied here,

[2]We assume that $\dot{a} \neq 0$ at $t = 0$ and $t = t_f$.

this locus is quite distinct from the locus studied in [1]. In particular, the roots $R_\pm$ studied there do not exist for $\Lambda < 0$. First let us note that the locus $f = 0$ includes $R = 2m$ at $t = t_0$ where $H = 0$. Moreover, since

$$\left(\frac{m}{R^2} - H^2 R\right)\dot{R} = H\dot{H}R^2 \tag{5.16}$$

along the locus, R can have a vertical tangent in the $R - t$ plane on $0 < t < t_0$ and $t_0 < t < t_f$ only at $R = 3m$. As $R \to \infty$ the locus becomes $H^2R^2 = 1$ which requires $H \to 0$, that is, $t \to t_0^\pm$.

5.3.5 Null Geodesics - Qualitative

The radial null geodesics of (5.5) satisfy

$$\frac{dR}{dt} = \sqrt{1 - 2m/R}\left(HR \pm \sqrt{1 - 2m/R}\right). \tag{5.17}$$

We label the branch "+" "outgoing" and the branch "-" "ingoing". Clearly

$$\left.\frac{dR}{dt}\right|_{t_0} = \pm\left(1 - \frac{2m}{R}\right) \tag{5.18}$$

and so the ingoing geodesics already have $dR/dt < 0$ at t_0 whereas the outgoing geodesics have $dR/dt > 0$ at t_0. Further,

$$\frac{dR}{dt} = 0 \tag{5.19}$$

at $f = 0$ for ingoing null geodesics when $t < t_0$ and for outgoing null geodesics when $t > t_0$. Since $dR/dt > 0$ along both branches for $f < 0$ and $t < t_0$ and $dR/dt < 0$ along both branches for $f < 0$ and $t > t_0$ it follows that the ingoing geodesics reach a maximum R at $f = 0$ for $t < t_0$ and the outgoing geodesics reach a maximum R at $f = 0$ for $t > t_0$. A special case is shown below in Figure 5.1 and Figure 5.2.

5.3.6 Energy conditions in general

Let us start by rewriting the energy density and isotropic pressure in terms of H. From Einstein's equations with $\Lambda < 0$ we find

$$8\pi\rho = 3H^2 - \Lambda,\ 8\pi p = -3H^2 - \frac{2\dot{H}}{\sqrt{1-2m/R}} + \Lambda. \tag{5.20}$$

As a result, with (5.13), a general feature of these models is $\rho \geq 0$ and $\rho + p \geq 0$ and so the null and weak energy conditions are always satisfied. The strong energy condition requires $\rho + 3p \geq 0$ which, from (5.20), gives

$$\frac{\dot{H}}{\sqrt{1-2m/R}} + H^2 \leq \frac{\Lambda}{3} < 0. \tag{5.21}$$

The dominant energy condition requires

$$-\rho \leq p \leq \rho. \tag{5.22}$$

It follows from (5.13), (5.20) and (5.22) that whereas the left-hand inequality is generally satisfied, the right-hand inequality requires

$$-\frac{\dot{H}}{\sqrt{1-2m/R}} \leq 3H^2 - \Lambda. \tag{5.23}$$

5.4 A specific form for H

We cannot proceed with further details without a specific form for H. For notational convenience, and for a comparison with [1], define

$$H_0^2 \equiv -\frac{\Lambda}{3},\ \ T \equiv 3H_0 t, \tag{5.24}$$

and take $H_0 > 0$. For a we take the Robertson - Walker scale factor for spatially flat dust with $\Lambda < 0$. This gives

$$H = \frac{H_0 \sin(T)}{1 - \cos(T)}. \tag{5.25}$$

Clearly H is periodic with period 2π and so $T_0 = \pi$. Moreover,

$$\dot{H} = -\frac{3H_0^2}{1-\cos(T)}. \tag{5.26}$$

The dominant feature in our study is the development of a Big Crunch. We know that this will occur with $\Lambda < 0$ as long as the strong energy condition holds. For more general equations of state, say $p = \kappa\rho$, the strong energy condition gives $\rho(1+3\kappa) \geq 0$. Since the minimum $8\pi\rho$ in our considerations is $-\Lambda > 0$, we would recover the same structure for $\kappa > -1/3$. In this sense our choice of $\kappa = 0$ is not critical.

5.5 Energy conditions

From (5.21) we find that the strong energy condition is satisfied for

$$\frac{3}{\sqrt{1-2m/R}} \geq 2. \tag{5.27}$$

Since the left side of (5.27) is at least 3, we see that the strong energy condition is always satisfied. For the dominant energy condition we rearrange (5.23) to give

$$\frac{R}{m} \geq \frac{8}{3} \tag{5.28}$$

and so the dominant energy condition fails sufficiently close to the singularities.

5.6 Integration of the null geodesics

5.6.1 Integration in the $R-T$ plane

With (5.25) we can write the null geodesic equations (5.17) in the dimensionless form

$$\frac{dY}{dT} = \sqrt{1-2/Y}\left(\frac{\sin(T)}{1-\cos(T)}\left(\frac{Y}{3}\right) \pm \frac{1}{3\delta}\sqrt{1-2/Y}\right) \tag{5.29}$$

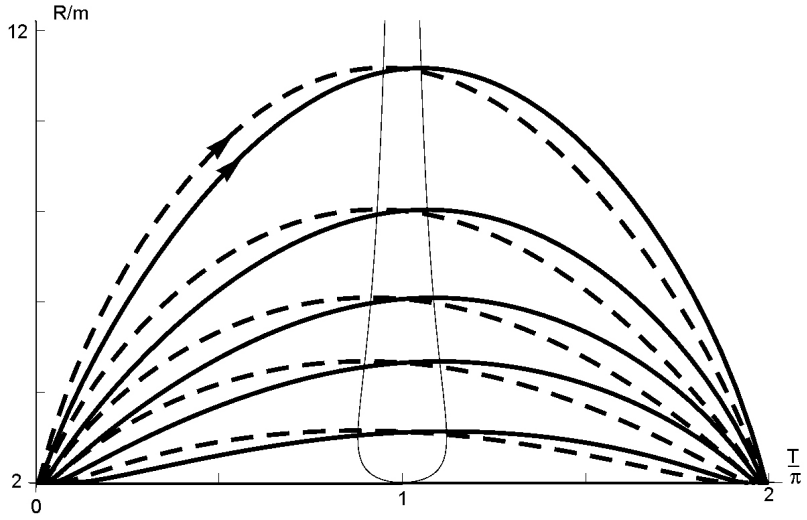

Figure 5.1: Numerical integrations of (5.29) and the locus $f = 0$. The ingoing geodesics ("$-$") are shown dashed and reach their maximal value of R/m on the left branch of the locus $f = 0$. The outgoing geodesics ("$+$") are shown solid and reach their maximal value of R/m on the right branch of the locus $f = 0$. The future orientation is T increasing as shown. All geodesics begin and end at $R = 2m$ which has two distinct parts, separated by the exceptional point $T = \pi, R = 2m$. This exceptional point is not part of the spacetime. An enlarged view near $R = 2m$ is shown in Figure 5.2.

where $Y \equiv R/m$ and δ is the parameter $H_0 m$. Numerical integrations of (5.29) are shown in Figures 5.1 and 5.2.

5.6.2 Integration in the $z - T$ plane

As previously [1], we find it numerically convenient to compactify R and define

$$z \equiv \sqrt{1 - \frac{2}{Y}} \tag{5.30}$$

so that equation (5.29) takes the form

$$\frac{dz}{dT} = \frac{(1 - z^2)}{6} \left(\frac{\sin(T)}{1 - \cos(T)} \pm \frac{z(1 - z^2)}{2\delta} \right). \tag{5.31}$$

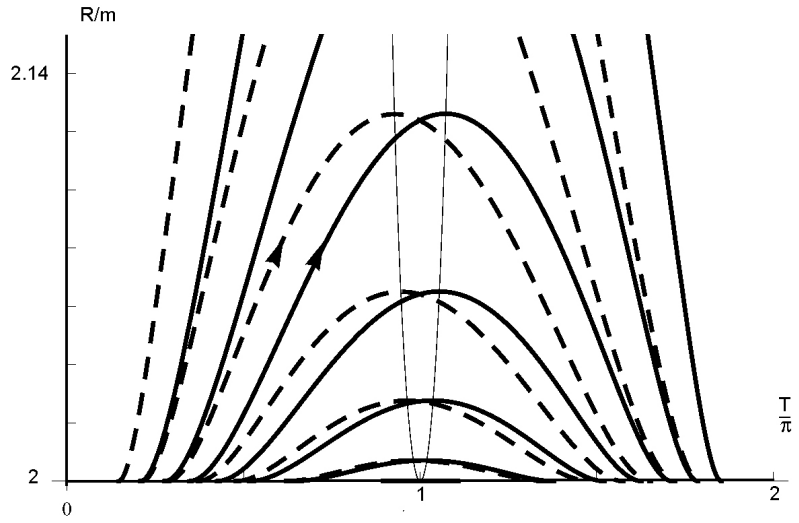

Figure 5.2: As in Figure 5.1 in the neighborhood of $R = 2m$.

Numerical integrations of (5.31) are shown in Figure 5.3. Any point in the spacetime $(0 < T < 2\pi, R > 2m)$ can be connected to the past boundary $(R = 2m, 0 < T < \pi)$ by a unique null geodesic from each branch. We use this to construct the conformal diagram below.

5.7 Global structure of the spacetime

5.7.1 Construction of the conformal diagram

We represent the past boundary[3] as a horizontal line in a Cartesian plane ($y = 0, -1 \leq x \leq 1$), setting the right end of $R = 2m$ at $T = 0$, and the left end at

[3]Our understanding is that null affine distance is relevant iff the coordinates diverge, indicating the incompleteness of the coordinates for finite affine distances. There is no divergence of the coordinates in this paper. In particular, if the boundaries $(R = 2m)$ are at finite null affine distance, this finiteness is irrelevant due to the fact that $R = 2m$ is genuinely singular and no extension is possible. If the boundaries $(R = 2m)$ are at infinite null affine distance the conformal diagrams remain unchanged and complete. That is, the affine completeness of the null geodesics is, in this case, irrelevant, quite unlike the cases $\Lambda \geq 0$ [1].

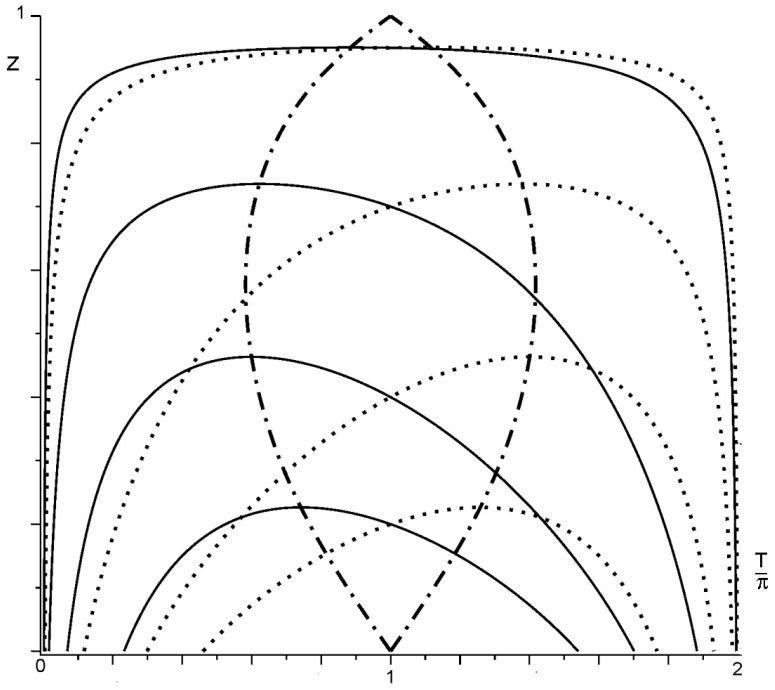

Figure 5.3: Numerical integrations of (5.31) and the locus $f = 0$. The ingoing geodesics ("$-$") are now shown solid and reach their maximal value of z on the left branch of the locus $f = 0$. The outgoing geodesics ("$+$") are now shown dashed and reach their maximal value of z on the right branch of the locus $f = 0$. The future orientation is T increasing as above. All geodesics begin at $z = 0$ for some value of $0 < T < \pi$ and terminate again at $z = 0$ for $\pi < T < 2\pi$.

$T = \pi$. To represent the interval $0 < T < \pi$, from $x = -1$ to 1, we only require a one-to-one function between these two variables. Our choice for $x(T)$ is given in the Appendix. This function was chosen purely for visual reasons by finding the spline curve fit of several points that were adjusted manually to make the resulting conformal diagram more visually appealing. Note that the choice of the shape of the curve ($R = 2m, 0 < T < \pi$) to be a horizontal straight line, as well as the function $x(T)$ used is arbitrary and does not change the overall global structure presented in the conformal diagram. It is only required that the curve ($R = 2m, 0 < T < \pi$) be

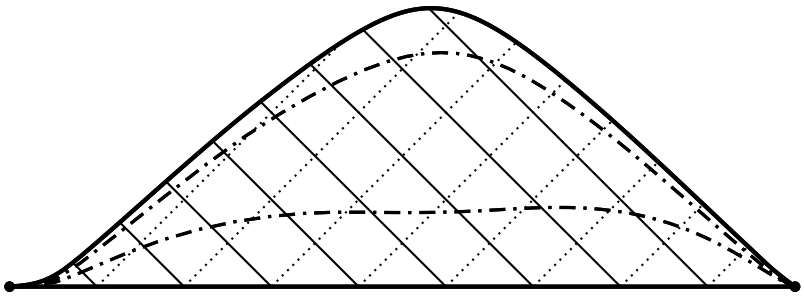

Figure 5.4: Conformal representation of the outgoing null geodesics (dashed) and ingoing null geodesics (solid). The locus $f = 0$ is also shown. This locus is globally spacelike. Note that $f > 0$ between the two branches of the locus. The boundaries are at $R = 2m$. The point at the lower right is $R \to \infty, 0 \leq T \leq 2\pi$. The point at the lower left is $T = \pi, R = 2m$.

space-like, and the function $x(T)$ be one-to-one. After this point, the procedure we used is identical to that in [1].

5.7.2 Null geodesics

Under the procedure described above, Figure 5.3 is mapped into Figure 5.4.

5.7.3 Surfaces of constant R and T

Conformal representations of surface of constant R and constant T are shown in Figures 5.5 and 5.6 respectively.

5.7.4 The fluid streamlines

The conformal representation of the fluid streamlines $r = constant$ is shown in Figure 5.7. These trajectories are, of course, globally timelike. From (5.4) we have $u > m/2$ for $R > 2m$. The scale factor is $a(t) = \mathcal{C}(1 - \cos(T))^{1/3}$ where $\mathcal{C}$ is a constant > 0.

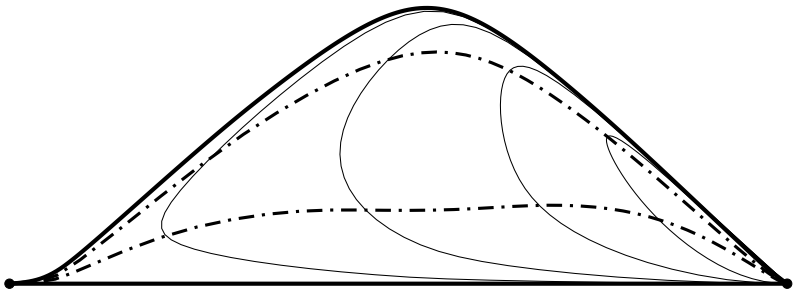

Figure 5.5: The trajectories show surfaces of constant R. These are timelike within the locus $f = 0$ and spacelike outside the locus. The values of z used to generate these curves are $0.15, 0.3, 0.5$ and 0.7.

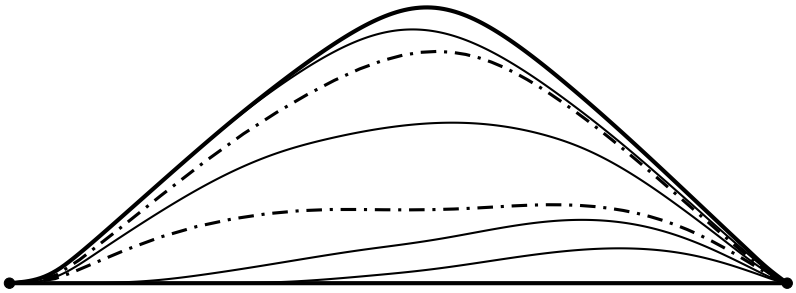

Figure 5.6: The trajectories show surfaces of constant T. These are globally spacelike. The values of T used to generate these curves (bottom up) are $\pi/3, \pi/2, \pi$ and $3\pi/2$.

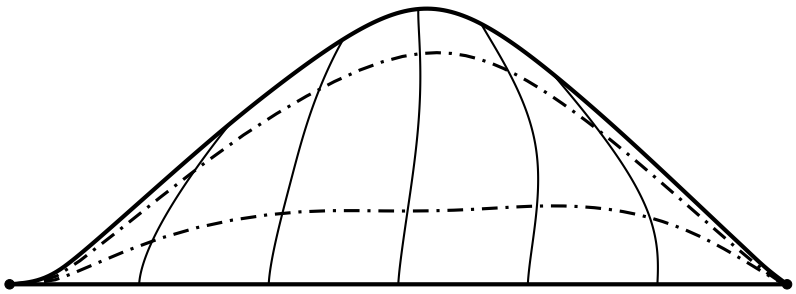

Figure 5.7: Trajectories of constant r characterized by the constant ϵ as explained in the text. We note that $\epsilon \to 1/2\sqrt[3]{2}$ to the left and $\epsilon \to \infty$ to the right.

Writing $\epsilon = r\,\mathcal{C}/m$ we have

$$\frac{R}{m} = \frac{(2\epsilon(1-\cos(T))^{1/3}+1)^2}{4\epsilon(1-\cos(T))^{1/3}}, \tag{5.32}$$

and we note that $R = 2m$ for $T = T_0$ and $T = 2\pi - T_0$ where

$$T_0 = \arccos\left(\frac{8\epsilon^3 - 1}{8\epsilon^3}\right). \tag{5.33}$$

Note that $1/2\sqrt[3]{2} < \epsilon < \infty$ as explained in the Figure.

5.8 Discussion

Motivated by the AdS/CFT correspondence, we have examined the McVittie solution with a negative cosmological constant $\Lambda < 0$. A detailed construction of the global structure has been given for the case of a background of dust. We have found that the situation is very distinct from the cases $\Lambda \geq 0$ [1]. As in the pure Robertson - Walker case, we find that $\Lambda < 0$ ensures collapse to a Big Crunch, a feature which completely dominates the global structure.

5.9 Appendix

5.9.1 $x(T)$

$$x(T) = \begin{cases} 1 - 2.66T + 7.82T^3 & , \quad 0 \quad < T \leq \quad 0.177 \\ 1.02 - 3.6T + 3.43T^2 - 1.9T^3 & , \quad 0.177 \quad < T \leq \quad 0.6 \\ 0.557 - 0.772T - 0.395T^2 + 0.222T^3 & , \quad 0.6 \quad < T \leq \quad 1.42 \\ 1.87 - 3.55T + 1.56T^2 - 0.235T^3 & , \quad 1.42 \quad < T \leq \quad 2.2 \\ -0.601 - 0.172T + 0.0217T^2 - 0.00230T^3 & , \quad 2.2 \quad < T \leq \quad \pi \end{cases} \tag{5.34}$$

5.10 acknowledgments

The conscientious efforts of the referee helped us improve the content of this paper. This work was supported in part by a grant (to KL) from the Natural Sciences and Engineering Research Council of Canada. Portions of this work were made possible by use of *GRTensorII* [11].

5.11 References

[1] K. Lake and M. Abdelqader, Phys. Rev. D **84**, 044045 (2011) [arXiv:gr-qc/1106.3666]

[2] G. C. McVittie, Mon. Not. R. Astron. Soc. **93**, 325 (1933). See also Ap. J. **143**, 682 (1966) and *General Relativity and Cosmology* (University of Illinois Press 1962)

[3] See, for example, V. Faraoni, A. F. Zambrano Moreno and R. Nandra, Phys. Rev. D **85**, 083526 (2012) [arXiv:1202.0719], R. Nandra, A. N. Lasenby and M. P. Hobson, Monthly Notices of the Royal Astronomical Society, **422**, 2931 (2012) [arXiv:1104.4447], C. Gao, X. Chen, Y.-G. Shen and V. Faraoni, Phys. Rev. D **84**, 104047 (2011) [arXiv:1110.6708]. For a review see M. Carrera and D. Giulini, Rev. Mod. Phys. **82**, 169 (2010) [arXiv: 0810.2712v2].

[4] See, for example, O. Aharony, S. Gubser, J. Maldacena, H. Ooguri, Y. Oz, Phys. Rept. **323**, 183 (2000) [arXiv:hep-th/9905111v3]

[5] S. W. Hawking and G. F. R. Ellis, *The large scale structure of space-time*. (Cambridge University Press, Cambridge, 1973)

[6] For a more general result see F. J. Tipler, Ap. J. **209**, 12 (1976).

[7] B. C. Nolan, Classical Quantum Gravity **16**, 1227 (1999).

[8] We use geometrical units and a signature of +2 throughout. Functional dependence is designated only on the first appearance of a function.

[9] $M \equiv \mathcal{R}_{\theta\phi}{}^{\theta\phi} R^3/2$ where $\mathcal{R}$ is the Riemann tensor.

[10] J. Griffiths and J. Podolský, *Exact Space-Times in Einstein's General Relativity* (Cambridge University Press, Cambridge, 2009).

[11] This package runs within Maple. The GRTensorII software and documentation is distributed freely from the address *http://grtensor.org*

Chapter 6

Conclusion

6.1 Summary

We have developed two new tools to analyze spacetimes and shed some light on their meaning, and have successfully applied them to several important exact solutions to Einstein's field equations. The first tool is based on examining the gradient fields of curvature invariants. This tool provided an intuitive way to visualize the cumulative tidal and frame-dragging effects of the spacetime. We applied this tool to the Curzon-Chazy solution in Chapter 2, and demonstrated that this metric does represent the gravitational field of a non-rotating ring. This was done by careful construction of Newtonian analogs to the curvature invariants and their gradient fields via tidal tensors. The quantitative similarities between the gradient fields of the Curzon-Chazy metric and the Newtonian ring provide the most compelling argument to date about the nature of the source that produces the Curzon-Chazy spacetime. Furthermore, the curvature invariant analysis allowed us to derive a new coordinate transformation that unfolds the singularity of the metric in a physically meaningful and intuitive

manner. In Chapter 3, we applied this analysis tool the Kerr metric, and discovered fundamental physical properties of rotating black holes. Specifically, we found that the cumulative tidal and frame-dragging effects produced by a rotating black hole outside its horizon depends on its angular moment, changing quantitatively at 7 specific values of the dimensionless spin parameter. These 7 values are A=[0.3090, 0.4339, 0.5878, 0.7818, 0.8090, 0.9511, 0.9749], evaluated to 4 significant figures.

The second tool involved constructing accurate conformal Penrose diagrams, based on detailed numeric solutions of radial null geodesics, and not on qualitative guessing as it has been done generally. In Chapter 3 we applied this tool to a particular case of the McVittie solution, where the background was chosen to be the ΛCDM model of the universe. This allowed us for the first time to construct accurate conformal diagrams of this metric, revealing its causal structure and horizons. It has been long debated whether this solution actually represents the spacetime of a black hole embedded in a homogeneous FLRW universe, and our analysis confirmed that this is indeed the case. Furthermore, we produced conformal diagrams of McVittie with different background models of the universe, with $\Lambda = 0$ in Chapter 3, and $\Lambda < 0$ in Chapter 4 for a thorough analysis of the solution.

6.2 Future Work

6.2.1 Analysis of Additional Cases of the Weyl Metric

The Weyl metric provides us with a very convenient and systematic way to construct infinitely many solutions to Einstein's field equations, as well as the superposition of two or more existing axisymmetric solutions. However, the lack of understanding of

the resulting solutions makes it difficult so far to take full advantage of the Weyl metric and its potential applications to astrophysics and cosmology. In future research, we will utilize the analysis and visualization tools we have developed to study more exact solutions, specifically the many-body solutions that are special cases of the Weyl metric (e.g. Curzon-Chazy two particle solution, among others). Although these solutions are static, a deeper understanding could provide new information about the non-linear aspects of Einstein's equations, as well as the global effect that the self-interaction contribution has on spacetime. This can be achieved by a systematic study of these many-body solutions, then comparing them to their Newtonian counterparts, with the attempt to mimic the non-linearity in toy model Newtonian potentials for the self-interaction.

6.2.2 Analysis of Numerical Relativity Simulations

The visualization and analysis tools we have developed have been applied only to analytic solutions so far. However, we plan to extend the application of the these tools to numerical relativity simulations in collaboration with other groups. Similar visualization tools constructed from projections of the Weyl tensor have been proposed and are being put to use for numerical simulation analysis. Therefore, our proposal of visualizing the gradient fields of invariants constructed from contractions of the Weyl tensor would be complimentary to those tools. Furthermore, the results we have for the Kerr metric indicates that the observable global structure of these gradient fields changes depending on the spin parameter (i.e. the number and type of critical points outside the horizon). Therefore, we will explore the possibility of using these tools to provide an alternative method to estimate the angular momentum and other physical

parameters of the final state of binary black hole merger simulations.

6.2.3 Spherically Symmetric Spacetimes

Significant attention is being given to locally inhomogeneous cosmologies recently, in order to have rigorous framework to account for the effects that local inhomogeneities have on cosmological observations and gravitational lensing at cosmological scales. In the next step of my research, I plan to use both of the tools presented in this PhD thesis in combination (Penrose diagram construction and gradient fields of invariants) to analyze some local inhomogeneous exact solutions, starting with Tolman-Bondi solution. We will work on improving and combining these tools to make it applicable to spherically symmetric spacetimes in general. This includes the study of other local inhomogeneous cosmologies, as well as spherical gravitational collapse, where some fundamental questions in General Relativity remain unsolved.